الجمهورية الجزائرية الديمقراطية الشعبية
People's Democratic Republic of Algeria
وزارة التعليم العالي والبحث العلمي
Ministry of Higher Education and Scientific Research

جامعة زيان عاشور بالجلفة
Ziane Achour University of Djelfa

كلية العلوم و التكنولوجيا
Faculty of Science and Technology

Department: Mechanical Engineering

Order N°: …. / 2026

Defense authorization N° ……/2026

DOCTORAL THESIS

3rd Cycle Doctoral (D-LMD)

Presented by

Ahmed TAIBAOUI

With a view to obtaining the doctoral diploma in 3rd Cycle Doctoral (D-LMD)

Branch: Mechanical Engineering

Specialty: Energetics

Topic

Improvement of wind turbines availability based on the optimization of their performances.

Supported, on 14/02/2026, before the jury composed of:

First and Last name	Grade	Institution of affiliation	Designation
Dr. AIDAOUI Lakhdar	Professor	University of Djelfa	President
Dr. BENMESSAOUD Tahar	MCA	University of Djelfa	Supervisor
Dr. KEZRANE Cheikh	Professor	University of Djelfa	Co-Supervisor
Dr. ROUIBAH Abdelkader	MCA	University of Djelfa	Examiner
Dr. MOHAMMEDI Kamal	Professor	University of Boumerdes	Examiner
Dr. Hadi Taibi	MCA	University of Djelfa	Examiner

Djelfa University, FST - 2026

Acknowledgements

*First and foremost, all praises and thanks are due to **Allah Almighty**, who has granted us the strength, wisdom, and perseverance to accomplish this study.*

*I am deeply grateful to **Professor Tahar BENMESSAOUD** and **Professor Cheikh KEZRANE** for their unwavering support and guidance throughout the entire duration of this work. I sincerely appreciate the valuable discussions and insights they have shared with me.*

*My special thanks and appreciation go to the members of the **Laboratory of Development in Mechanics and Materials (LDMM)** for their assistance and collaboration.*

*Lastly, I would like to express my heartfelt gratitude to my **Parents**, **family**, and **friends** for their constant encouragement, support, love, and care.*

Dedication

First and foremost, I offer my deepest gratitude to Allah, the Almighty, for the strength and grace to complete this journey.

This work is most honorably dedicated to my beloved Parents; it is through their endless sacrifices and unwavering belief in me that I have become the person I am today. I am eternally in their debt.

I also extend this dedication to

my brothers and sisters,

my extended family,

and my friends,

for their constant encouragement.

Thank you all.

Abstract

The increasing reliance on wind energy as a sustainable power source has intensified the need to improve the aerodynamic performance, structural integrity, and operational availability of wind turbines. These systems operate under complex and variable loading conditions, where aerodynamic efficiency, material behavior, and maintenance strategies play a critical role in overall performance and cost-effectiveness. This thesis contributes to this context through an integrated numerical and optimization-based approach organized into four main parts. First, the aerodynamic and structural behavior of Horizontal Axis Wind Turbine (HAWT) blades is investigated across different tip-speed ratios, with particular attention to the effect of Young's modulus. Second, the unsteady aerodynamic performance of three airfoils—NACA 4412, NACA 23012, and NACA 63415—is analyzed. Third, the aerodynamic optimization of Savonius wind turbines is studied by evaluating several diffuser configurations. Finally, a multi-objective maintenance optimization framework is proposed. The results indicate that low tip-speed ratio lead to flow separation near the blade trailing edge, while optimal tip-speed ratio maintain attached flow along the blade span. Structural analysis shows that blade deformation increases from hub to tip and decreases with higher Young's modulus, with maximum stresses concentrated at the blade–hub junction. A comparison between one-way and two-way fluid–structure interaction (FSI) approaches shows that the difference depends strongly on blade stiffness. The largest discrepancy, reaching 8.21%, occurs at a low Young's modulus (5×10^{8} Pa), while the difference progressively decreases as stiffness increases and becomes nearly negligible for high Young's modulus values. Among the airfoils studied, NACA 4412 provides the best aerodynamic performance, while NACA 63415 exhibits larger separation regions and higher drag. The optimized diffuser configuration for the Savonius turbine achieves a maximum power coefficient of 0.433. Additionally, the proposed maintenance strategy reduces lost production costs by more than 64% and increases turbine availability to 98%.

Keywords: Aerodynamic Performance, Fluid-Structure Interaction, Structural Responses, Maintenance Optimization, Wind Turbine Availability, Whale Optimization Algorithm.

ملخص

أدى الاعتماد المتزايد على طاقة الرياح كمصدر مستدام للطاقة إلى زيادة الحاجة إلى تحسين الأداء الديناميكي الهوائي والسلامة الهيكلية والتوافر التشغيلي لتوربينات الرياح. تعمل هذه الأنظمة في ظل ظروف معقدة ومتغيرة، حيث تلعب الكفاءة الديناميكية الهوائية وسلوك المواد واستراتيجيات الصيانة دورًا حاسمًا في الأداء العام والفعالية من حيث التكلفة. تساهم هذه الأطروحة في هذا السياق من خلال نهج رقمي تحسيني متكامل ، ومنظم في أربعة أجزاء رئيسية. أولاً، يتم دراسة السلوك الديناميكي الهوائي والهيكلي لشفرات توربينات الرياح ذات المحور الأفقي عبر نسب سرعة طرفية مختلفة، مع إيلاء اهتمام خاص لتأثير معامل يونغ. ثانيًا، يتم تحليل الأداء الديناميكي الهوائي غير المستقر لثلاثة أجنحة هوائية NACA 4412 و NACA 23012 وNACA 63415 . ثالثًا، تمت دراسة التحسين الديناميكي الهوائي لتوربينات الرياح Savonius من خلال تقييم عدة تكوينات للموجه. أخيرًا، تم اقتراح إطار عمل متعدد الأهداف لتحسين الصيانة. تشير النتائج إلى أن نسبة سرعة الطرف المنخفضة تؤدي إلى انفصال التدفق بالقرب من الحافة للشفرة، بينما تحافظ نسبة سرعة الطرف المثلى على التدفق الملتصق على طول امتداد الشفرة. يوضح التحليل الهيكلي أن تشوه الشفرة يزداد من المحور إلى الطرف وينخفض مع ارتفاع معامل يونغ، مع تركيز الضغوط القصوى عند تقاطع الشفرة والمحور. تظهر المقارنة بين نهجي التفاعل أحادي الاتجاه وثنائي الاتجاه بين الموائع والهياكل أن الفرق يعتمد بشكل كبير على صلابة الشفرة. يحدث أكبر تباين، الذي يصل إلى 8.21 بالمئة، عند معامل يونغ المنخفض (5×10^8 Pa)، بينما يتناقص الفرق تدريجياً مع زيادة الصلابة ويصبح ضئيلًا تقريبًا عند قيم معامل يونغ العالية. من بين الأجنحة الهوائية التي تمت دراستها، يوفر NACA 4412 أفضل أداء ديناميكي هوائي، بينما يظهر NACA 63415 مناطق فصل أكبر ومقاومة أعلى. يحقق تكوين الموجه المُحسّن لتوربين Savonius معامل طاقة أقصى يبلغ 0.433. بالإضافة إلى ذلك، تقلل استراتيجية الصيانة المقترحة تكاليف الإنتاج المفقودة بأكثر من 64٪ وتزيد من توفر التوربين إلى 98٪.

الكلمات المفتاحية: الأداء الديناميكي الهوائي، تفاعل الموائع والهياكل، الاستجابات الهيكلية، تحسين الصيانة، توفر توربينات الرياح، خوارزمية التحسين (WOA).

Résumé

Le recours croissant à l'énergie éolienne comme source d'énergie durable a intensifié la nécessité d'améliorer les performances aérodynamiques, l'intégrité structurelle et la disponibilité opérationnelle des éoliennes. Ces systèmes fonctionnent dans des conditions de charge complexes et variables, où l'efficacité aérodynamique, le comportement des matériaux et les stratégies de maintenance jouent un rôle essentiel dans les performances globales et la rentabilité. Cette thèse contribue à ce contexte grâce à une approche intégrée, numérique et basée sur l'optimisation, organisée en quatre parties principales. Tout d'abord, le comportement aérodynamique et structurel des pales des éoliennes à axe horizontal

(HAWT) est étudié pour différents rapports de vitesse de pointe, avec une attention particulière portée à l'effet du module d'Young. Ensuite, les performances aérodynamiques instables de trois profils aérodynamiques (NACA 4412, NACA 23012 et NACA 63415) sont analysées. Troisièmement, l'optimisation aérodynamique des éoliennes Savonius est étudiée en évaluant plusieurs configurations de diffuseurs. Enfin, un cadre d'optimisation de la maintenance à objectifs multiples est proposé. Les résultats indiquent qu'un faible rapport de vitesse périphérique entraîne une séparation du flux près du bord de fuite de la pale, tandis qu'un rapport de vitesse périphérique optimal maintient un flux attaché sur toute la longueur de la pale. L'analyse structurelle montre que la déformation de la pale augmente du moyeu vers l'extrémité et diminue avec un module d'Young plus élevé, les contraintes maximales étant concentrées à la jonction entre la pale et le moyeu. Une comparaison entre les approches d'interaction fluide-structure (FSI) unidirectionnelle et bidirectionnelle montre que la différence dépend fortement de la rigidité des pales. L'écart le plus important, atteignant 8,21 %, se produit à un faible module d'Young (5×10^8 Pa), tandis que la différence diminue progressivement à mesure que la rigidité augmente et devient presque négligeable pour des valeurs élevées du module d'Young. Parmi les profils aérodynamiques étudiés, le NACA 4412 offre les meilleures performances aérodynamiques, tandis que le NACA 63415 présente des zones de séparation plus importantes et une traînée plus élevée. La configuration optimisée du diffuseur pour la turbine Savonius atteint un coefficient de puissance maximal de 0,433. De plus, la stratégie de maintenance proposée réduit les coûts de perte de production de plus de 64 % et augmente la disponibilité de la turbine à 98 %.

Mots clés : Performances aérodynamiques, interaction fluide-structure, réponses structurelles, optimisation de la maintenance, disponibilité des éoliennes, algorithme d'optimisation (WOA).

Publication List

Journal Publication

TAIBAOUI, A., BENMESSAOUD, T., & KEZRANE, C. (2026). Analysis of Structural Responses of a Horizontal Axis Wind Turbine at Maximum Aerodynamic Performance. *Journal of Applied and Computational Mechanics*, *12*(1), 155-163. *https://doi.org/10.22055/jacm.2025.48025.4922*.

BENMESSAOUD, T., **TAIBAOUI, A.** A Comparative Unsteady Aerodynamic Analysis of NACA 4412, 23012, and 63415 Airfoils: Effects of Rotational Speed and Reynolds Number. *Journal of Information Systems Engineering and Management, 2025, 10(63s)* *https://doi.org/10.52783/jisem.v10i63s.13964*

BENMESSAOUD, T., ROUIBAH, A., & **TAIBAOUI, A.** (2025). Multi-objective optimization of wind turbines maintenance using the Whale Optimization Algorithm. *International Journal of Computational and Experimental Science and Engineering*, *11*(4). *https://doi.org/10.22399/ijcesen.4597*

International Conferences

TAIBAOUI, A., BENMESSAOUD, T., KEZRANE, C., & BENNOUR, E. Performance Analysis of Savonius Wind Turbine Equipped with Three Diffusers of Different Configurations Under Variable Tip Speed Ratios. *1st International Conference on Applications and Technologies of Renewable Energy Systems (ICATRES 2024)*, University of Djelfa, Algeria, December 18-19, 2024.

TAIBAOUI, A., BENMESSAOUD, T., KEZRANE, C., & BENNOUR, E. Investigation of Aerodynamic Performances and Airflow Patterns over a rotating Airfoils through a 2D Unsteady Simulations. *3rd International Conference on Energy, Materials and Environment (ICEME2024)*, University of Djilali Bounaama Khemis Miliana, Algeria, May 6th and 7th, 2024.

BENNOUR, E., Kaid, N., KEZRANE, C., **TAIBAOUI, A**. Enhancing Heat Transfer in Laminar Flow Using a Sinusoidal Tube with Vortex Generators. *Arab Conference on Mechanics & Engineering (ARCME'23)*, University of Biskra, Algeria,10th, 11th and 12th of December 2023

Table of Contents

Table of Figures

List of Tables

Nomenclature

Variables

A_r	rotor area (m^2)
A	Availability
c	airfoil chord length
C_{CM}	Corrective maintenance costs
CD	drag coefficient
C_{elec}	Electricity Cost [€ / kWh].
CL	lift coefficient
C_{loss}	Cost lost due to system downtime
Cp	Power Coefficient (-)
C_{pen}	Cost of additional work carried out by the maintenance team
C_{PM}	Preventive maintenance costs
C_t	Thrust Coefficient (-)
CT	Total cost
Dt	time step
E_k	kinetic energy
Pm	Mechanical power (W)
Pw	Wind Power (W)
r	radial position (m)
R	Radius of turbine (m)
T	Thrust Force (N)
Tm	Mechanical torque (N.m)
TSR	Tip speed Ratio (-)
u	displacement vector
V	Wind Velocity (m/s)
YM	Young's modulus (Pa)
C_{CMh}	the hourly cost for performing corrective maintenance
C_{CMa}	the average cost for performing preventive maintenance
C_{pen}	Penalty cost of additional maintenance work

Greek symbols

μ	Repair rate
δ	blade tip deflection (m)
ε	strain (-)
ε_t	deformation tensor
λ	Failure rate
ν	Poisson's ratio

ρ	air density (kg/m^3)
σ	stress (Pa)
υ	wind speed
ω	Rotational speed (rad/s)
α_{ji}	task j duration for corrective maintenance in wind turbine i
n_{ji}	supplementary hours for corrective maintenance task j in wind turbine i
β_{j}	number of preventive maintenance tasks

Acronyms

CFD	computational fluid dynamics
EXP	experimental
FEA	Finite Element Analysis
FSI	Fluid structure interaction
HAWT	Horizontal Axis Wind Turbine
MTBF	Mean time between failures
MTTR	Mean time to repair
SRF	Single Moving Reference Frame
VAWT	vertical axis wind turbines
WOA	Whale Optimization Algorithm

General Introduction

Background and Context

Wind energy has emerged as a key component of sustainable electricity production, particularly in regions with rich wind resources. Wind Turbines (WTs), both onshore and offshore, play a significant role in meeting national and global renewable energy targets. However, the performance and availability of these systems are challenged by two critical factors: the complex fluid–structure interactions that affect blade efficiency and durability, and the stochastic nature of wind loads, which introduces uncertainty in turbine maintenance planning.

Research Problem

This research addresses the dual challenge of optimizing wind turbine blade performance while improving their operational availability. Specifically, it investigates how key performance parameters—such as tip-speed ratio, Young's modulus, rotational speed, Reynolds number, and modifications to blade and diffuser configurations—influence aero-structural behavior in wind turbines. and how intelligent maintenance scheduling can mitigate downtime and reduce associated costs. The problem is rooted in the need to maximize power output and structural reliability while minimizing unexpected failures and operational disruptions.

Objectives

The objectives of this research are as follows:

1. To numerically analyze the aerodynamic and structural responses of HAWT blades across a range of tip-speed ratios and Young's modulus values.
2. To compare One-way and Two-way Fluid-Structure Interaction (FSI) simulation approaches in terms of deformation, and blade tip deflection.
3. To provide a comparative analysis of the aerodynamics of three airfoils named NACA-4412, NACA-23012, and NACA-63415, through two-dimensional unsteady

simulations, the computational approach thoroughly explores the impact of rotational speeds and a range of Reynolds numbers.

4. To conducts a numerical simulation to analyze the aerodynamic performance, including power and torque coefficients, of a traditionally shaped Savonius wind turbine equipped with three diffusers of different configurations.
5. To develop a multi-objective maintenance optimization strategy using the Whale Optimization Algorithm (WOA).
6. To evaluate the economic and operational benefits of optimized maintenance planning in reducing production losses and maximizing turbine availability.

Significance of the Study

This study contributes to the wind energy field by providing insights into physical performance analysis and operational decision-making. The investigation of blade aero-structural performances supports the design of more reliable turbine blades, while the optimization of maintenance planning addresses real-world challenges associated with system downtime and high operational costs.

Overview of the Structure

This dissertation is organized as follows:

- **Chapter 1** presents a General Overview of Wind Turbines including Physics and Operating Principle, Types of Wind Turbines, Major Components of a Wind Turbine, Wind Turbine Classification, Wind Turbines Maintenance, Advantages of Wind Energy and Challenges and Limitations.
- **Chapter 2** Details an Analysis of structural responses of a horizontal axis wind turbine at maximum aerodynamic performance.
- **Chapter 3** Presents an Investigation of Aerodynamic Performances and Airflow Patterns over rotating Airfoils through 2D Unsteady Simulations. And Provides a Performance Analysis of Savonius Wind Turbine Equipped with Three Diffusers of Different Configurations Under Variable Tip Speed Ratios.
- **Chapter 4** Presents a Multi-objective optimization of wind turbines maintenance using the Whale Optimization Algorithm.

Chapter 1: Overview of Wind Turbines

1.1 Introduction

This chapter aimed at giving an overview and an insight into most aspects of wind energy. These topics include a historical background; the reasons for the interest in wind energy; challenges facing the wind turbine industry; the wind turbine's anatomy and its major categories; and the applications of wind turbines.

1.2 Historical Background

The utilization of wind as a source of energy has a deep-rooted history spanning over a thousand years. Throughout this period, wind energy has served diverse roles, evolving from mechanical work applications to a viable source of electrical power. Historically, it played a critical role in sustaining agricultural and economic activity, particularly before the widespread use of fossil fuels. Wind power, being a decentralized and renewable energy source, offered a valuable solution during times when other energy carriers were either unavailable or technologically underdeveloped. the development of wind energy can be conceptually divided into four major historical phases, each influenced by socio-economic, technological, and geopolitical shifts. The **Classical Period (600–1890)** saw widespread use of windmills for mechanical power, particularly in Europe. The **Electricity-Generating Phase (1890–1930)** introduced wind-powered electrical generators but declined with the rise of fossil fuel availability. The **First Innovation Period (1930–1960)** emerged during resource shortages around World War II, focusing on rural electrification and aerodynamic advances, but waned again as fossil fuels became more accessible. The **Second Innovation Phase (post-1973)** was catalyzed by the oil crisis and growing environmental awareness, marking the onset of modern wind energy technology and the transition toward industrial-scale wind turbine production.[1]

Figure 1: Historical development of the use of wind as a source of energy.[1]

1.3 Wind Turbines

Simple sails or blades that are positioned around a rotor to catch the wind and transform its kinetic energy into rotational energy constitute the basic principle of wind energy. Instead of the original windmills being used to grind grain or pump water, modern wind turbines use rotational energy to power a generator that generates electricity. The vertical axis wind turbines (VAWTs), which have their axis of rotation vertical to the ground and almost perpendicular to the wind stream, and the horizontal axis wind turbines (HAWTs), with their axis of rotation horizontal to the ground and almost parallel to the wind direction, are the two main configurations that have resulted from the current development of wind turbines[2]. The two major categories are depicted schematically in Figure 2.

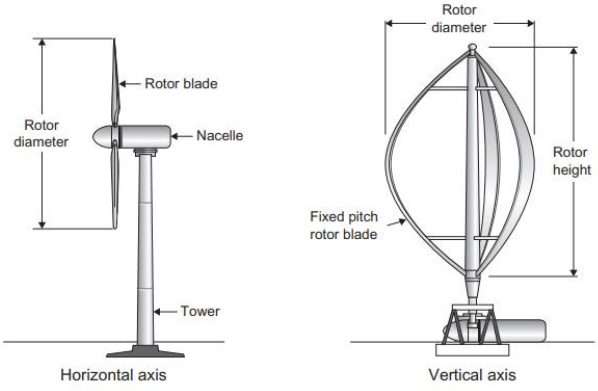

Figure 2: Horizontal and vertical axis wind turbine configurations[2].

1.4 Physics and Operating Principle

Wind turbines operate based on the principles of **aerodynamics and energy conversion**. The wind's kinetic energy is captured by the blades, generating lift and drag forces that induce rotor rotation. The kinetic energy in wind is governed by the equation:

$$E_k = 1/2\ \rho\ Ar\ \upsilon^3 \quad \ldots\ldots (1)$$

where ρ is air density, Ar is the swept area, and υ is the wind speed. The output power is therefore highly sensitive to wind speed[3].

The rotational motion is transferred via a shaft to a generator—either directly or through a gearbox—which produces electricity. The theoretical maximum energy extraction from the wind is limited by **Betz's Law**, which sets a ceiling of 59.3% efficiency [4].

1.5 Types of Wind Turbines

Wind turbines come in two main configurations:

1.5.1 Vertical Axis Wind Turbines VAWTs

A vertical axis wind turbine has vane mounts on its vertical shaft that catch the wind and transform its kinetic energy into rotational energy. At ground level, a generator connected to the vertical shaft produces electricity. The rotor of a VAWT is turned by two aerodynamic mechanisms: drag and lift-mechanism. One of the most recognized lift-based Vertical Axis Wind Turbine (VAWT) designs is the Darrieus turbine, originally developed by French engineer Georges Darrieus. This turbine features a vertical central shaft to which two slender, curved aerofoil blades are attached, forming a distinctive bow shape. Each blade is fixed at both the top and bottom of the shaft, enabling wind energy capture through aerodynamic lift. The H-shaped rotor design, called the Giromill, is another configuration of vertical axis wind turbine made by Georges Darrieus himself. Sigurd J. Savonius invented the Savonius wind turbine in 1925 as a simple vertical axis wind machine. It was originally constructed with two half-cylindrical blades arranged in an "S" shape. Mechanical power is produced as a result of the difference in drag force between the concave side of the one-half cylindrical blade and the convex side of the other blade. Several types of vertical-axis wind turbines are shown in Figure 3. Vertical-axis wind

turbines are notable for their lack of sensitivity to wind direction. The placement of the gearbox and generator at the bottom of the vertical shaft at ground level simplifies the structural requirements of the tower and makes maintenance easier. Another advantage is that the rotor's turning speed can be extremely high. Unlike a much more typical horizontal axis turbine, a vertical axis wind turbine typically does not start itself when the wind blows. The rotor's blades must pass through aerodynamically dead zones as it rotates. As a result, the overall system efficiency may be inferior. There are some other main disadvantages as well. One of them is that the rotor is too close to the ground or sea surface to take advantage of the best wind conditions.[5]

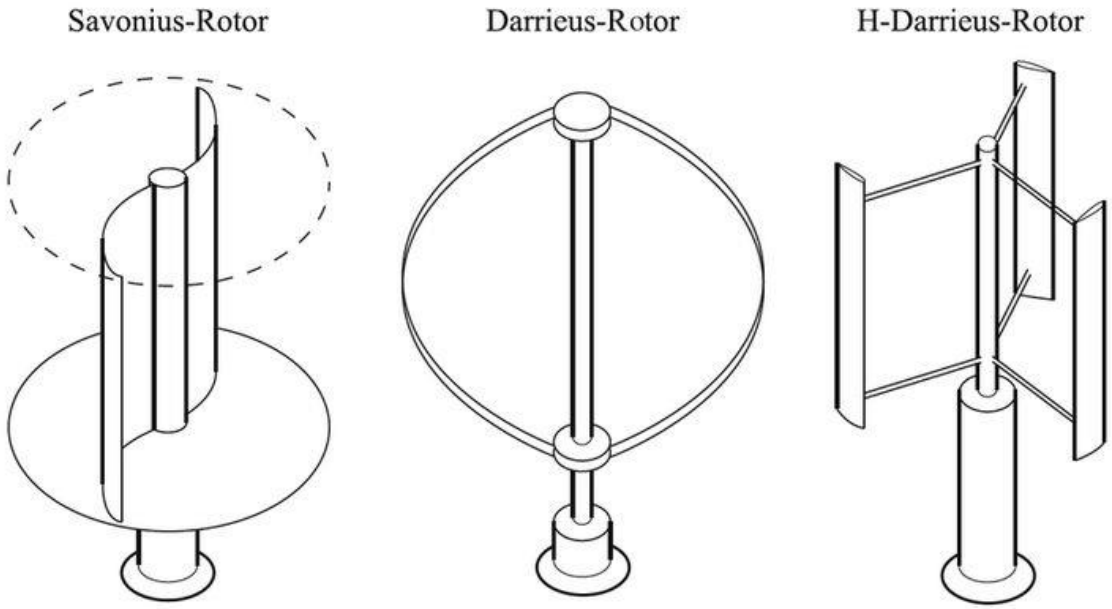

Figure 3: Several types of Vertical axis wind turbines.[5]

1.5.2 Horizontal Axis Wind Turbines HAWTs

The horizontal-axis wind turbine (HAWT) features a rotor—typically comprising multiple blades—that captures kinetic energy from the wind and converts it into rotational motion. This rotor is mounted on a horizontally aligned shaft positioned atop a tall tower. The shaft is mechanically linked, often via a gearbox, to a generator that converts mechanical energy into electrical power. The most prevalent configuration in modern wind energy systems is the three-bladed, upwind HAWT mounted on a tubular tower. This design has become the industry standard over the past two decades for both onshore and offshore wind farm installations.[6]

1. The three-bladed rotor has become the industry standard for utility-scale wind turbines, offering an optimal compromise between cost and balance. While turbines with varying blade counts have been explored, additional blades improve balance and reduce centrifugal stress at lower rotational speed needed for ideal energy capture, but significantly increase cost. Conversely, fewer blades reduce costs but introduce mechanical and dynamic challenges.
2. In a conventional horizontal-axis wind turbine, the drivetrain begins with the hub, which is connected to the main shaft. This shaft transmits mechanical rotational energy to a generator located at the opposite end, where it is converted into electrical energy—typically in the form of alternating current. A gearbox is often integrated between the rotor hub and the generator to adjust the rotor's relatively low rotational speed to the higher speed required by the generator.

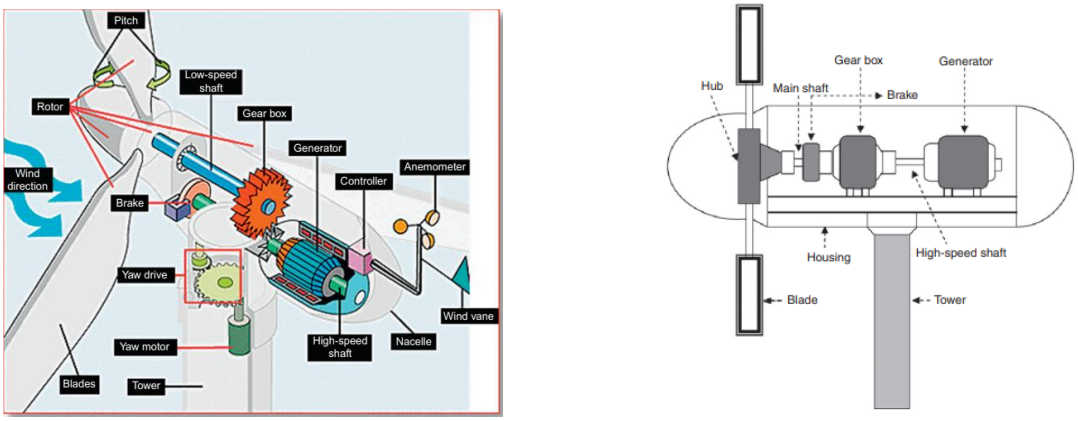

Figure 4: drivetrain principal components of a horizontal axis wind turbine.[6]

3. The nacelle, which is situated atop the wind turbine tower, houses the drive train. The components are protected from the weather by the nacelle. To guarantee that the rotor is constantly facing the wind, the entire tower-top structure is attached to the tower by a bearing that permits the nacelle to spin along a vertical axis. To keep its orientation as the wind direction changes, the nacelle needs to include a yawing motor that can shift the tower-top structure as necessary.
4. Usually, the tower that the nacelle is installed atop is composed of tubular steel. The tower's base will have a greater diameter than its summit. There are other building

techniques, such using concrete, which is often more costly than steel. lattice steel towers are now rare, with the exception of small capacity devices. Tripods, poles, and guy-wires are additional tower constructions that tiny wind turbines employ.

5. A big utility wind turbine's tower will have a lift to reach the nacelle, and a transformer at the ground level to increase the machine's power voltage before it is sent to the grid, often through a local substation.
6. The tower and turbine need a sturdy base to keep the wind from bringing the construction down. On land, it is usually a huge concrete structure that is frequently reinforced with steel. The tower's ability to withstand the forces of the wind depends on the strength of the soil in which it is buried. More intricate foundations, such tripods with several legs and monopiles pushed into the sea bed, are commonly used for offshore buildings.

Because the blades of horizontal axis wind turbines (HAWT) revolve near the center of gravity, they are more stable. Additionally, the blades' efficiency is better since they take more power from the wind and rotate regularly to the wind speed. Long towers contribute to increased efficiency even more. During storms, failure is avoided by controlling the blade pitch angle. Despite these advantages, HAWTs require additional control, including pitch and yaw control and a brake mechanism for strong winds.[6]

1.6 Wind Turbine Classification

Wind turbines are classified according to multiple key criteria, each influencing their design, application, and performance[7]:

1.6.1 By Size (Capacity)

1. Small (<10 kW): Ideal for residential or off-grid use, such as rooftop or rural applications engineering.
2. Intermediate (10–250 kW): Used for community-based systems and hybrid installations.
3. Large (>250 kW to multi-megawatt): Applied in large-scale onshore and offshore wind farms.

1.6.2 By Location

1. Onshore: dominates global installed capacity; more cost-effective but subject to terrain and land constraints.
2. Offshore: Offshore turbines leverage higher and more consistent wind speeds but necessitate robust mechanical and structural designs (e.g., corrosion resistance, large-diameter main bearings)

1.6.3 By Drive Mechanism

1. Geared (with gearbox): Conventional design uses a gearbox to step up rotor speed for standard generators, but gearboxes often become maintenance-critical components.
2. Direct-drive: Eliminates the gearbox by coupling the rotor directly to a slow-speed generator (often a permanent magnet design). Benefits include fewer moving parts and reduced maintenance; however, they require large, expensive generators and use significant quantities of rare-earth materials

1.6.4 Upwind vs. Downwind

1. Upwind Turbines In upwind configurations, the rotor is positioned on the windward side of the tower—meaning the blades face into the wind before it reaches the tower structure. This is the most common design in modern wind energy systems, especially for large-scale Horizontal Axis Wind Turbines (HAWTs).[8]
    a. Advantages:
        i. Minimized tower shadow effect: Since the wind hits the blades before the tower, turbulence and wake interactions are reduced, leading to smoother power output and better structural performance.
        ii. Higher efficiency: Aerodynamic performance is generally improved due to cleaner airflow over the blades.
    b. Challenges:
        i. Requires a yaw mechanism to continuously align the rotor with the wind direction, adding complexity and maintenance needs.
        ii. Risk of blade-tower collision in extreme deformation cases, requiring careful control of blade stiffness and clearance.
2. Downwind Turbines In downwind configurations, the rotor is located on the leeward side of the tower—meaning wind passes over the tower before reaching the blades.[8]

a. Advantages:
    i. No yaw system needed: The wind naturally aligns the rotor, reducing mechanical complexity.
    ii. Greater design freedom: Blades can be more flexible, bending away from the tower during high wind loading.
b. Challenges:
    i. Tower shadowing effects: The tower causes wind turbulence before it reaches the blades, leading to periodic loading, power fluctuations, and potential fatigue issues.
    ii. Acoustic noise and vibrations are typically higher, making downwind turbines less favored for commercial installations.

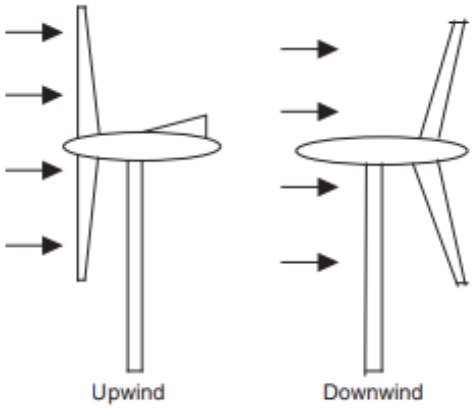

Figure 5: Upwind vs. Downwind

1.7 Necessity of Using a Wind Turbine

For several decades, the development of renewable and clean energy has been a critical issue because of the decline in the supply of traditional energy sources and the environmental issues related to their use in power generation. One of the most popular renewable energy sources is wind power. The need for wind turbines is related to their ability to provide a good answer to some environmental and economic issues. Wind turbines have many advantages for generating electricity.[9]

1. Provide a Clean source of energy. The fact that wind energy creates virtually no pollution is one of the strongest arguments in favour of its expansion. It produces power without releasing carbon dioxide.

2. Sustainability. Energy can be captured and transmitted to the grid whenever the sun shines and the wind blows.
3. Location. Almost any location, including existing farms, may have wind turbines built. Good windy spots, such the summits of mountains or the valleys between hills, are not in conflict with other land uses or urban expansion.
4. Compatibility with other land uses. Wind turbines can be installed on pastureland with minimal disruption to livestock and farming operations. Other areas to consider for wind farms include areas near landfills, the sides of roadways, and major roads where urban development is unlikely to occur.
5. Reduced transportation costs for electricity from distant power plants. Transporting alternating current electricity over long distances is costly due to the cost of the cables and pylons, as well as the loss of power due to electrical resistance in the cables.
6. National security. The wind is a free source of energy. Being independent of foreign fuel sources is a great advantage.
7. Water conservation. Traditional power plants that use coal, oil, gas, or nuclear fuel all use a lot of water. Wind farms do not use any water.
8. Reduction of destructive mining. Pumping oil and gas (particularly from ocean beds) and mining coal or uranium all have serious environmental consequences for the sea or land. Wind farms are relatively benign in this regard, and farming and other activities can take place around the turbines because the actual action takes place more than a hundred meters above the ground or sea.
9. Short commissioning time. Wind farms can be built in a relatively short period of time, and it is not impossible to achieve electricity production in as little as two or three years. This is comparable to the many decades required to design, build, and commission a nuclear power plant.
10. Creation of jobs and local resources.
11. Source of income for farmers, ranchers and foresters and grid operators.
12. Diversification of power supply.
13. International cooperation.

1.8 Challenges Facing the Wind Turbine Industry

There are of course a number of challenges associated with harnessing the power of the wind. [9]

1. The intermittency of wind.
2. Good sites are often in remote locations. The best windy locations are frequently found in hilly, mountainous regions far from urban areas. This means that electricity generated onshore must be transferred to users via expensive high-voltage cables.
3. Noise pollution.
4. Turbine blades can damage wildlife.
5. Safety. The greatest safety issue linked with turbines, once installed, is the chance of a blade becoming adrift, causing catastrophic harm to people or animals nearby.
6. Frequency of light and shadows.
7. Initial cost. The initial cost of establishing a wind farm is likely the most significant disadvantage. It is for this reason that many governments around the world continue to provide subsidies. This is balanced by the turbine's long-term financial and environmental benefits.

1.9 Maintenance in Wind Turbines

Wind turbine maintenance involves a systematic approach to ensuring turbines remain efficient, safe, and fully operational throughout their extended service life. Maintenance activities encompass inspections, lubrication, cleaning, and repairs, which are systematically executed to prevent failures and maintain performance.[10, 11]

- Inspection Protocols

  Periodic inspections are conducted by trained technicians to evaluate the condition of critical components, including rotor blades, nacelle, tower, generator and associated subsystems. These inspections utilize visual, sensor-based, and non-destructive testing methods to identify early signs of wear, corrosion, or structural damage, thereby preempting catastrophic failures.

- Cleaning Procedures

Environmental exposure leads to the accumulation of dirt, debris, and biological matter on turbine components, particularly blades, which can compromise aerodynamic efficiency. Regular cleaning restores optimal performance and prevents long-term degradation due to surface abrasion or contamination.

- Lubrication Practices

Lubrication is essential for reducing friction and wear in rotating components such as gearboxes, yaw systems, and rotor shafts. High-performance lubricants are applied at scheduled intervals to enhance component durability, lower failure rates, and reduce maintenance costs.

- Repair Operations

When failures occur, technicians undertake repairs, including the replacement of damaged parts. These operations often involve complex logistics, particularly for offshore or remote installations, requiring the transport of heavy equipment to elevated or confined spaces. Predictive maintenance strategies aim to minimize such interventions by addressing issues proactively.

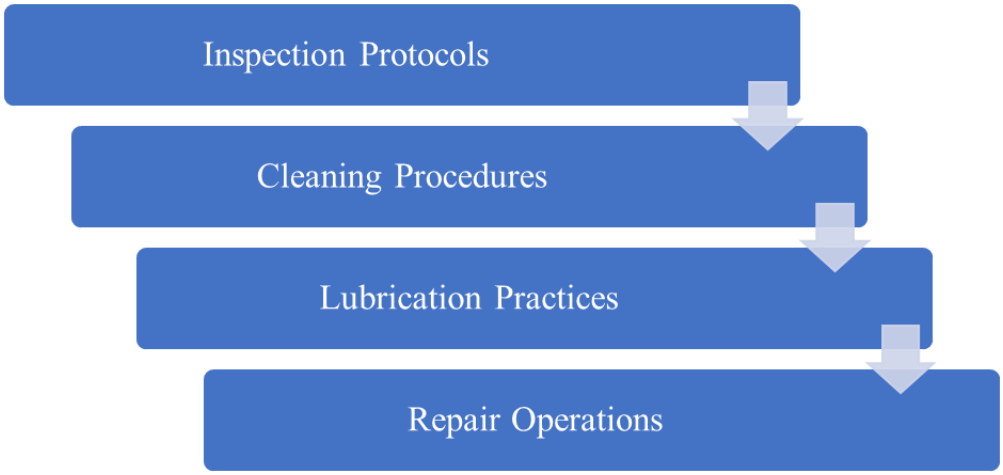

Figure 6: Maintenance activities.

1.10 Key Components Requiring Maintenance

Wind turbines comprise several subsystems, each requiring targeted maintenance to ensure reliability and performance.[12] [13]

The following components are critical:

- Rotor components: Regular inspections detect cracks, erosion, or delamination. Cleaning and minor repairs maintain aerodynamic efficiency, while structural health monitoring ensures long-term integrity.
- Tower Structure: Evaluated for corrosion, bolt integrity, and structural stability to prevent catastrophic failure.
- Nacelle Housing: Inspected for weatherproofing, seal integrity, and mechanical damage to protect internal components.
- Generator: Requires lubrication, bearing alignment, and insulation testing to maintain electrical efficiency and prevent overheating.
- Gearbox Assembly: Monitored for oil quality, leaks, and wear to mitigate the high failure rates associated with gears and bearings.
- Yaw and Pitch Systems: Inspected for mechanical and electrical functionality to ensure proper wind alignment and blade angle optimization.
- Bearings: Regular lubrication and vibration monitoring prevent wear and overheating in critical rotating components.
- Electrical Systems: Wiring, control panels, and lightning protection systems are inspected to ensure operational safety and reliability.
- Hydraulic and Cooling Systems: Monitored for leaks, pressure anomalies, and thermal performance to prevent system failures.
- Foundation: Assessed for cracks, erosion, or shifting to maintain structural stability.
- Safety and Monitoring Systems: Fire suppression, braking, and SCADA systems are tested to ensure compliance and real-time performance tracking.

1.11 Common Failure Modes in Wind Turbines

Historically, to fulfill the demands of wind energy production, wind farms were predominantly constructed in challenging environments, such as offshore marine locations or remote mountainous regions, subjecting them to severe operational conditions. As critical components of wind farms, wind turbines are inherently exposed to these harsh environments. Variable and unpredictable loads arising from factors such as dust, humidity, temperature fluctuations, air pressure variations, and wind gusts impose significant

alternating stresses on primary load-bearing structures, notably blades and towers. These conditions exacerbate tribological phenomena—including wear, fatigue, and corrosion—leading to component degradation and system failures. With the global proliferation of wind turbine installations, new challenges have emerged. Failures are often attributed to mechanical damage surpassing design fatigue thresholds, compounded by novel failure modes stemming from material aging, manufacturing imperfections, and evolving rotor size standards. Consequently, the increasing deployment of both onshore and offshore wind turbines has correlated with a rise in operational incidents.[14]

Figure 7 illustrates the global incidence of wind turbine damage cases from 2000 to 2017. The data indicate a direct correlation between the growing number of wind turbine installations worldwide and an increase in accident frequency during this period.

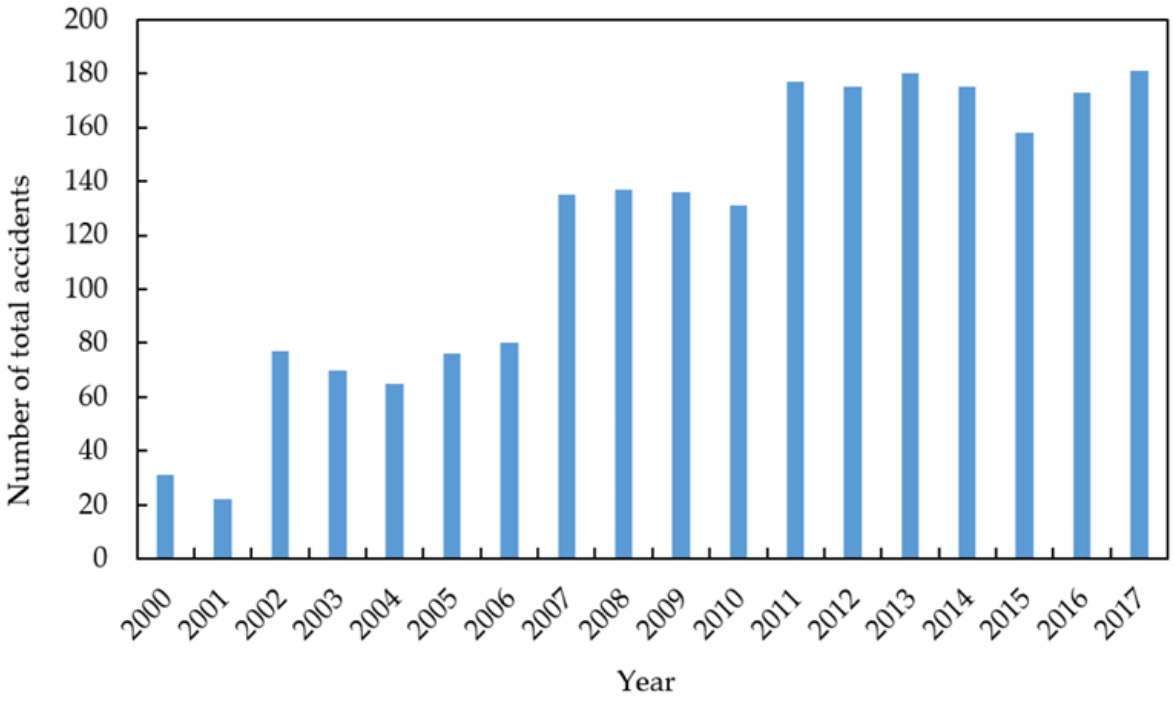

Figure 7: Global incidence of wind turbine damage cases from 2000 to 2017.[14]

Wind turbines are susceptible to several prevalent failure modes, including blade failure, gearbox failure, pitch system failure, and yaw system failure.[14]

The primary fault characteristics and their underlying causes are outlined below:

- Failure of blade

The manufacturing cost of wind turbine blades accounts for approximately 15–20% of the total turbine cost, highlighting their significant economic impact. Blades, fully exposed to the external environment, endure harsh operating conditions such as high altitudes, ultraviolet radiation, abrasive particles like sand and dust, lightning strikes, heavy rainfall, freezing rain, ice, snow, salt corrosion, and extreme wind events including typhoons. These severe and variable environmental factors increase the likelihood of blade failure, underscoring the critical need for advanced condition monitoring systems, early warning mechanisms, and robust operations and maintenance (O&M) strategies to ensure reliability and durability. [14]

Common blade failure modes include

- fracture and cracking due to cyclic loading, material fatigue, or manufacturing flaws such as poor curing or uneven composite layering, which compromise structural integrity.
- Lightning-induced damage results from high-energy strikes causing thermal degradation, surface burns, or structural separation, particularly at the blade tip or leading edge.
- Surface abrasion and localized cracking stem from erosion by rain, hail, or airborne particulates, leading to surface degradation, micro-cracks, and water infiltration that weaken adhesive bonds and composite structures.

These failures are often worsened by manufacturing defects, such as folding, inadequate resin curing, or inconsistent layering, further impairing blade performance and longevity.

Figure 8: Common blade failure modes.[14]

- Failure of gearbox

The gearbox, a critical component of wind turbines, comprises numerous gears, with gear-related failures accounting for approximately 60% of all gearbox malfunctions. These failures predominantly affect the gear teeth, manifesting as tooth surface corrosion due to environmental exposure, tooth surface wear from prolonged mechanical stress, tooth surface bonding caused by excessive frictional heat or inadequate lubrication, and tooth fractures resulting from fatigue or overloading. [14]

- Failure of pitch system

The pitch system, essential for adjusting blade angles to optimize power output and ensure operational safety, is susceptible to several failure modes. These include pitch shaft cabinet battery undervoltage, which compromises the power supply for blade angle control; abnormal hub detection data, resulting from sensor malfunctions or communication errors that disrupt accurate blade positioning; and excessive paddle angle deviation, caused by mechanical wear, hydraulic system failures, or control inaccuracies, leading to reduced aerodynamic efficiency and increased structural loads. [14]

- Failure of Yaw system

The yaw system, responsible for aligning the turbine with the wind direction, also experiences distinct failure modes. These encompass abnormal noise, indicative of mechanical wear, inadequate lubrication, or misalignment in yaw gears or motors; yaw drive machinery jamming, caused by debris accumulation, gear wear, or motor failure, which prevents proper turbine orientation; and inaccurate yaw positioning, resulting from sensor drift or control system errors, leading to suboptimal wind capture and heightened structural stresses. [14]

Figure 9 and Table 1 provide an abstract representation of the failure modes affecting key wind turbine components, along with their primary causes.

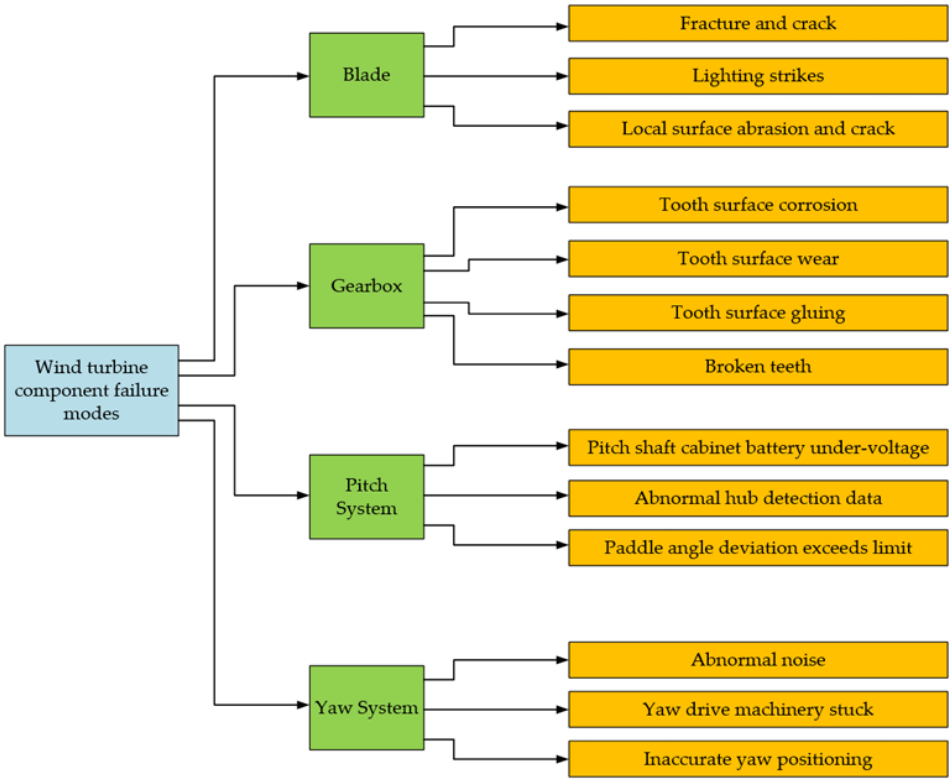

Figure 9: The failure modes of key wind turbine components.

Table 1. Failure mode of each component and a main cause.

Failure Mode of Each Component	Main Causes
Fracture and cracking	Design defects; poor quality; changes in process; lack of production experience
Lightning strikes	Cracks in components; fouling or damage of blade surface
Local surface abrasion and cracking	Abrasion by wind, sand, and water vapor; extreme weather conditions
Tooth surface corrosion	Excessive water content in lubricating oil; wet operating environment
Tooth surface wear	Machining inaccuracies; material defects; short-term overload; long periods of inactivity
Tooth surface gluing	High-speed or low-speed heavy load
Broken teeth	Fatigue; overload
Pitch shaft cabinet battery under-voltage	Shaft cabinet battery under-voltage; charging loop fault
Abnormal hub detection data	Communication failure
Paddle angle deviation exceeds limit	Rotational overrun
Abnormal noise	Degradation of driving motor oil; transmission bearing damage; broken ring gear; uneven ring clearance; lack of grease in yaw system; excessive brake damping pressure
Yaw drive machinery stuck	Planetary gear train failure
Inaccurate yaw positioning	Brake failure of yaw motor

1.12 Different types of loads act on the blades

The structural integrity of a wind turbine is paramount in determining its maximum permissible wind speed, with the blades being particularly susceptible to various loads induced by airflow. These forces generate stresses within the blade, potentially leading to structural damage. Additionally, blade vibrations pose a significant concern, as they can exacerbate fatigue and accelerate failure. Addressing these challenges requires the selection of robust materials capable of withstanding continuous and dynamic loading conditions.[15] The primary types of loads acting on wind turbine blades are categorized as follows:

- Steady load: Constant forces resulting from uniform airflow, which impose static stresses on the blade structure
- Cyclic load: Periodic variations due to rotor rotation, wind shear, or yaw motion, contributing to material fatigue.
- Transient load: Time-varying forces caused by sudden wind gusts or changes in wind direction, necessitating dynamic structural analysis
- Stochastic load: These loads are similarly time-varying, but they cannot be expressed as a function since the load value changes randomly over time.
- Resonance-induced loads: These are loads caused by the dynamic reaction of the blade. These loads occur when the wind turbine blade is stimulated to its native frequency.

These loads are typically generated by high winds and can inflict significant damage on the turbine blade. Loads on the blades are caused primarily by aerodynamic force, gravity, dynamic vibrations, and the effects of secondary subsystems such as gears. Aside from these loads, inertia and the gyroscopic effect might cause them. Another major concern is the induced vibrations caused by the blades' excitation to their natural frequency. These vibrations might severely destroy the blades. The primary cause of turbine blade failure is material fatigue. Material fatigue refers to damage induced by cyclic stresses. A continuous load on the blades can cause material fracture because the stress induced exceeds the maximum allowable stress in the blades. The sort of stress

created varies each segment of the blade and is completely dependent on the geometry of the blade.[15]

1.13 Maintenance Strategies for Wind Turbines

Wind turbine maintenance strategies are traditionally classified into corrective and preventive approaches, each with distinct methodologies and implications for operational efficiency[10]. Corrective maintenance, often referred to as unscheduled or failure-based maintenance, is performed in response to turbine breakdowns, detected faults, or component failures. This reactive approach typically necessitates immediate repairs or part replacements, resulting in unplanned downtime, which makes it the most-costly maintenance strategy. Wind farm operators aim to minimize reliance on corrective maintenance due to its high economic and operational impact.[16]

In contrast, preventive maintenance (PM) seeks to repair or replace components before failures occur, thereby enhancing reliability and reducing downtime. The most common form of PM is scheduled maintenance, also known as time-based or planned maintenance. This approach involves performing maintenance tasks, such as oil and filter changes, bolt tightening, etc. at fixed intervals as prescribed by equipment suppliers, irrespective of the component's actual condition. While effective in reducing failure rates, scheduled maintenance often leads to more frequent interventions than necessary, potentially underutilizing the service life of components and increasing operational costs. [10] [16]

An alternative to scheduled maintenance is condition-based maintenance (CBM), which leverages continuous monitoring and advanced inspection techniques to identify early signs of faults and determine maintenance needs proactively. CBM relies on the acquisition, processing, analysis, and interpretation of data from condition monitoring systems (CMS), enabling operators to select optimal maintenance actions before failures occur. Techniques such as vibration analysis, oil debris monitoring, and thermography are integral to CBM, providing real-time insights into component health. Research demonstrates that CBM significantly reduces maintenance costs, enhances operational safety, and decreases the frequency and severity of in-service failures, making it a preferred strategy for modern wind farms.[10] [16]

Table 2. The key characteristics of maintenance strategies

Strategy	***Type***	***Objective***	***Advantages***	***Limitations***	***Typical Cost Impact***
Corrective Maintenance	Unplanned	Repair post-failure	Minimal planning, only when needed	High costs, downtime, safety risks	High (emergency repairs)
Scheduled Maintenance	Planned	Prevent failure via regular tasks	Predictable, reduces major failures	Over-maintenance, underutilizes components	Moderate (frequent tasks)
Condition-Based Maintenance	Planned	Prevent failure via real-time monitoring	Cost-effective, extends component life	High setup costs, requires expertise	Low (optimized tasks)

1.14 Concepts and Methods for Wind Turbines Condition Monitoring

Condition monitoring (CM) plays a crucial role in ensuring the reliability and operational efficiency of wind turbines by continuously assessing the condition of critical components and enabling early fault detection. A Condition Monitoring System (CMS) integrates multiple subsystems designed to monitor turbine components such as blades, gearboxes, and generators using data acquisition and signal processing techniques. Various monitoring methods are applied in wind turbines, including vibration analysis, oil analysis, temperature measurement, strain measurement, optical fiber monitoring, visual inspection, acoustic emission, ultrasonic testing, thermography, and radiographic inspection. Vibration analysis and oil analysis are widely used for detecting mechanical faults in rotating components, while temperature and strain measurements help evaluate thermal behavior and structural integrity. Advanced techniques such as optical fiber monitoring and acoustic emission provide high-precision structural health monitoring, whereas ultrasonic testing and thermography allow for the detection of internal defects and abnormal thermal patterns. Visual inspection remains a complementary technique for identifying surface damage, although it is limited by subjectivity. Radiographic inspection can reveal internal structural flaws but is less commonly applied due to cost and operational complexity. The integration of these techniques within CMS enhances fault detection accuracy, supports predictive maintenance strategies, and contributes to improved reliability and longevity of wind turbine systems. [12],[17]

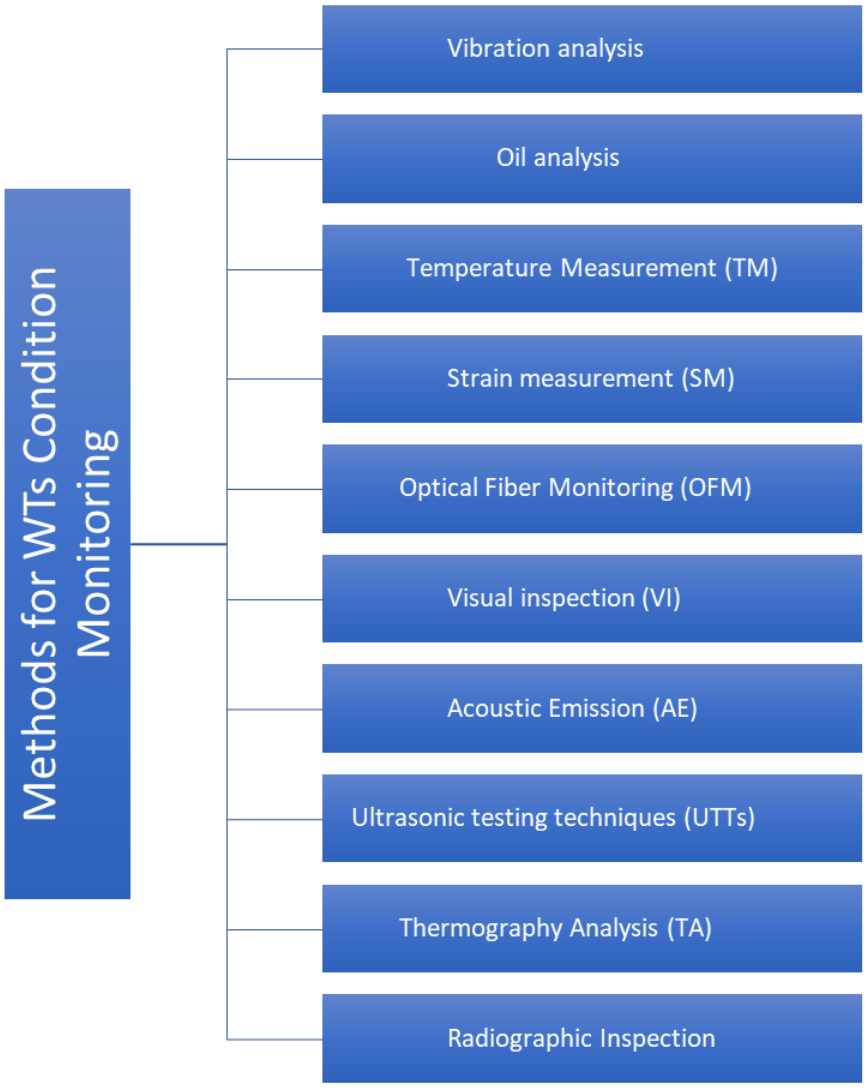

Figure 10: Methods for Wind Turbines Condition Monitoring.

1.15 Optimality criterion

1.15.1 Minimum cost

One of the primary objectives in maintenance optimization is minimizing the total operational expenditure. This includes direct maintenance costs (e.g., spare parts, labor, transportation, tools), indirect costs (e.g., logistics, downtime penalties), and capital depreciation due to component failure. Cost minimization strategies often focus on scheduling preventive interventions to avoid high-cost corrective repairs. This is especially critical for offshore turbines where reactive maintenance is significantly more expensive due to access limitations.[18]

1.15.2 Minimum production loss (maximum power output)

Wind farms, vital for renewable energy, face various energy production losses that reduce their efficiency. These losses stem from interactions between turbines, operational downtime, inefficiencies in turbine performance or electrical systems, and environmental factors. Understanding and mitigating these losses is crucial for maximizing energy output and ensuring economic viability.[18]

- Wake Losses

Wake losses occur when upstream turbines create turbulence and reduced wind speeds, affecting downstream turbines. This can significantly lower power output and increase wear on turbine components. While traditionally overlooked in maintenance planning, newer strategies are beginning to account for these effects to optimize energy production.

- Availability Losses

Availability losses are another sort of wind farm production loss. When a wind turbine fails unexpectedly, the entire system shuts down until the necessary repairs are made. An unexpected failure causes significant production losses in wind farms. Aside from random failures, power loss can be caused by scheduled PM tasks, which typically shut down wind turbines during maintenance. Wind farm operators have expressed a strong interest in optimising maintenance techniques in order to reduce overall production losses (or maximise total power output).

- Other Loss Factors

Turbine performance losses arise from suboptimal operation, such as misalignment or blade degradation. Electrical losses occur during power conversion and transmission, while environmental factors like icing or soiling can further reduce efficiency. Intentional curtailments, often for regulatory reasons, also contribute to lost production.

1.15.3 Maximum availability/reliability

Availability is defined as the proportion of time that a wind turbine is operational and capable of producing energy. High availability (usually greater than 97%) is considered a

performance benchmark for modern turbines. Maintenance plans that maximise availability frequently rely on predictive diagnostics and optimised logistics to reduce the mean time to repair (MTTR) while increasing the mean time between failures (MTBF).[18]

Figure 11: Optimality criterion.

Chapter 2: Analysis of structural responses of a horizontal axis wind turbine.

2.1 Introduction

Wind turbines have become a cornerstone of global renewable energy strategies due to their ability to harness an abundant, clean, and inexhaustible resource—wind. The fundamental principle of wind energy conversion is the transformation of kinetic energy from moving air into mechanical energy through the rotation of turbine blades, which is subsequently converted into electrical energy via a generator. This process is both environmentally sustainable and economically viable, especially as technological advancements continue to reduce the cost per kilowatt-hour of wind-generated electricity [3].

Modern wind turbines are broadly classified into two categories based on the orientation of their rotational axis: Horizontal-Axis Wind Turbines (HAWTs) and Vertical-Axis Wind Turbines (VAWTs). Among these, HAWTs are the most prevalent and commercially successful due to their higher energy efficiency, superior scalability, and established technological maturity. HAWTs typically consist of three primary components: the rotor (including blades and hub), the nacelle (housing the gearbox and generator), and the supporting tower. The aerodynamic performance of the rotor is a critical determinant of the overall energy output of the turbine [8].

Wind turbine performance is influenced by various factors, including blade geometry, material properties, wind speed variability, atmospheric turbulence, and site-specific topography[19]. As turbines increase in size to capture more energy, the structural loads they experience also become more significant. These loads include aerodynamic forces, gravitational forces, and inertial forces due to rotation and yaw motion. Managing these loads is essential to ensure structural integrity, maintain aerodynamic efficiency, and extend the operational lifespan of the turbine [20].

The design of wind turbine blades is particularly complex, as it requires balancing aerodynamic performance with structural resilience. Blades must be lightweight to reduce gravitational loading but strong enough to withstand cyclic aerodynamic forces. This

challenge is compounded by the need for flexibility to accommodate dynamic deformations, which in turn affect aerodynamic flow patterns and energy conversion efficiency [19]

To address these challenges, engineers and researchers have developed a variety of analytical and numerical modeling approaches. Computational Fluid Dynamics (CFD) is widely used to simulate airflow and predict aerodynamic loads, while finite element analysis is applied to evaluate structural responses such as stress, strain, and deflection. However, the coupling between aerodynamic and structural analyses—captured through Fluid-Structure Interaction (FSI) modeling—has emerged as a more accurate and holistic approach to wind turbine analysis.[21] ,[22]

2.2 Overview of related researches

In the realm of wind energy research, the study of Horizontal Axis Wind Turbines (HAWTs) entails a dual investigation: a meticulous examination of their aerodynamic performance and a profound analysis of blade elasticity. This dual focus highlights the intricate interplay between fluid dynamics and structural mechanics[15]. Numerous studies have delved into these distinct facets. (Cho and Kim) [23] conducted a wind tunnel experiment to explore the influence of wind velocity and rotational speed on the rotor performance of a scaled-down wind turbine. Their work considered the comparison of two surface condition of the blade named free transition and forced transition surfaces, their results showed the reduction by 15% of the maximum power coefficient in the case of forced transition compared to the free transition condition. A study by (Cho et all) [24].employed a comprehensive approach, combining experimental and numerical methods to investigate the performance of a model wind turbine. Experimental tests resulted in a peak power coefficient of 0.448. Concurrently, numerical simulations were executed. The outcomes of their study revealed a notable congruence between computed and measured performance at the model scale, bolstering the potential for accurate extrapolation of high-resolution CFD predictions to full-scale turbine conditions. Several recent papers delve into the examination and validation of turbulence models to assess the accuracy and reliability of numerical simulations within the context of wind turbine aerodynamics. The studies conducted by Ji, Zhong, et al. (2022) [25]. Muiruri, Motsamai et al. (2019) [26]. Moshfeghi, Song et al. (2012) [27]. Mo and Lee (2012) [28] and Tachos, Filios et al. (2010, 2009) [29] [30] cover a spectrum of turbulence models.

Their findings reveal varying degrees of agreement and discrepancies in predicting aerodynamic properties, underscoring the critical importance of carefully selecting an appropriate turbulence model to ensure accurate simulations in similar wind energy applications. Another studies conducted by (Abdelsalam and Ramalingam 2014) [31], and (Abdelsalam, Boopathi et al. 2014) [32], have focused on analyzing wake characteristics in the near and far wake regions of horizontal axis wind turbines (HAWTs). In term of the horizontal Axis wind turbines aerodynamics Proprieties, (Sudhamshu, Pandey et al. 2016) [33] and (Thumthae and Chitsomboon 2009) [34] , conducted a numerical studies to investigate the impact of pitch angle on the performance of a horizontal axis wind turbine. Their study found that there exists an optimal pitch angle for the turbine to generate maximum power at a given wind velocity. A comprehensive study was conducted by (Yossri, Ayed et al. 2021) [35], using a computational fluid dynamics approach to investigate the impact of blade airfoil section and rotor diameter size on the power output of a small-scale wind turbine. Their study examined four airfoils along with three rotor diameter sizes (50, 75, and 100 cm) and considered the determination of the optimal point according to the verified geometrical parameters. (Khalafallah, Ahmed et al. 2019) [36] explored the impact of winglets on the turbine output of straight and swept blades in horizontal axis wind turbines. Through computational fluid dynamics (CFD) and parametric analysis, they found that turbines equipped with winglets and sweep showed a greater increase in output compared to those with straight or swept blades alone. Their study revealed a significant improvement in the coefficient of power by 4.39%.(Lipian et al.2020) [37] conducted a comprehensive investigation involving numerical aerodynamic and structural analyses of a small horizontal axis wind turbine. Their study considered various wind speeds for turbine's wind blades featured a Young's modulus of 3.40 and a Poisson's ratio of 0.39. Notably, their study highlighted the potential of Fluid-Structure Interaction (FSI) analysis in assessing the strength of unconventional materials and estimating the impact of blade deformation on rotor performance. The study by (Roul et all.2020) [38] explored the impact of blade pitch angle on the aerodynamic and structural characteristics of a Horizontal Axis Wind Turbine (HAWT) with several blade materials using an FSI approach. Their investigation spanned a range of wind velocities and highlighted the accepted values of the maximum deformation of the blade in consideration of the tower clearance limit. A large scale horizontal Axis Wind Turbine with composite blades is studied numerically in the work of (Wang, Quant et al.2016) [39], their study used a one-way Fluid-Structure Interaction approach, their study highlights the effects of several working conditions on the Maximum compressive- tensile stresses and tip deflections with their relation to the structural and material

limits. (Huque et al.2024) [40] explored the impact of three different tip shapes on horizontal axis wind turbine performance through a one way fluid-structure interaction. Their study focused on stress and deformation analysis along the blade span. Their Results suggest that modifying blade tips could effectively boost power generation without compromising structural strength. A fluid-structure interaction analysis is conducted by (Wenyan Li et al.2023), [41] of a horizontal axis wind turbine. their results showed a considerable effect of the rotation of the blade on the aerodynamic state and structural responses for a wind turbine studied near the ground. (Shi et al.2019) [42] performed a numerical calculation of the blade vibration characteristics under various wind and rotation speeds. Their findings showed that an increase in wind or rotation speed causes a nonlinear increase in the maximum span-wise displacement of the blade and in the Mises-stresses. (Thangavelu et al.2021) [43] presented a numerical aeroelastic analysis of two types of HAWT, the first with swept blades and the second with unswept blades. Taking into consideration the effects of yaw angle, their study showed that swept blades have better aeroelastic performance in terms of higher rotor power and lower deformation than unswept blades. It can be seen from the studies reviewed that while significant progress has been made in aeroelastic studies of HAWTs, certain critical gaps persist. In particular, there is a lack of comparative studies evaluating the impact of Young's modulus variations on blade deformation and aerodynamic efficiency. Additionally, further improvements in structural prediction methods are needed, particularly regarding the limitations of one-way and two-way FSI approaches in capturing realistic structural responses under aerodynamic loads. Addressing these gaps, the present study explores the complex relationship between fluid dynamics and structural mechanics in Horizontal Axis Wind Turbines (HAWTs), providing insights into their behavior under diverse operating conditions. The investigation considers tip speed ratios ranging from 1 to 8.1 and examines blade structural responses at the maximum aerodynamic coefficient (tip speed ratio of 6.1) across a spectrum of Young's modulus values from 5×10^{8} to 1×10^{10} Pa.

2.3 Numerical methodology and geometries description

The numerical methodology employed in this study comprises four key steps:

2.3.1 Geometry Construction and Mesh Generation

The turbine's geometry is constructed using the Design Modeller tool. During the geometry generation process, a one-third cylindrical domain is created, measuring 4R in diameter

and 4.5R in length, while considering the symmetric case. Within this computational domain, the blade is positioned at 1.5R from the inlet and 3R from the outlet, (where R is the wind turbine rayon) as illustrated in Figure 12. The geometric parameters closely follow those detailed in reference [44], with the wind turbine featuring trapped and twisted blades. Next, ANSYS Fluent Meshing is used to generate a computational mesh, employing a Tetrahedral mesh.

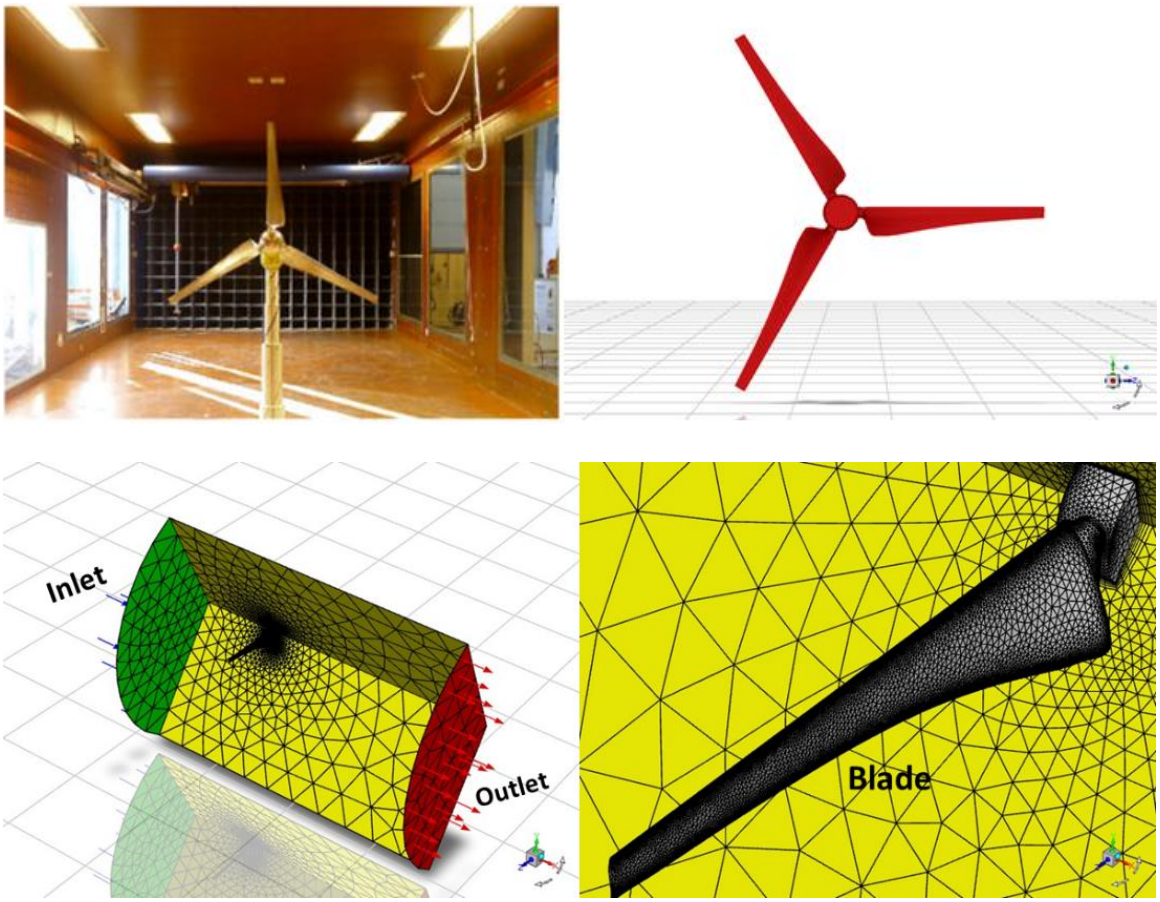

Figure 12: Upper-left: The Wind turbine from reference [44]; Upper-right: The simulated wind turbine, Bottom: The Computational Domain.

Table 3. Geometry and computational domain parameters

Category	Parameter	Specification / Value
Turbine Geometry	Turbine type	Horizontal Axis Wind Turbine (HAWT)
	Blade geometry	Twisted and tapered blades (NREL S826)
	Geometrical reference	Based on Ref. [44]
Computational Domain	Domain shape	One-third cylindrical domain (120° periodicity)
	Domain diameter	4R
	Domain length	4.5R
	Blade position from inlet	1.5R
	Blade position from outlet	3R

Mesh	Meshing tool	ANSYS Fluent Meshing
	Mesh type	Tetrahedral
	Mesh refinement	Local refinement near blade surface

Table 4. Blade definition Ref. [44]

r / R	c / R	α (deg)
0.016667	0.030000	–
0.050000	0.030000	–
0.10889	0.030000	–
0.12222	0.11000	38.000
0.15000	0.18096	37.055
0.18333	0.17802	32.544
0.21667	0.17114	28.677
0.25000	0.16250	25.262
0.28333	0.15335	22.430
0.31667	0.14434	19.988
0.35000	0.13578	18.034
0.38333	0.12782	16.349
0.41667	0.12050	14.663
0.45000	0.11379	13.067
0.48333	0.10766	11.829
0.51667	0.10207	10.753
0.55000	0.09696	9.8177
0.58333	0.092286	8.8827
0.61667	0.088002	7.9877
0.65000	0.084068	7.2527
0.68333	0.080446	6.5650
0.71667	0.077104	5.9187
0.75000	0.074014	5.3045
0.78333	0.071149	4.7185
0.81667	0.068487	4.1316
0.85000	0.066009	3.5439
0.88333	0.063697	2.9433
0.91667	0.061536	2.2185
0.95000	0.059512	1.0970
0.98333	0.057613	–0.71674

2.3.2 Solver Configuration

ANSYS Fluent is utilized for configuring the solver. The Single Moving Reference Frame approach [21] is implemented to simulate the wind turbine blade's rotation, the following boundary conditions were employed: At the upstream border, where the flow enters the domain, a velocity condition was added. Additionally, the downstream point where the flow leaves the domain was subjected to an ambient pressure condition. A non-slip wall was applied to the blade surface. A slip wall at the surrounding surface. Periodic boundary conditions were applied to the two lateral boundaries of the domain to simulate the 120° periodicity of the flow. The solver settings used were as follows: A pressure-based

solver with an absolute velocity formulation, along with a simple algorithm for pressure-velocity coupling. A second-order upwind discretization method, for the turbulence equations. The standard method was used for pressure and the quick method for momentum. The convergence criteria were set to 10^{-4}. The quality of the convergence was checked by monitoring the residuals and ensuring that they were below the specified limit. Additionally, the torque value variation with the solving iterations was plotted to provide another means of checking convergence. Air density is set at 1.225 kg/m^3, and viscosity is established at 1.789×10^{-5} kg/ (m.s). The numerical analysis encompasses a range of tip speed ratios ranging from 1 to 8.6.

Table 5. Solver setup and numerical parameters

Category	Parameter	Specification / Value
Solver	Solver type	Pressure-based
	Velocity formulation	Absolute
	Pressure–velocity coupling	SIMPLE
Physical Models	Turbulence model	k–ω SST
	Simulation approach	Single Moving Reference Frame (SRF)
Boundary Conditions	Inlet	Velocity inlet (10 m/s)
	Outlet	Pressure outlet (ambient pressure)
	Blade surface	No-slip wall
	Outer domain surface	Slip wall
	Lateral boundaries	Periodic (120°)
Numerical Schemes	Pressure discretization	Standard
	Momentum discretization	QUICK
	Turbulence discretization	Second-order upwind
Convergence Criteria	Residuals	1×10^{-4}
	Additional monitoring	Torque variation with iterations
Fluid Properties	Air density	1.225 kg/m³
	Dynamic viscosity	1.789×10^{-5} kg/(m·s)
Operating Conditions	Tip-speed ratio (λ)	1 – 8.6

2.3.3 Fluid-Structure Interaction (FSI) Simulations

In the fourth step, transient simulations are conducted, considering bidirectional communication involving forces from the fluid to the solid and displacements from the solid to the fluid, utilizing the dynamic mesh approach for two-way FSI cases. In the case of one-way FSI simulations, the pressure on the turbine's blade resulting from the aerodynamic simulation serves as loads for structural simulations. Where the feedback from solid deformation to the fluid domain is disregarded [45]. The analysis covers Young's modulus values ranging from 5e8 to 1e10 Pa. This range encompasses a variety

of materials commonly used in wind turbine blade construction, including glass fibers, wood laminates, polyester resins, and epoxies, as detailed in ref [46], These materials exhibit different mechanical properties, influencing blade deformation and structural resistance.

A summary of the Young's modulus values for these materials is presented in Table 6:

Table 6. Young's modulus values for Several materials.

Material	Young's Modulus (Pa)	Notes on Application
Glass Fibers	5e10 – 9e10	Common in composite blades, good flexibility
Wood Laminates	10e9- 20e9	Sustainable, moderate stiffness
Polyester Resins	2e9 - 4.5e9	Used in composites, good toughness
Epoxies	3e9 – 6e9	Strong adhesion, good for bonding layers

2.3.4 Fluid movement governing equations

The governing equations for the turbulent incompressible flow encountered in this study are the unsteady-state Reynolds-averaged Navier-Stokes (URANS) equations, which express the conservation of mass and momentum [47].

Continuity:

$$\frac{\partial \overline{u_i}}{\partial x_i} = 0 \quad \text{(1)}$$

Momentum:

$$\frac{\partial \overline{u_i}}{\partial t} + \overline{u_j}\frac{\partial \overline{u_i}}{\partial x_j} = -\frac{\partial \overline{p}}{\partial x_i} + \nu\frac{\partial^2 \overline{u_i}}{\partial x_j \partial x_j} - \frac{\partial \tau_{ij}}{\partial x_j} \quad \text{(2)}$$

In Equation (2), $\overline{p}$ represents mean pressure, ν stands for the fluid kinematic viscosity, and $\tau_{ij} = -\overline{u_i' u_j'}$ corresponds to the Reynolds stress term. To accurately address turbulence effects, Reynolds stresses are modelled in order to achieve closure of Equation (2). The method of modelling employed the Boussinessq hypothesis to relate the Reynolds stresses to the mean velocity gradients within the flow. In order to that the study employs the K-Omega SST turbulence model [48].

The K-Omega SST turbulence model equations

$$\frac{\partial \mathrm{k}}{\partial \mathrm{t}} + \overline{u_\iota}\frac{\partial \mathrm{k}}{\partial x_\mathrm{i}} = \frac{\partial}{\partial x_i}\left[(\nu + \sigma_k \nu_t)\frac{\partial \mathrm{k}}{\partial x_\mathrm{i}}\right] + \mathrm{P}_k - \mathrm{c}_\mu \omega k \quad (3)$$

$$\frac{\partial \omega}{\partial \mathrm{t}} + \overline{u_\iota}\frac{\partial \omega}{\partial x_\mathrm{i}} = \frac{\partial}{\partial x_i}\left[(\nu + \sigma_\omega \nu_t)\frac{\partial \omega}{\partial x_\mathrm{i}}\right] + \gamma\frac{\omega}{k}\mathrm{P}_k - \beta\omega^2 + (1-\mathrm{F}_1)\frac{2\sigma_\omega}{\omega}\frac{\partial \mathrm{k}}{\partial x_\mathrm{i}}\frac{\partial \omega}{\partial x_\mathrm{i}} \quad (4)$$

Where $\mathrm{F}_1$is the blending function, and σ_ω, σ_k, β, γ are the coefficients of the SST model.

2.3.5 Dimensionless governing equations

To generalize the analysis and reduce the number of controlling parameters, the governing equations are non-dimensionalized using the following reference quantities [49]:

- Characteristic length: L
- Reference velocity: U_∞
- Reference time: $\mathrm{L}/\mathrm{U}_\infty$
- Reference pressure: $\rho\mathrm{U}^2{}_\infty$

The dimensionless variables are defined as:

$$x_i^* = \frac{x_i}{L},\ u_i^* = \frac{\overline{u_\iota}}{\mathrm{U}\infty},\ t^* = \frac{t\mathrm{U}\infty}{L},\ p^* = \frac{\overline{p}}{\rho\mathrm{U}_\infty^2}$$

Dimensionless Continuity Equation:

$$\frac{\partial u_i^*}{\partial x_i^*} = 0 \quad (5)$$

Dimensionless Momentum Equation:

$$\frac{\partial u_i^*}{\partial t^*} + u_j^*\frac{\partial u_i^*}{\partial x_j^*} = -\frac{\partial p^*}{\partial x_i^*} + \frac{1}{Re}\frac{\partial^2 u_i^*}{\partial x_j^* \partial x_j^*} - \frac{\partial \tau_{ij}^*}{\partial x_j^*} \quad (6)$$

The governing equations can be written in three dimensions as follows [50]

Continuity Equation:

$$\frac{\partial u^*}{\partial x^*} + \frac{\partial v^*}{\partial y^*} + \frac{\partial w^*}{\partial z^*} \quad (7)$$

X-Momentum

$$\frac{\partial u^*}{\partial t^*} + u^* \frac{\partial u^*}{\partial x^*} + v^* \frac{\partial u^*}{\partial y^*} + w^* \frac{\partial u^*}{\partial z^*} = -\frac{\partial p^*}{\partial x^*} + \frac{1}{Re}\left(\frac{\partial^2 u^*}{\partial x^{*2}} + \frac{\partial^2 u^*}{\partial y^{*2}} + \frac{\partial^2 u^*}{\partial z^{*2}}\right) - \left(\frac{\partial \tau_{xx}^*}{\partial x^*} + \frac{\partial \tau_{xy}^*}{\partial y^*} + \frac{\partial \tau_{xz}^*}{\partial z^*}\right)$$

Y-Momentum

$$\frac{\partial v^*}{\partial t^*} + u^* \frac{\partial v^*}{\partial x^*} + v^* \frac{\partial v^*}{\partial y^*} + w^* \frac{\partial v^*}{\partial z^*} = -\frac{\partial p^*}{\partial y^*} + \frac{1}{Re}\left(\frac{\partial^2 v^*}{\partial x^{*2}} + \frac{\partial^2 v^*}{\partial y^{*2}} + \frac{\partial^2 v^*}{\partial z^{*2}}\right) - \left(\frac{\partial \tau_{yx}^*}{\partial x^*} + \frac{\partial \tau_{yy}^*}{\partial y^*} + \frac{\partial \tau_{yz}^*}{\partial z^*}\right)$$

Z-Momentum

$$\frac{\partial w^*}{\partial t^*} + u^* \frac{\partial w^*}{\partial x^*} + v^* \frac{\partial w^*}{\partial y^*} + w^* \frac{\partial w^*}{\partial z^*} = -\frac{\partial p^*}{\partial z^*} + \frac{1}{Re}\left(\frac{\partial^2 w^*}{\partial x^{*2}} + \frac{\partial^2 w^*}{\partial y^{*2}} + \frac{\partial^2 w^*}{\partial z^{*2}}\right) - \left(\frac{\partial \tau_{zx}^*}{\partial x^*} + \frac{\partial \tau_{zy}^*}{\partial y^*} + \frac{\partial \tau_{zz}^*}{\partial z^*}\right)$$

2.3.6 Solid Displacement governing equation

Considering a solid body **Σ** surrounded by a boundary **Ω**. In general, volume forces are applied on **Σ** while surface forces and/or displacements are imposed on **Ω**. **u** denote the displacement vector defined on **Σ**, which results from the forces and displacements imposed on **Ω,** from **u**, the deformation tensor $\boldsymbol{\varepsilon}_t$ can be calculated as the symmetric part of the gradient of **u:**

$$\varepsilon_t = \frac{1}{2}\left(\nabla u + (\nabla u)^t\right) \quad \text{(8)}$$

In the present context of linear isothermal and isotropic elasticity, the constitutive equation of the stresses **σ** is given by:

$$\sigma = \frac{YM}{1+\nu}\left(\frac{\nu}{1-2\nu}\,\mathrm{tr}(\varepsilon_t) I + \varepsilon_t\right) \quad \text{(9)}$$

where **I** is the unit tensor. This equation involves two physical parameters: The Young's modulus **YM** and the Poisson's ratio **ν.**

When introducing this expression for the stresses **σ** into the momentum equation, and after substituting $\boldsymbol{\varepsilon}_t$ by its definition, a second-order elliptic equation is eventually obtained for the displacement **u**. After substitution, the momentum equation [51] can be written as:

$$\rho_s a = \frac{YM}{1+\nu}\,\nabla.\left(\frac{\nu}{1-2\nu}\mathrm{tr}(\nabla u)\, I + \frac{1}{2}\left(\nabla u + (\nabla u)^t\right)\right) \quad \text{(10)}$$

where ρ_s is the density of the solid and a is the acceleration.

2.3.7 Utilized relations

Power coefficient (Cp): The Coefficient of Power characterizes the efficiency of the turbine, representing the ratio of mechanical power Pm (derived from the product of mechanical torque Tm and rotational speed ω) to wind power Pw [52] .

$$Cp = \frac{Pm}{Pw} = \frac{T_m * \omega}{1/2\ Ar\ \rho\ V^3} \quad (11)$$

Thrust Coefficient (Ct): Presents the ratio of the axial thrust force (T) exerted by the wind on the rotor to the dynamic pressure of the wind over the rotor swept area [52].

$$Ct = \frac{T}{1/2\ Ar\ \rho\ V^2} \quad (12)$$

Tip speed Ratio (TSR): is the ratio between the speed of the tip of the blade to the speed of the wind [52].

$$\mathrm{TSR} = \frac{\omega * R}{V} \quad (13)$$

Young's modulus: Young's modulus quantifies the stiffness of an elastic material by representing the ratio between tensile or compressive stress (σ) and strain (ε) [53].

$$\mathrm{YM} = \frac{\sigma}{\varepsilon} = \frac{\mathrm{F/a}}{\Delta \mathrm{L}/\mathrm{L_0}} = \frac{\mathrm{F\ L_0}}{\mathrm{A}\ \Delta \mathrm{L}} \quad (14)$$

in Relations (5), (6) and (7), Ar is the rotor area, ρ is the air density, and V is the wind speed and R is the rotor radius and ω is rotational speed, F is the force exerted on an object under tension, L_0 is the original length of the object. ΔL is the amount by which the length of the object changes, a is the cross-sectional area.

2.3.8 Post-processing

The obtained results are post-processed, focusing on evaluating the power coefficient (Cp), thrust coefficient (Ct), airflow patterns and analysing the blade structure responses. The numerical methodology main steps are presented in Figure 13.

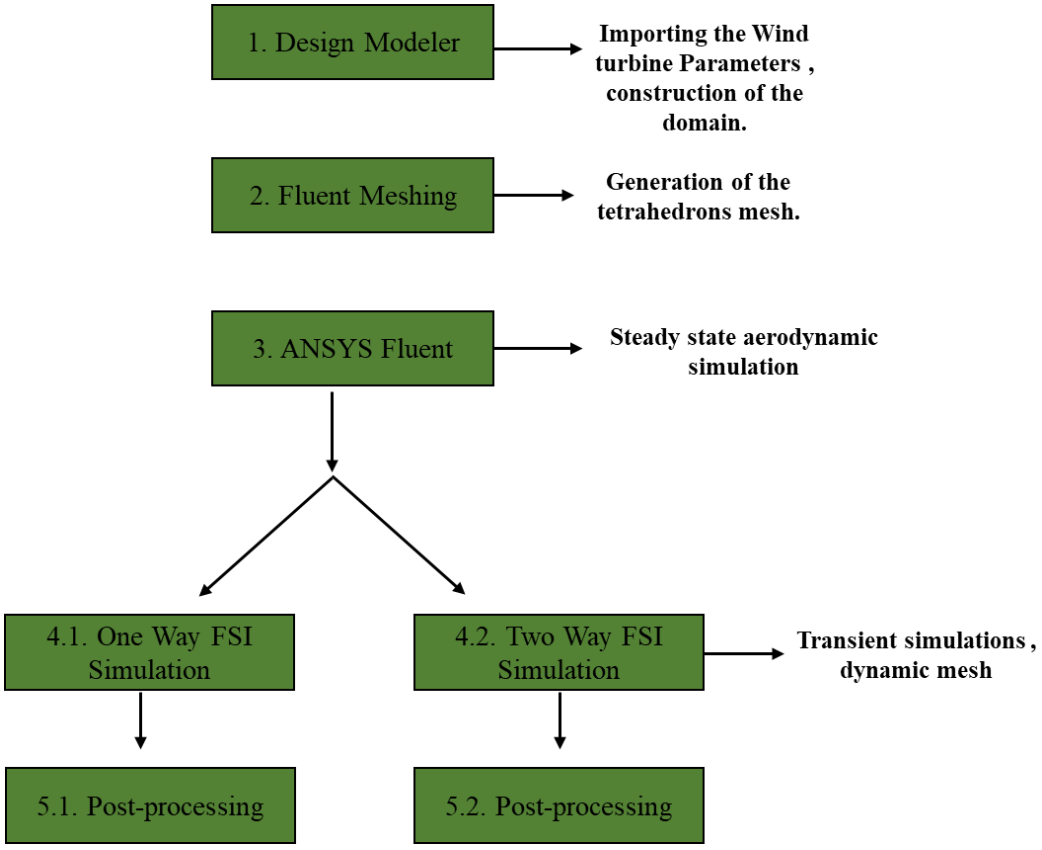

Figure 13: Numerical Methodology chart.

2.4 Results and discussion

2.4.1 Mesh analysis and Validation

A mesh sensitivity analysis was conducted to verify the suitability of the mesh for the simulations. The results, depicted in Figure 14, indicated that the optimal number of mesh cells for the current study was 916224 cells. This value was utilized to generate the final mesh for the simulations. Additionally, this figure presented a comparison between the numerical findings of this study and experimental data (EXP) and numerical results (CFD) from reference [44] to validate the results. the comparison taken in account the power and thrust coefficients and revealed an acceptable agreement between the datasets.

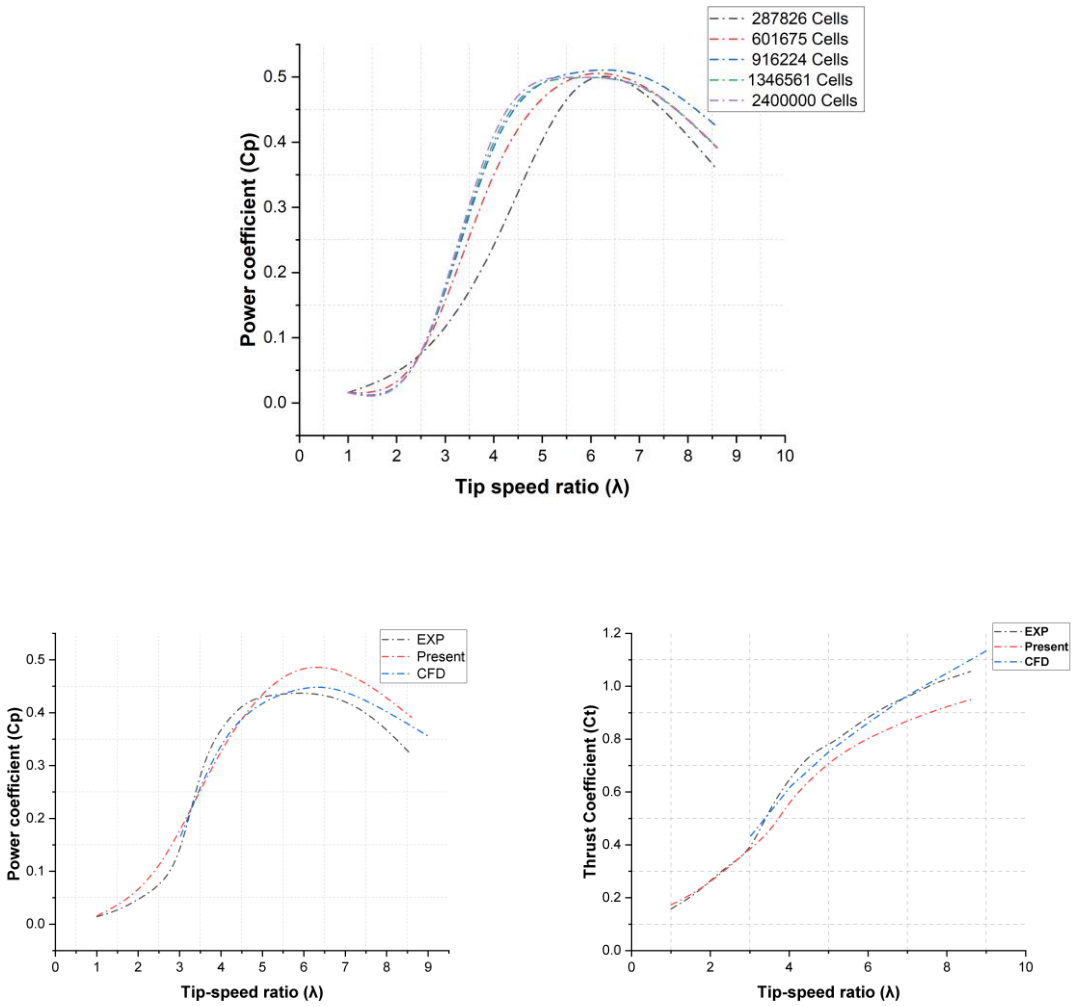

Figure 14: Mesh sensitivity analysis and a comparison between the numerical findings of this study and experimental data (EXP) and numerical results (CFD) from reference [44].

2.4.2 Aerodynamic analysis

Figure 15 and Figure 16 provide visual representations of absolute pressure and velocity magnitude contours, offering an analysis of the aerodynamic characteristics of a horizontal axis wind turbine. These figures exhibit contours at radial positions of r=30%R, r=60%R, and r=80%R (with R denoting the wind turbine radius), showcasing 12 images with varying tip-speed ratios (TSR = 2 and TSR = 6.1) at a wind speed of 10 m/s. Firstly, regarding velocity magnitude, a high velocity gradient is shown in the case of the tip speed ratio of 2 at the three radial positions (30%, 60%, and 80%R), compared to the case of maximum aerodynamic coefficient (tip speed ratio of 6.1). This aligns closely with pressure gradient values, where the highest values occur in the minimum tip speed ratio case. The figures also present relative wind speed vectors, revealing a noteworthy finding of predicted flow

separation near the blade's trailing edge at TSR = 2. The flow separation region shortens when going from the center of the blade to the tip region. However, for the highest tip-speed ratio case, the airflow remains attached to the blade in all radial positions. Overall, the comparison between TSR = 2 and TSR = 6.1 demonstrates that aerodynamic performance is highly sensitive to operating conditions. The low TSR case is dominated by high pressure gradients, early separation, resulting in reduced efficiency. Conversely, the optimal TSR maintains attached flow, balanced pressure distribution, and stable velocity gradients, leading to maximum aerodynamic coefficients.

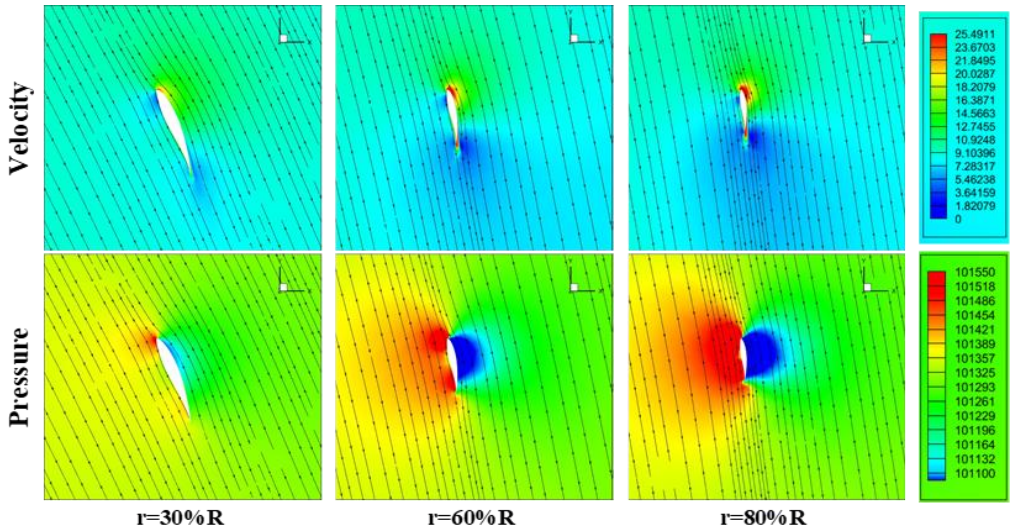

Figure 15: Velocity and Pressure Contours (TSR = 6.1)

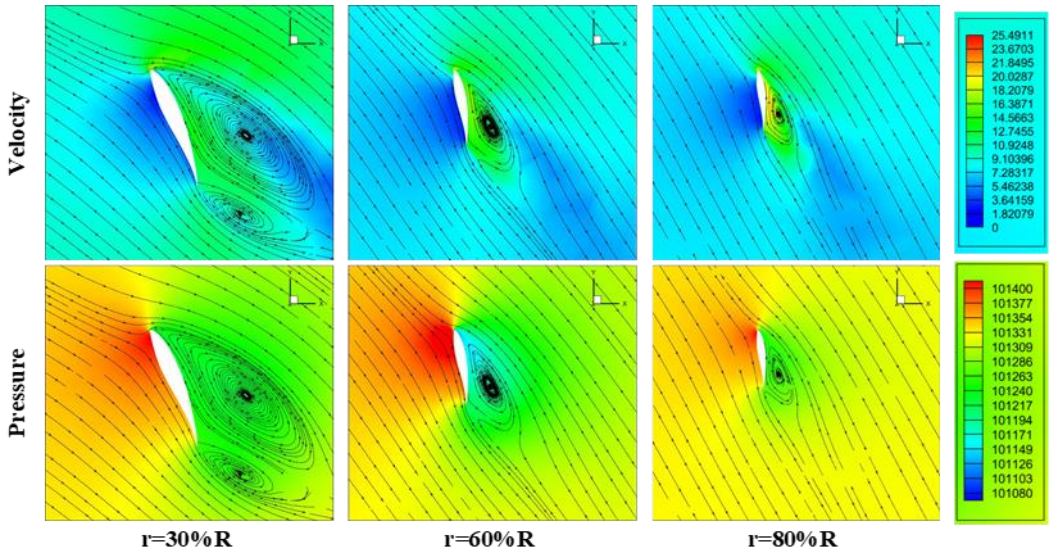

Figure 16: Velocity and Pressure Contours (TSR = 2).

2.4.3 Structural analysis

The Blade Deformation Contours presented in Figure 17 and the Blade Deformation curves as a function of radial position presented in Figure 18 depict the deformation patterns of the wind turbine blade at several Young's modulus (YM) values, while maintaining a wind velocity of 10 m/s at the maximum tip-speed ratio (TSR) corresponding to 6.1. The contours visually represent the structural response of the blade under varying YM conditions, while the curves provide a detailed analysis of the Blade Deformation values. Notably, a clear radial deformation pattern emerges from the figures, where blade deformation values appear to increase from the centre of the blade (r=0) towards the blade's tip. Furthermore, the observed trend of decreasing blade deformation values with increasing YMs suggests an inverse relationship between this blade material parameter and aerodynamic forces. In Figure 19, a contour of the von Mises stress is presented as a material failure criterion. From these contours, a maximum value is detected at the junction point of the blade-hub of the wind turbine, which is also observed at the midpoint of the blades. The values of the von Mises stress decrease with increasing Young's modulus values, with maximum values of 7.262e6, 6.909e6, and 6.570e6 Pa for YM values of 5e8, 9e8, and 1e10 Pa, respectively. These figures show that deformation is minimal at the root (r = 0) and reaches its maximum at the tip. This aligns with cantilever beam theory, where the blade is fixed at the hub and free at the end. The increase in deformation toward the tip is driven by the relative tangential velocity. Since the tip moves faster than the root, it generates higher local lift forces, amplifying the "bend. There is a clear inverse relationship between Young’s Modulus (YM) and displacement. As YM increases, the material becomes more rigid, significantly reducing the total deflection. The maximum stress is located at the blade-hub junction. As the fixed boundary, this point must resist the cumulative bending moments of the entire blade. A notable stress peak occurs at the blade midpoint, marking the transition zone where aerodynamic loading and structural constraints overlap. The figure shows that increasing the YM from 5 10^8 Pa to 1 10^10Pa reduces peak stress from 7.262 MPa to 6.570 MPa. Higher stiffness doesn't just prevent bending; it allows the blade to redistribute internal loads more effectively. From design point Low Stiffness Leads to high deformation. While this may offer "passive load alleviation" (bending to avoid the wind), it risks aerodynamic stall, fatigue, and potential collision with the turbine tower. High Stiffness Minimizes deformation and peak stress,

ensuring the blade maintains its optimal aerodynamic shape. However, this often comes at the cost of increased weight and higher inertial loads on the turbine's drivetrain.

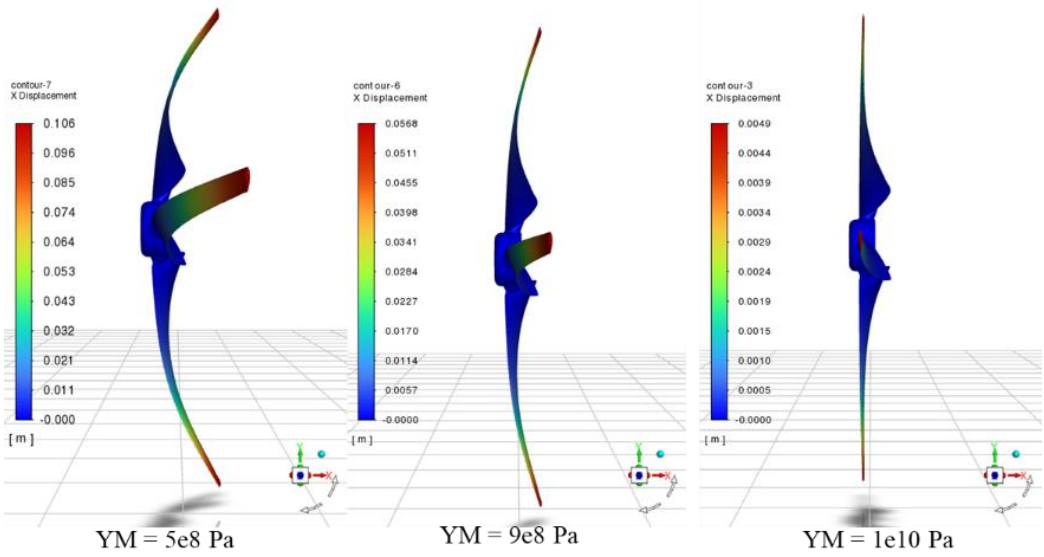

Figure 17: Blade Deformation Contours

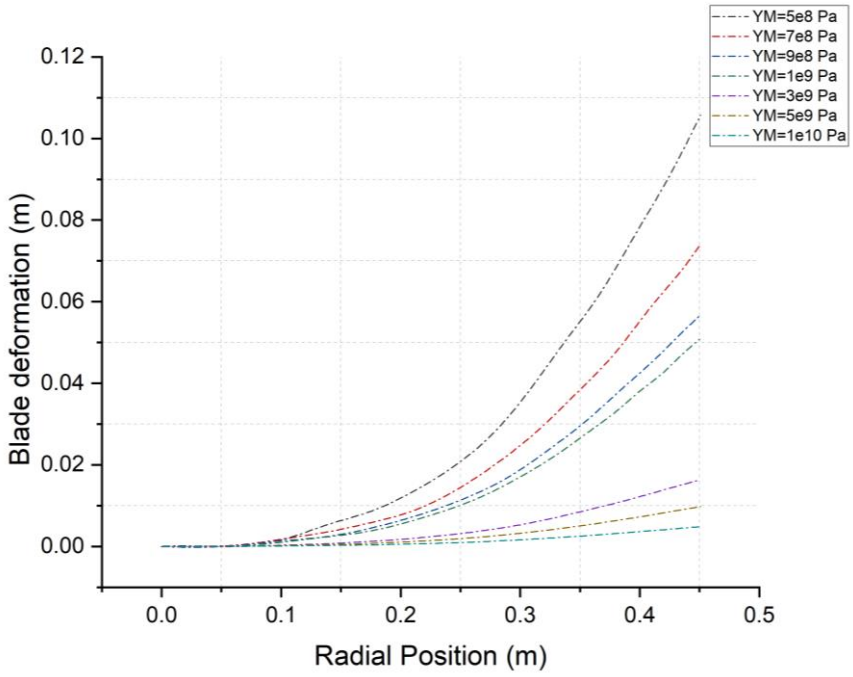

Figure 18: Blade Deformation curves.

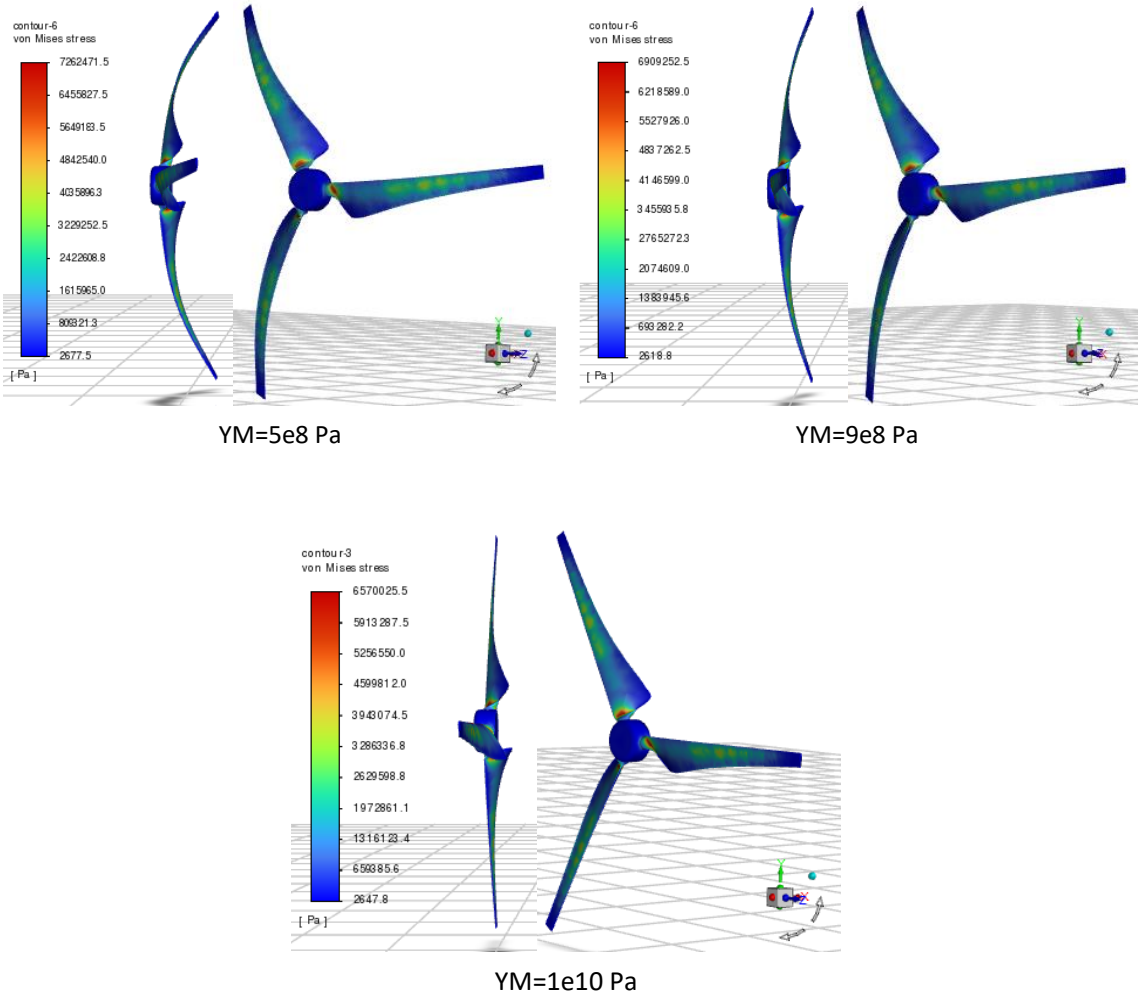

Figure 19: Von Mises stress Contours.

Figure 20 illustrates the variation in blade tip deflection (δ, in meters) as a function of time (seconds) across a range of Young's modulus values spanning from 5e8 to 1e10 Pa. The analysis comprises seven distinct curves, each corresponding to different Young's modulus value obtained at the maximum tip-speed ratio of 6.2, determined through two-way FSI simulations. The observed trend reveals oscillations in δ values over time initially, followed by stability at determined values. In the stability region, δ values decrease as Young's modulus (YM) values increase, with δ values of 0.1063, 0.0739, 0.0568, 0.0506, 0.0163, 0.0098, and 0.0049 meters for YM values of 5e8, 7e8, 9e8, 1e9, 3e9, 5e9, and 1e10 Pa, respectively. Furthermore, Figure 21 presents a comparison of blade tip deflection and blade deformation values from two FSI simulation approaches (One-way FSI and Two-way FSI simulations). The comparison reveals that the magnitude of the difference between the two approaches is dependent on the blade stiffness. At lower Young's modulus values,

the discrepancy between the two methods is relatively significant, reaching a maximum of 8.21% for YM=5e8 Pa. This behavior can be attributed to the stronger fluid–structure coupling occurring in flexible blades, where aerodynamic loads continuously modify the blade geometry, which in turn alters the surrounding flow field. Consequently, the Two-way FSI approach captures these bidirectional interactions more accurately, resulting in larger predicted deflections. As the Young's modulus increases, the blade becomes progressively stiffer, reducing its sensitivity to aerodynamic loading. This leads to a gradual reduction in the difference between the two FSI approaches. For example, the discrepancy decreases from 5.67% at 7e8 Pa to 0.36% at 3e9 Pa, and eventually becomes nearly negligible for the highest stiffness cases. At YM=1e10 Pa, the difference slightly reverses (−0.176%), indicating that both approaches converge toward nearly identical predictions.

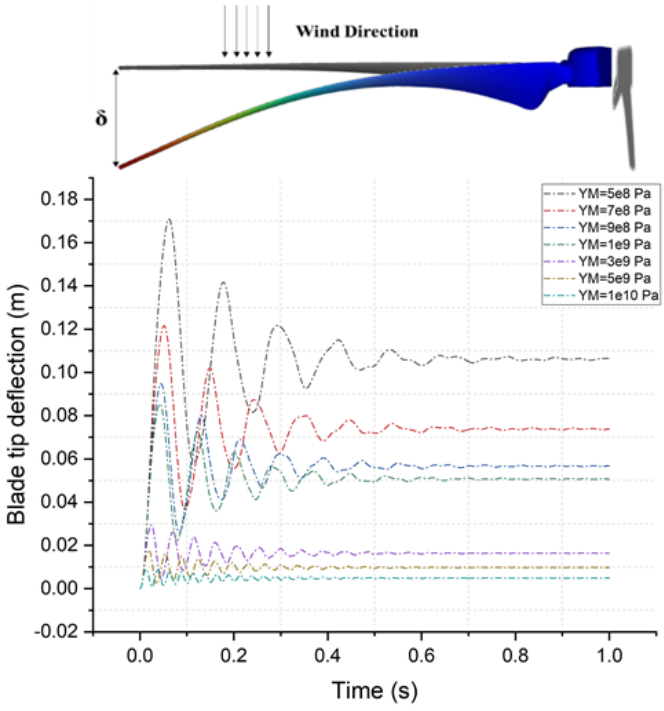

Figure 20: Blade tip deflection (δ, in meters) as a function of time (seconds).

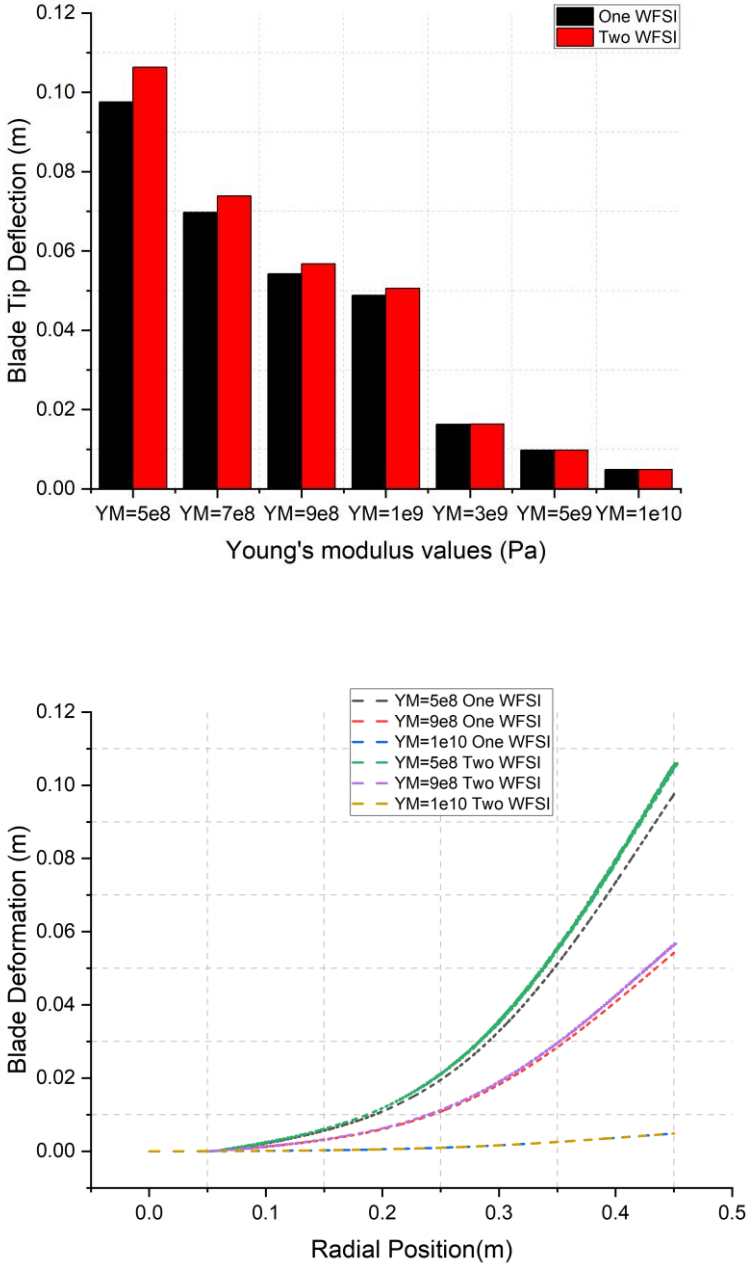

Figure 21: Comparison of blade tip deflection and blade deformation values from two FSI simulation approaches (One-way FSI and Two-way FSI simulations).

Chapter 3: Aerodynamic Analysis of Rotating Airfoils and Diffuser-Enhanced Savonius Turbines.

3.1 Introduction

This chapter Presents an Investigation of Aerodynamic Performances and Airflow Patterns over rotating Airfoils through 2D Unsteady Simulations and Provides a Performance Analysis of Savonius Wind Turbine Equipped with Three Diffusers of Different Configurations Under Variable Tip Speed Ratios.

3.2 Investigation of Aerodynamic Performances and Airflow Patterns over rotating Airfoils.

The blade section of a wind turbine is essential for converting wind into clean, renewable energy. Each blade is meticulously designed based on aerodynamic principles, with a focus on lift and drag forces. Grasping the details of aerodynamics in this setting is vital for maximizing energy capture and ensuring the efficiency of wind power systems. [54, 55]. In the literature, Numerous studies [56-64] have scrutinized the aerodynamic behaviors of NACA airfoils. These analyses encompass a variety of blade section forms, including NACA0012, NACA4412, NACA2412, NACA0009, NACA4415, NACA0015, and NACA63415. Employing a range of methodologies, from experimental to numerical approaches. The outcomes of these studies aim to identify optimal points encompassing blade section form, lift (CL) and drag (CD) coefficients, Pressure coefficient, Reynolds number from low to high, and angle of attack. The studies [65-71] collectively investigate the aerodynamic behavior of airfoils, particularly the NACA4412, under various conditions such as dynamic ground effect, extreme ground effect. Utilizing numerical simulations, experimental methods, and computational modeling techniques, these works elucidate intricate flow characteristics, pressure distributions, lift and drag forces, and their dependencies on factors like angle of attack, Reynolds number, and ground clearance. In order to that the wavy ground effects on the aerodynamic characteristics and flow field of NACA airfoils are examined in works [72-75]. This chapter provides a comparative analysis of the aerodynamics of three airfoils named NACA-4412, NACA-23012, and NACA-63415 with a specific focus on aerodynamic performance and airflow patterns, through two-dimensional unsteady simulations using Ansys Fluent software, the

computational approach thoroughly explores the impact of rotational speeds (ranging from 2 to 16 degrees per second) and a range of Reynolds numbers from 1.25e6 to 2e6.

Table 7. Airfoil models and simulation scope

Parameter	Specification
Airfoil profiles	NACA 4412, NACA 23012, NACA 63415
Simulation type	Two-dimensional unsteady CFD
Flow regime	Incompressible
Reynolds number range	$1.25 \times 10^6 – 2.0 \times 10^6$
Rotational speed range	2 – 16 deg/s

3.2.1 Numerical Methodology

The numerical methodology employed in this study consists of four main steps. Firstly, the domain is created using the Design Modeler tool. in the second step, a computational mesh is generated. The third step involves configuring the solver using ANSYS Fluent. Finally, the results are subjected to post-processing.

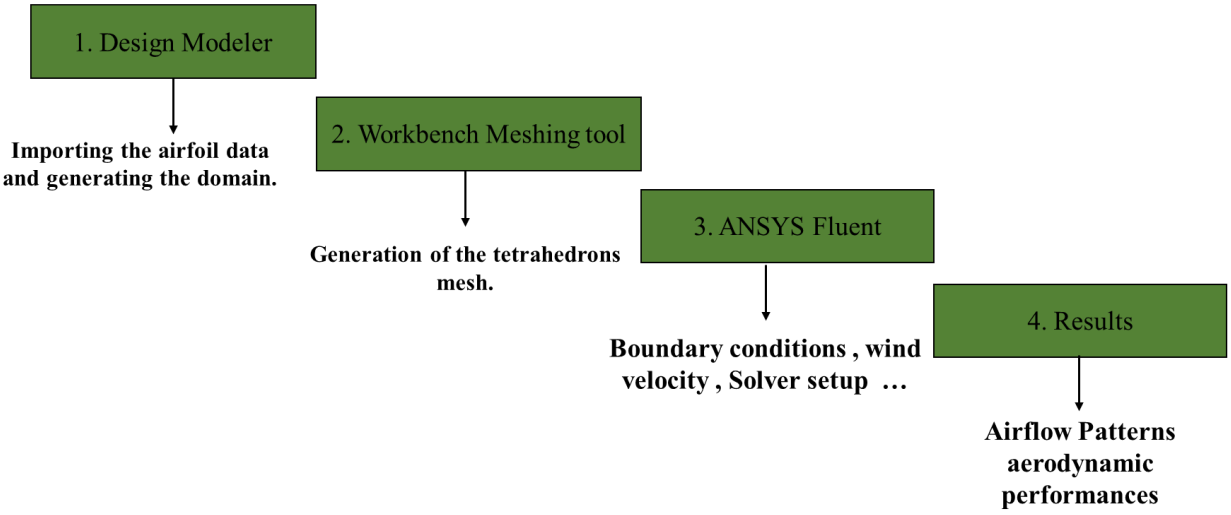

Figure 22: Numerical methodology steps.

3.2.2 Computational Domain and Calculation Mesh

The constructed domain is partitioned into an inner circular shape (with a diameter five times that of the chord length) for accommodating variations in the angle of attack. Additionally, there is an outer domain featuring inlet and outlet boundaries. Within this entire domain, a structured mesh is generated, as depicted in Figure 23.

Table 8. Computational domain configuration and Mesh characteristics

Parameter	Specification
Domain type	Two-dimensional
Inner domain shape	Circular
Inner domain diameter	5c (c: airfoil chord length)
Inner domain function	Angle of attack variation
Outer domain	Rectangular flow domain
Boundary types	Velocity inlet, pressure outlet
Mesh type	Structured
Refinement	Near airfoil surface

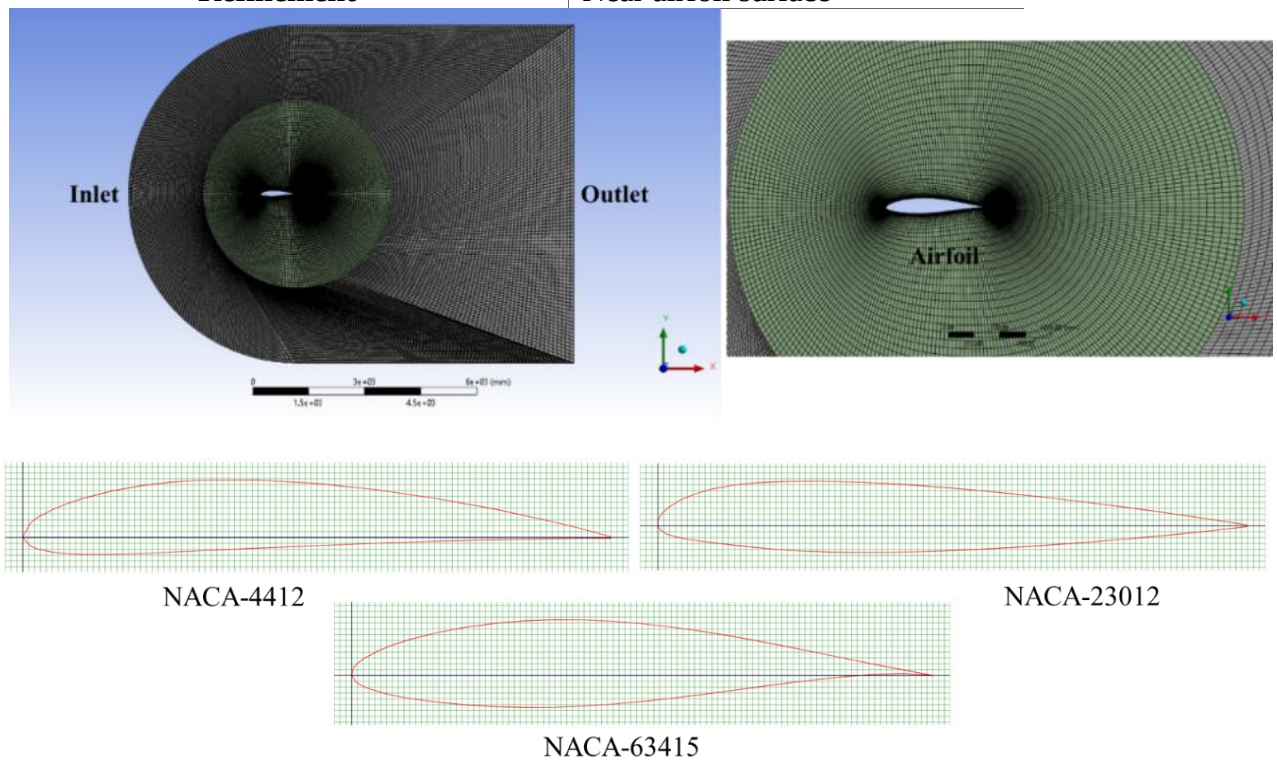

Figure 23: Computational domain.

3.2.3 Utilized relations

The lift force and the drag force are given by:

$F_L=1/2\ \rho\ C_L\ A_L\ V^2$…… (1)

$F_D=1/2\ \rho\ C_D\ A_D\ V^2$…… (2)

Here, ρ is the density of air, A_L is the projected wing area, A_D is the rotor blade's cross-sectional area and V is the velocity of the oncoming air.

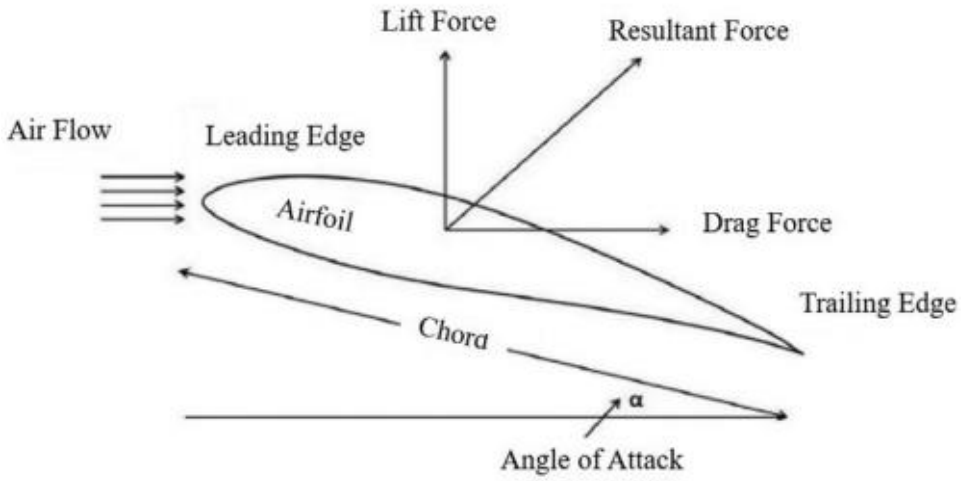

Figure 24: Aerodynamic Forces Applied on Airfoil

3.2.4 Results and Discussion

A mesh sensitivity analysis (considering lift coefficient (CL)) was conducted to verify the suitability of the mesh for the simulations. The results, depicted in Table 9, indicated that the optimal number of mesh cells for the current study was 31030 cells. This value was utilized to generate the final mesh for the simulations. An analysis of time step variation including three values (DT=0.002, DT=0.02, and DT=0.2s) revealed the use of DT=0.02s for the current simulations (see Table 10). Additionally, the Figure 25 presents a comparison between the numerical findings of this study and experimental data [76] and numerical results [77] to validate the numerical approach used in the present study . the comparison revealed an acceptable agreement between the datasets.

Table 9. Mech cells variation analysis

Time (s)	51569 Cells	31030 Cells	17648 Cells	Err %	Err %2
1.000	0.582	0.579	0.578	0.43%	0.13%
3.000	0.960	0.957	0.957	0.32%	-0.06%
6.000	1.447	1.447	1.440	0.02%	0.46%
9.000	1.674	1.690	1.652	-0.92%	2.25%
11.500	1.444	1.479	1.414	-2.42%	4.38%

Table 10. Time step variation analysis

Time (s)	DT = 0.002	DT = 0.02	DT = 0.2	Err %	Err %2
1.000	0.582	0.579	0.582	0.499%	-0.567%
3.000	0.960	0.957	0.958	0.384%	-0.138%
6.000	1.449	1.447	1.439	0.140%	0.562%

9.000	1.681	1.690	1.631	-0.505%	3.492%
11.000	1.528	1.479	1.460	3.208%	1.300%

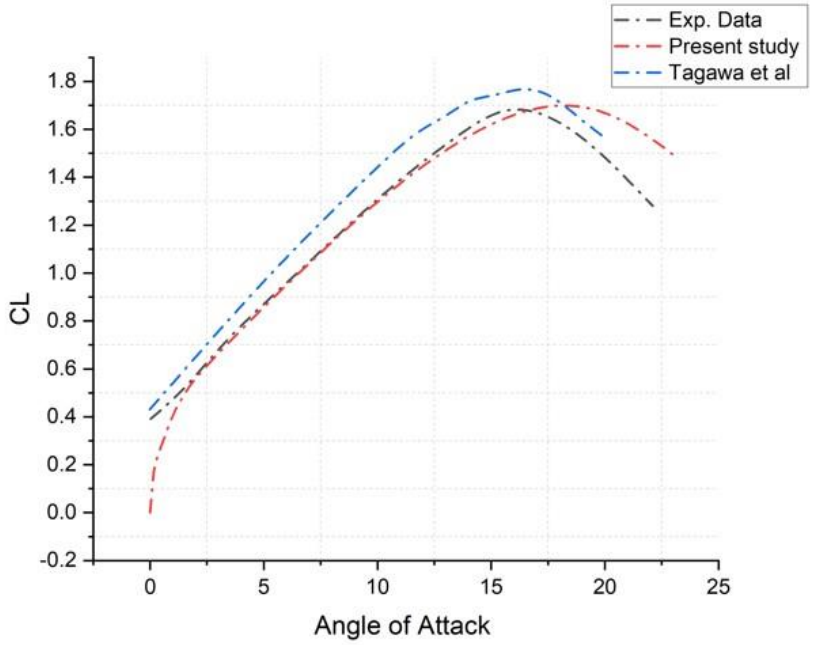

Figure 25: Numerical approach Validation.

Figure 26 illustrate graphs of the lift coefficient as a function of the angle of attack within the specified range of [0 to 23 degrees] at a Reynolds number of 2e6. The analysis focuses on the NACA-4412 airfoil, incorporating a range of rotational speeds (from 2 to 16 degrees per second). From these figures, it is evident that there is a small variation in lift coefficient values concerning the change in rotational speed, allowing for the selection of 8 degrees per second as the accepted rotational speed for the remaining studied cases.

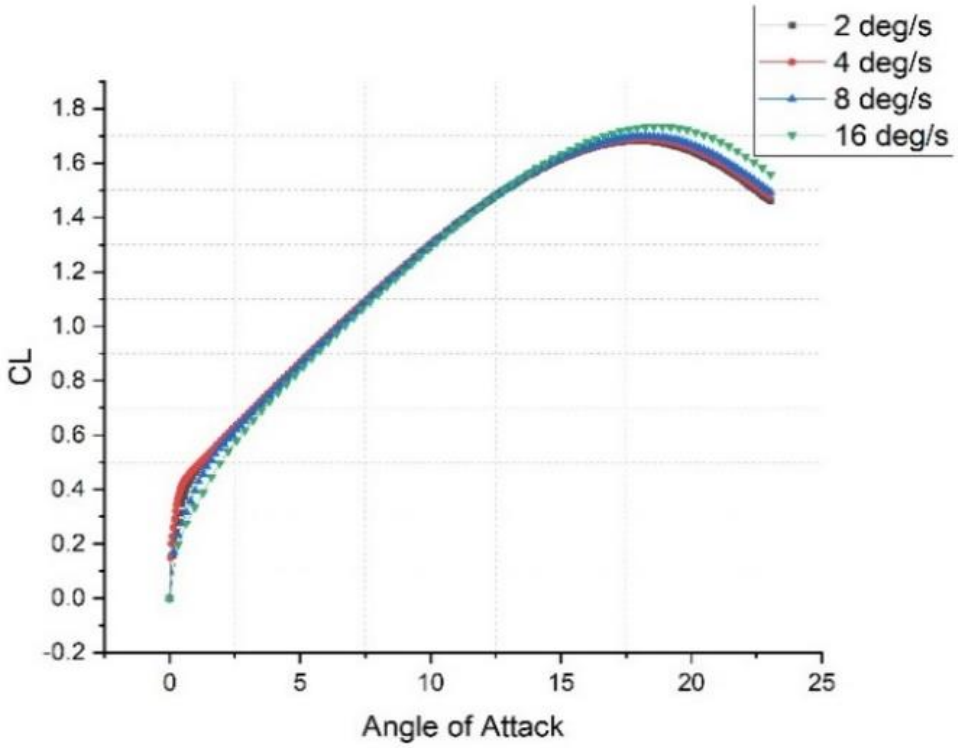

Figure 26: Lift coefficient in function of angle of attack.

Figures 27 and 28 illustrate graphs of drag and lift coefficients as functions of time for the specified range of [0 to 3s] and several Reynolds numbers (1.25e6, 1.5e6, 1.75e6, and 2e6).within the utilized rotational speed of 8 degrees per second, the analysis encompasses a range of angles of attack (from 0 to 23 degrees).in order to that the analysis considered three airfoils named NACA-4412, NACA-23012, and NACA-63415, from these figures, it is clear that the lift coefficient values exhibit an increasing variation to a maximum value after that a decreasing trend can be noticeable , the maximum values are 1.67 at 2.28 (s) , 1.45 at 2.22 (s) and 1.33 at 1.9 (s) , which correspond to 18.24 , 17.76 and 15.2 degrees for the airfoil NACA-4412, NACA-23012, and NACA-63415 , respectively. In order to that the drag coefficient values exhibit an increasing variation over time with high values in the case of NACA-63415.

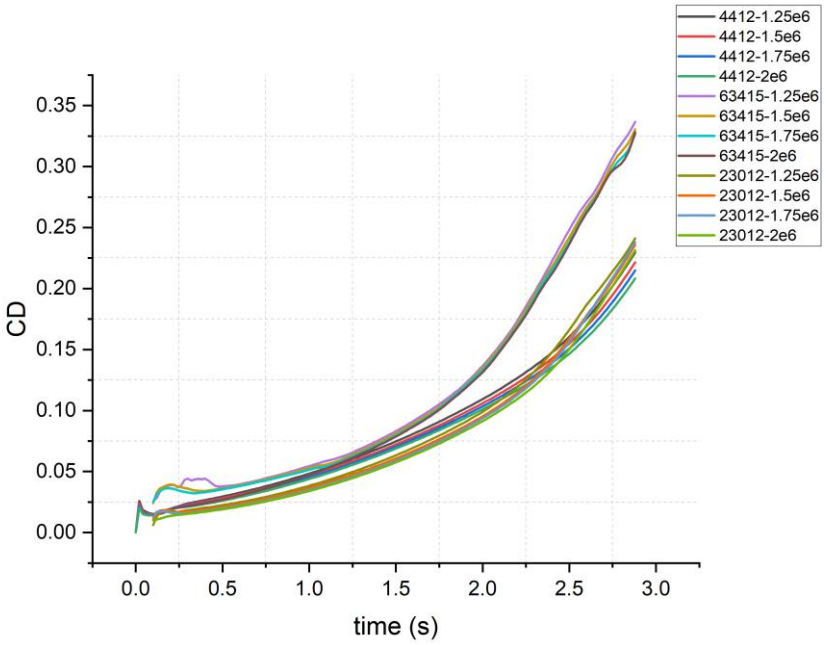

Figure 27: Drag coefficient in function of time.

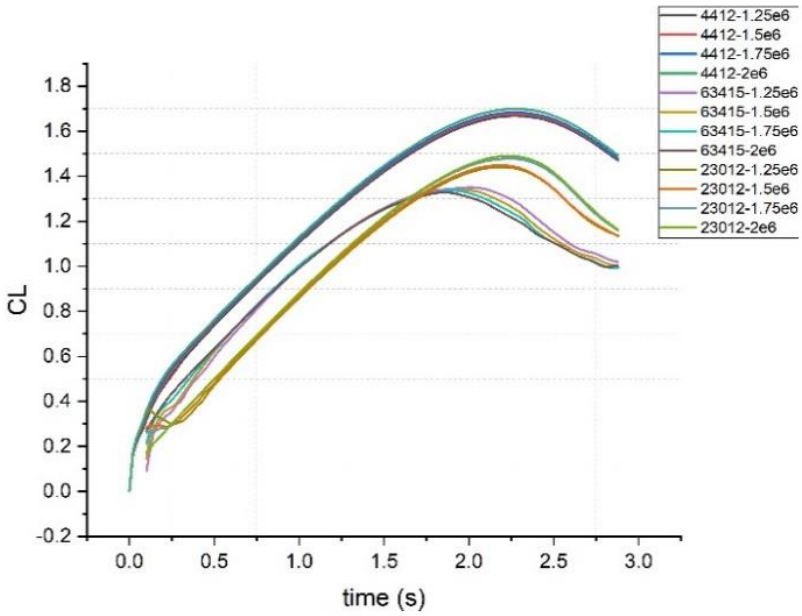

Figure 28: Lift coefficient in function of time.

Figures 29 and 30 present visualizations of velocity magnitude and velocity vectors, examining the aerodynamic characteristics of three airfoils named NACA-4412, NACA-23012, and NACA-63415. Within these figures, twelve images are displayed, illustrating different angles of attack (17.28 and 23.04 degrees) at a Reynolds number of 2E6. A noteworthy observation is the presence of a region with minimum values near the trailing edge of the airfoils. This region becomes more pronounced with an increase in the angle of

attack, aligning consistently with the flow separation region identified in the velocity vectors, with a larger separation region observed in the case of NACA 63415.

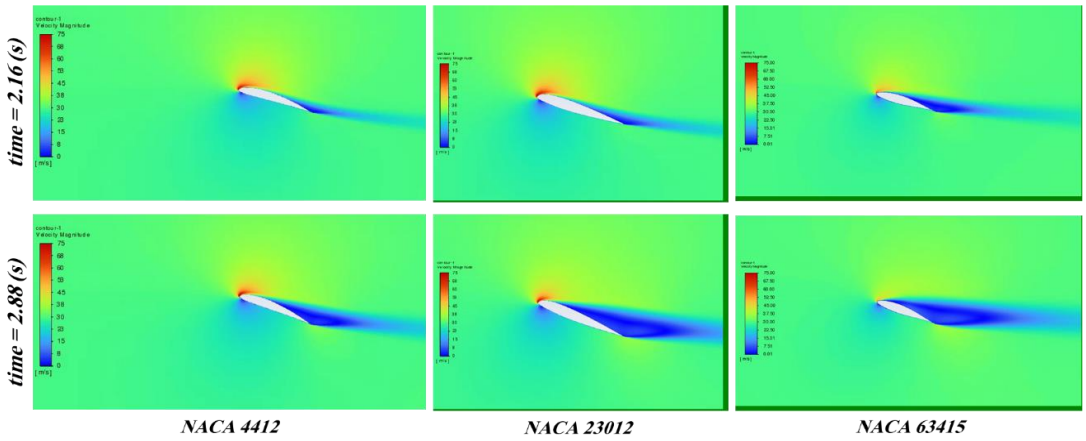

Figure 29: Velocity Magnitude.

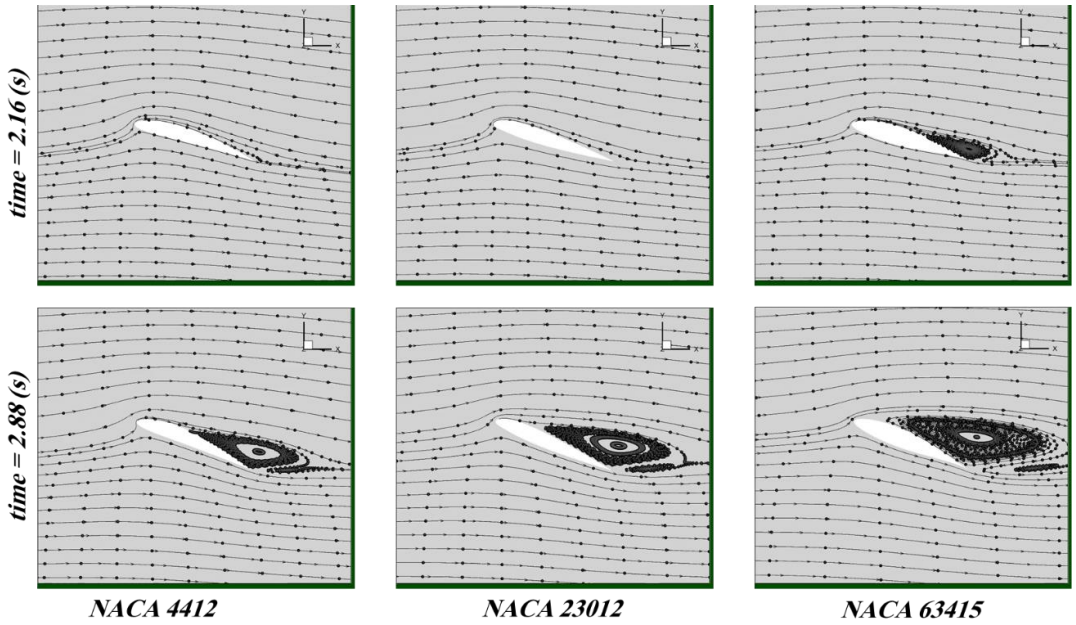

Figure 30: Velocity Vectors.

3.3 Performance Analysis of Savonius Wind Turbine Equipped with Three Diffusers of Different Configurations.

The Savonius wind turbine, characterized by its innovative drag-based aerodynamic design, presents a compelling solution for harnessing wind energy, particularly in environments with low and variable wind speeds [78] . Its unique scoop-shaped blades generate torque through pressure differentials, enabling efficient energy conversion even under less-than-ideal conditions. This adaptability, combined with a relatively low cut-in speed and minimal maintenance requirements, positions the Savonius wind turbine as a promising technology for decentralized energy generation in urban settings and remote locations alike, contributing to sustainable energy solutions and enhancing energy accessibility [79]. Recent research has explored several augmentation and optimization techniques aimed at improving the performance of Savonius wind turbines. (Patel and Mohite) [80] This numerical study analyzed a two-blade Savonius rotor equipped with six circular geometry guide vanes designed to capture wind drafts from heavy locomotive vehicles. CFD simulations showed that the vanes create a venturi effect, accelerating wind flow onto the blades and increasing power development by up to 8%. (Shahriare, Rony et al. 2025) [81] Researchers investigated two modified blade curvature models (M1 and M2) under transient conditions. At a tip speed ratio (TSR) of 1.0, these modifications yielded performance increases in the power coefficient of 9.37% and 12.5%, respectively, compared to conventional semicircular blades. (Tanino, Yoshihara et al. 2022) [82] This investigation focused on an axisymmetric casing for turbines comprising three flow deflectors with inclination angles varied between -20° and +20°.The findings revealed that optimizing these deflector angles significantly improves the pressure gradient across the blades, leading to enhanced output performance. (Aboujaoude, Bogard et al. 2023) [83] Researchers used transient 3D CFD to optimize a truncated cone axisymmetric deflector for multi-directional wind concentration. An optimized convex spline-shaped deflector was found to provide a 20% average increase in aerodynamic performance compared to standard cones. (Tata, Bekhti et al. 2023) [84] This analysis evaluated seven distinct blade configurations, identifying that elliptical blades provide an 80% increase in power coefficient over semicircular ones. Furthermore, a twin-rotor configuration using these

elliptical blades enhanced the efficiency by 110% compared to a single conventional rotor. (Kariuki, Saoke et al. 2024) [85] This numerical investigation explored the impact of Phase Shift Angles (PSA) ranging from 45° to 90° in a two-stage rotor. A PSA of 45° provided the smoothest torque distribution and the highest torque coefficient (0.3654). (Ferrari, Federici et al. 2017) [86] researchers conducted 3D parametric analysis on rotors with aspect ratios (AR) from 0.55 to 1.66. The study validated that taller rotors (higher AR) offer improved power coefficients, with a rotor having an AR of 1.1 achieving a peak Cp of 0.202. (Sumiati, Dinata et al. 2024) [87] Inner concave surfaces were modified with tiered-height zigzag patterns to increase the effective drag surface area. Experimental tests showed a 16% improvement in Cp as the zigzag geometry concentrated airflow more effectively towards the overlap region. (Mohamed, Alqurashi et al. 2022) [88] This study investigated a three-bladed Savonius design where the returning blade featured movable parts or slits (openings) to allow wind passage. The opening blade design improved performance by 25.9% at TSR 0.7, while traditional deflectors in the same setup were found to decrease performance. (Mahizam, Chang et al. 2023) [89] A Taguchi-based optimization designed a cylindrical deflector with double wake splitters and a bottom barrier. The optimal configuration (Ls/D=0.9 and 10° barrier angle) achieved a power coefficient of 0.459, representing a 61% performance increase. (Layeghmand, Ghiasi Tabari et al. 2020) [90] Researchers implemented an airfoil-shaped deflector (NACA 0012) placed at an optimal distance of 1.2/D from the rotor. This geometry achieved a 50% increase in power coefficient and doubled the static torque by shielding the returning blade and delaying flow separation. (Afify, Saber et al. 2025) [91] This work explored adding layers of multiple miniature inner blades and straight auxiliary blades to the semicircular buckets. Results showed that inner blade layering and straight auxiliary blades enhanced the power coefficient by 11.34% and 20%, respectively. (Ramarajan and Jayavel 2021) [92] Comparative analysis of four blade geometries identified a three-fourth modified shape as the most aerodynamically efficient. This modification led to Cp increases ranging from 4% to 20% compared to conventional semicircular blades. (Ghafoorian, Mirmotahari et al. 2025) [93] This study evaluated a complex housing system called the Wind Accelerator and Guiding Rotor House (WAG-RH) featuring dual-plane straight deflectors. The straight WAG-RH configuration increased the local power coefficient by 385% and the average Cp

by 264.3% in urban rooftop settings. (Zereg, Bouzaher et al. 2024) [94] A novel model was proposed utilizing partially deformable blades that expand during rotation to create an active slot. Numerical results at TSR 1.0 showed that if deformation exceeded one-quarter of the bucket radius, the torque coefficient improved by 32%. (Sugiharto, Soeparman et al. 2016) [95] This research tested variations of 4, 8, and 16 flat guide vanes placed around the rotor at a 45° angle. The 16-vane configuration yielded 33% higher performance by shifting vortex formation away from the turbine. (Singh and Kumar 2022) [96] This work analyzed a conventional Savonius turbine inside a nozzle-diffuser duct with a 28° convergent angle. Unsteady CFD simulations demonstrated that the ducted turbine achieved a 64.65% increase in power coefficient over the non-ducted baseline. (Ang and Honra 2025) [97] This study optimized a three-blade Savonius rotor equipped with pointed deflectors. The design aimed to enhance the force differential across the blades by increasing drag on the concave sides while minimizing tip vortices. (Mirashi and Kumarappa 2016) [98] This work introduced a concept featuring an internal splitter with a blunt 11.89 mm nose radius and curved stationary guide vanes (CSGV). The dual splitter-CSGV system resulted in a 15% improvement in power coefficients by providing proper air channelization and reducing negative torque. (Debnath and Debbarma 2024) [99] Researchers simulated an elliptical bladed profile in conjunction with an upstream curtain plate. The results showed that elliptical rotor blades achieved a peak power of 10 W, outperforming the conventional rotor's 8 W. (Mohammadi, Mohammadi et al. 2018) [100] This study numerically investigated the impact of installing various nozzle configurations and modifying bucket curvature to enhance momentum exchange. Researchers tested four nozzle designs—simple, curved, simple with tail, and curved with tail—finding that a simple nozzle with an attached tail performed best by capturing more air and eliminating reverse torque. Additionally, the work introduced double-curved buckets in one, two, and three-stage configurations; results showed that the double-curved two-stage rotor achieved the highest performance, raising the maximum power coefficient from 0.13 to 0.39. (Khalil, Bassuoni et al.) [101] This research utilized 3-D numerical analysis to examine a Savonius rotor installed inside a long-flanged diffuser equipped with a plate obstacle at the entrance. The geometry featured a plate obstacle at a 25° angle, an entrance angle of 5°, and a 12° flange at the exit. The simulations revealed that the obstacle plate effectively increased drag force

on the advancing blade while shielding the returning blade, leading to a 52% increase in the torque coefficient (Ct=0.38) and a 20% increase in the power coefficient compared to an un-shrouded rotor. (Antar and Elkhoury 2019) [102] Researchers conducted a 2-D parametric optimization to size a three-wall guide plate casing, which was then validated using 3-D Delayed Detached Eddy Simulations (DDES). The optimization involved varying five geometric parameters: the curvature of the top wall (R1), the offset distance of the lower casing (R2), the jet angle of the returning blade (D1), and the jet width (D2). The study found that while optimal dimensions vary with the Tip Speed Ratio (TSR), the optimized casing consistently outperformed the caseless design, tripling the peak torque and achieving a maximum 42.5% performance improvement in 3-D simulations. (Hesami, Nikseresht et al. 2022) [103] This study investigates a "wind-lens" (a flanged diffuser combining a nozzle and diffuser) for single and twin-rotor Savonius configurations. High-fidelity numerical simulations (2D URANS) show that a twin-rotor ducted turbine in an optimal counter-rotating arrangement can improve the maximum power coefficient (Cp) by approximately 114% relative to an open turbine. The optimal position for the rotors within the wind-lens throat was found to be a vertical distance ratio (Lt/D) of 0.45, which maximizes the positive mutual interaction and Venturi effect between the blades. (Guo, Song et al. 2020) [104] Researchers proposed a passive system that uses a rear deflector impinged by incoming flow to automatically align a front deflector. Towing tank tests and 2D CFD simulations revealed that the rear deflector itself can suppress turbine performance if placed too close; however, at an optimal distance of 0.82 times the turbine diameter (S1 /D=0.82), the suppressing effect on Cp is reduced to less than 3%. The study concludes that shorter deflector lengths and farther distances from the center of rotation result in a weaker negative impact on the power coefficient. In the present chapter numerical simulations conducts to analyse the aerodynamic performance, including power and torque coefficients, of a traditionally shaped Savonius wind turbine equipped with three diffusers of different configurations.

3.3.1 Numerical methodology

The numerical methodology utilized in this study comprises four primary steps. Initially, the domain is constructed through the Design Modeler tool. Subsequently, a computational

mesh is generated. The third step involves configuring the solver using ANSYS Fluent. Lastly, the results undergo post-processing.

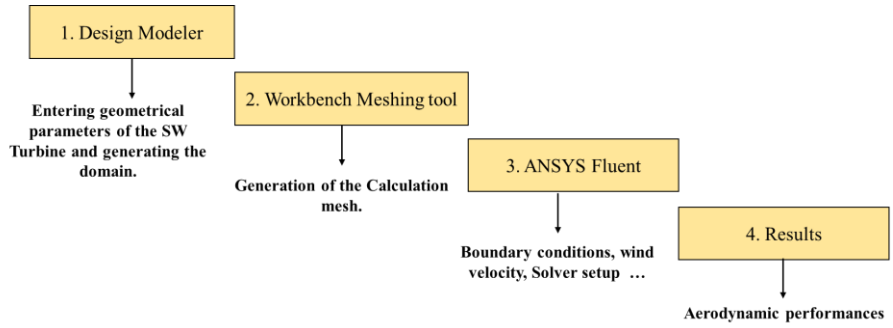

Figure 31: The numerical methodology

Figure 32 illustrates the four configurations studied: a conventional Savonius wind turbine and three modified configurations (SH1, SH2, and SH3). And the table. 11 presents the main Geometric Parameter.

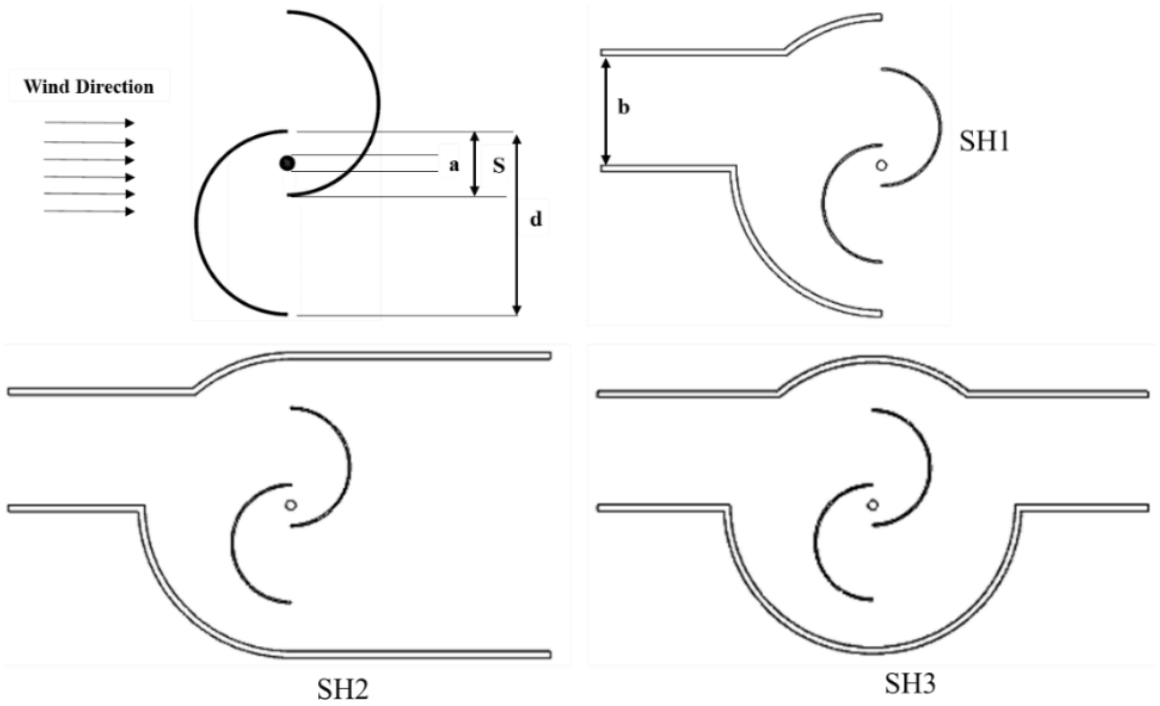

Figure 32 : The four configurations studied: a conventional Savonius wind turbine and three modified configurations (SH1, SH2, and SH3).

Table 11. Geometric Parameters

Geometric Parameter	Value
d (m)	0.302
S/d	0.219
a/d	0.050
b/d	0.563

The constructed domain is partitioned into an inner circular shape and an outer domain featuring inlet and outlet surfaces along with surrounding surfaces. Within this entire domain, a Hybrid-mesh is generated, as depicted in Figure 33.

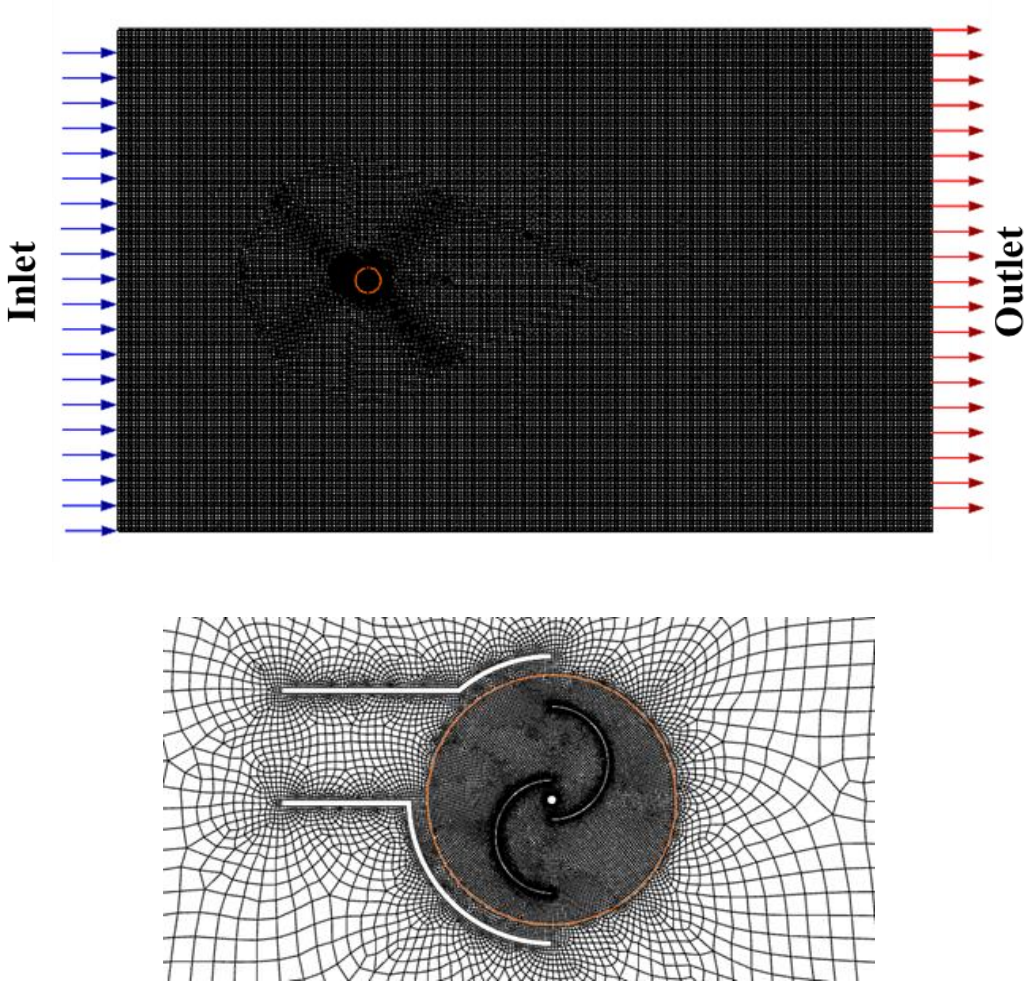

Figure 33: Computational Domain.

3.3.2 Utilized relations

Power coefficient (Cp):

$$Cp = \frac{Pm}{Pw} = \frac{T_m * \omega}{1/2\ A\ \rho\ V^3} \quad (1)$$

Tip speed Ratio (TSR):

$$\text{TSR} = \frac{\omega * R}{V} \quad (2)$$

Torque coefficient (Ct):

$$Ct = \frac{Cp}{TSR} = \frac{T_m}{1/2\ A\ \text{R}\ \rho\ V^2} \quad (3)$$

Reynolds Number (Re):

$$\text{Re} = \frac{VD}{\nu} \quad (4)$$

3.3.3 Results and Discussion

In order to validate the results obtained from the present numerical study, Figure 34 and Figure 35 presented a comparison between the present numerical findings and an experimental data from reference [105], the results indicated an accepted agreement between the datasets.

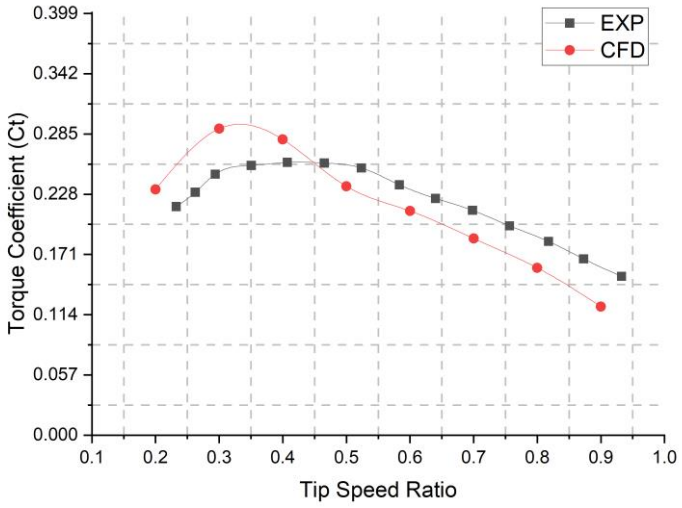

Figure 34: Torque coefficient (Ct) in function of TSR.

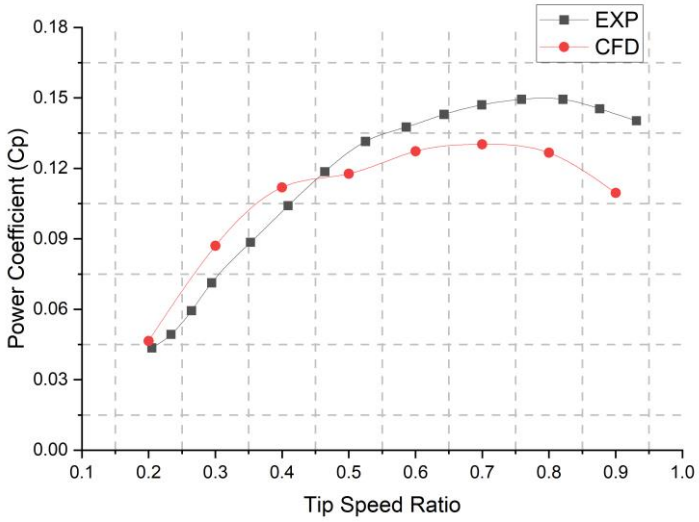

Figure 35: Power coefficient (Cp) in function of TSR.

Figure 36 and Figure 37 illustrates the variation of the aerodynamic coefficients (torque and power) over a range of tip speed ratios (TSRs) from 0.2 to 0.9 for the four configurations studied: a conventional Savonius wind turbine and three modified configurations (SH1, SH2, and SH3). The results revealed the following:

- A common trend where the aerodynamic coefficients initially increase, reaching a peak before decreasing.
- An improvement in aerodynamic performance with the addition of diffusers to the conventional turbine.
- Maximum power coefficients of 0.433, 0.423 and 0.208 for the SH1, SH2, and SH3 configurations, respectively.
- Maximum torque coefficients of 1.08, 0.921 and 0.367 for the SH1, SH2, and SH3 configurations, respectively.
- The SH2 configuration demonstrated stability in maximum power coefficients over a TSR range of 0.4 to 0.8, while the SH1 configuration peaked and then declined rapidly.

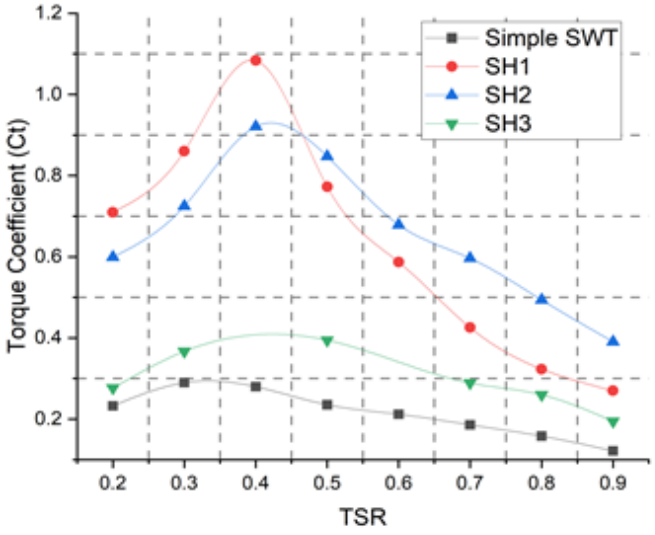

Figure 36: Torque coefficient (Ct) in function of TSR.

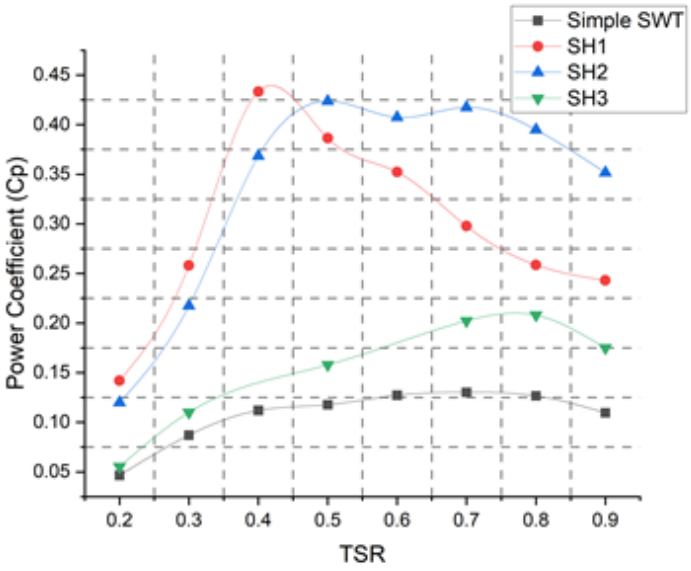

Figure 37: Power coefficient (Cp) in function of TSR.

Figures 38 and 39 present detailed visualizations of the velocity magnitude and absolute pressure contours, providing insights into the aerodynamic behaviour of the SH1 and SH2 configurations. The figures include twelve images, each corresponding to three distinct tip speed ratios (TSRs) of 0.2, 0.4, and 0.9. These visualizations help to clarify how the added configurations influence the wind flow around the turbine blades. In the SH1 and SH2 configurations, the diffusers effectively channel the wind directly toward the concave side of the wind turbine blades. This redirection leads to an increase in absolute pressure on the concave side, which enhances the driving force and results in improved torque and power generation. On the other hand, the added configurations create a shielding effect on the convex side of the turbine. By blocking the oncoming wind from directly hitting the convex surface, the diffusers accelerate the airflow around this side, causing a reduction in absolute pressure. This pressure drop on the convex side is crucial because it reduces aerodynamic drag, allowing for smoother and faster rotation of the turbine blades. As TSR increases, the visualizations reveal changes in the airflow patterns and pressure distribution across both sides of the turbine blades. At lower TSRs (0.2 and 0.4), the effect of the configurations is most pronounced, as the wind is more effectively directed toward the concave side, generating higher pressure differentials. At a higher TSR (0.9), while the overall aerodynamic performance still benefits from the diffuser configurations, the differences in

pressure and velocity magnitude are less dramatic, indicating a diminishing return on performance improvements at very high rotational speeds.

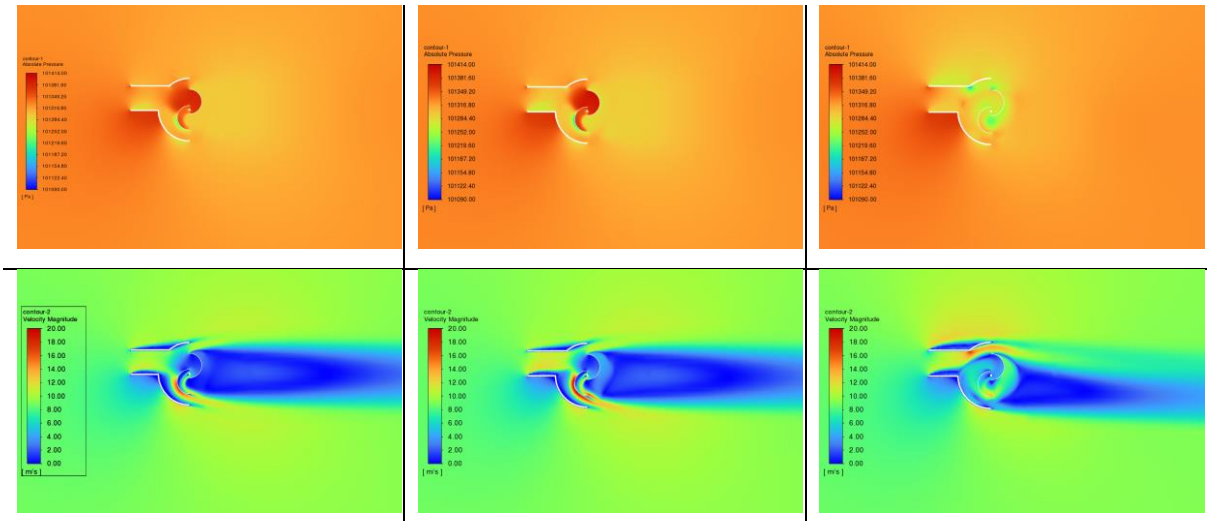

TSR=0.2	TSR=0.4	TSR=0.9

Figure 38: The velocity magnitude and absolute pressure contours of the SH1 Configuration.

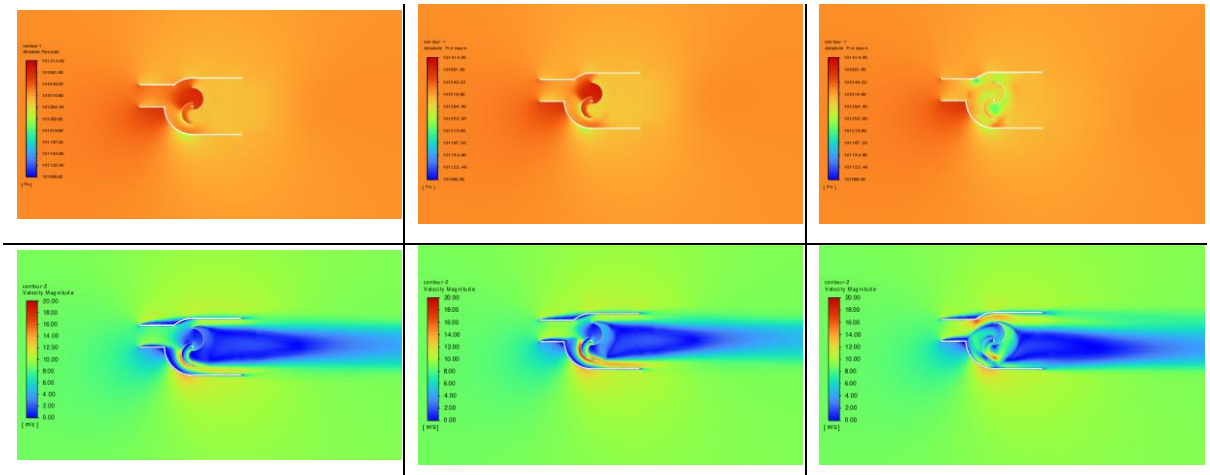

TSR=0.2	TSR=0.4	TSR=0.9

Figure 39: The velocity magnitude and absolute pressure contours of the SH2 Configuration.

Chapter 4: Multi-objective optimization of wind turbines maintenance using the Whale Optimization Algorithm.

4.1 Introduction

New and renewable energies are becoming the most preferred sources of electricity by nations due to their cleanliness, reduced costs and impacts on economic markets. Wind turbines are considered one of the best clean sources of electricity generation and their siting requires wind-rich regions [106]. Wind stochasticity influence negatively on the operation of wind systems by undergoing random loads which generates multiple and unnecessary stops and makes their maintenance complex [107].The objective of this section is to seek the appropriate minimum number of maintenance tasks to be scheduled over a period of one year to reduce and limit the occurrence of failures. To do this, the Whale Optimization Algorithm (WOA) is proposed as a new approach to optimize the availability, the maintenance cost and the total cost including the cost of electricity production losses due to the various shutdowns of wind systems. Two objective functions and 9 constraints are carefully selected to accomplish the objective in question and to reach the optimal values of different desired performances.

4.2 Whale optimization algorithm

Whale optimization algorithm (WOA) is a recently developed swarm-based meta-heuristic algorithm by [108], The algorithm simulates the bubble-net hunting maneuver technique—of humpback whales. During hunting, the whales create typical bubbles along a circle path while encircling prey. Simply, the hunting behavior could be described as follows at a depth of about 12 m, the whales create the bubble in the form of a spiral around the prey, and then rise to the surface following the bubbles. Mathematically, in the WOA hypothesis model, the current best candidate solution is the target prey. The remaining whales try to update their position to the best solution according to equation (1):

$$D = |C.X^*(t) - X(t)| \quad (1)$$

$$X(t+1) = X^*(t) - A.D \quad (2)$$

Where:

- X^* : represents the position vector of the best solution,
- X : is the position vector,
- t: represent the current iteration,

$A\ and\ C$: are coefficient vectors. A and C values are calculated as follows:

$$A = 2.a.r - a \quad (3)$$

$$C = 2.r \quad (4)$$

Where:

- a : is a control parameter and it is linearly decreased from two to zero over iterations.
- r: is a random number [0,1].

The exploitation phase of the bubble net strategy is a hybrid of two combined approaches that can be mathematically modeled as follows:

a. Shrinking Encircling Mechanism

obtained by decreasing a value according to Equation (4). Noting that a is a random value in [−a, a].

b. Spiral Updating Position

To simulate the whale's helix-shaped movement, a spiral equation is created between the position of the whale and the prey as follows:

$$X(t+1) = D'.e^{bl}.\cos(2\pi l) + X^*(t) \quad (5)$$

$$D' = |X^*(t) - X(t)| \quad (6)$$

Where:

- b: is the parameter space (fixed number).
- l: is a random number in [−1, 1].

Indeed, the whales swim at the same time along a spiral-shaped trajectory and in a constricting circle. To choose either the spiral or the shrinking circle mechanism model, a 50% probability is assumed as follows:

$$X(t+1) = \begin{cases} X^*(t) - A.D & if\ p < 0.5 \\ D^l.e^{bl}.\cos(2\pi l) + X^*(t) & otherwise \end{cases} \quad \text{..... (7)}$$

Where:

p: is a random number in a uniform distribution,

Similarly, to almost all meta-heuristic algorithms, in the bubble net method the position of the optimal model is not known, so humpback whales search for their prey randomly. Furthermore, in the exploration phase, $1 \prec A \prec -1$ is used to force the agent to move away from this location.

The exploration phase is represented mathematically in equations (7) and (8) as follows:

$$D = |C.X_{rand} - X(t)| \quad \text{..... (8)}$$

$$X(t+1) = X_{rand} - A.D \quad \text{..... (9)}$$

Figure 40, shows the flowchart of standard Whale Optimization Algorithm (WOA).

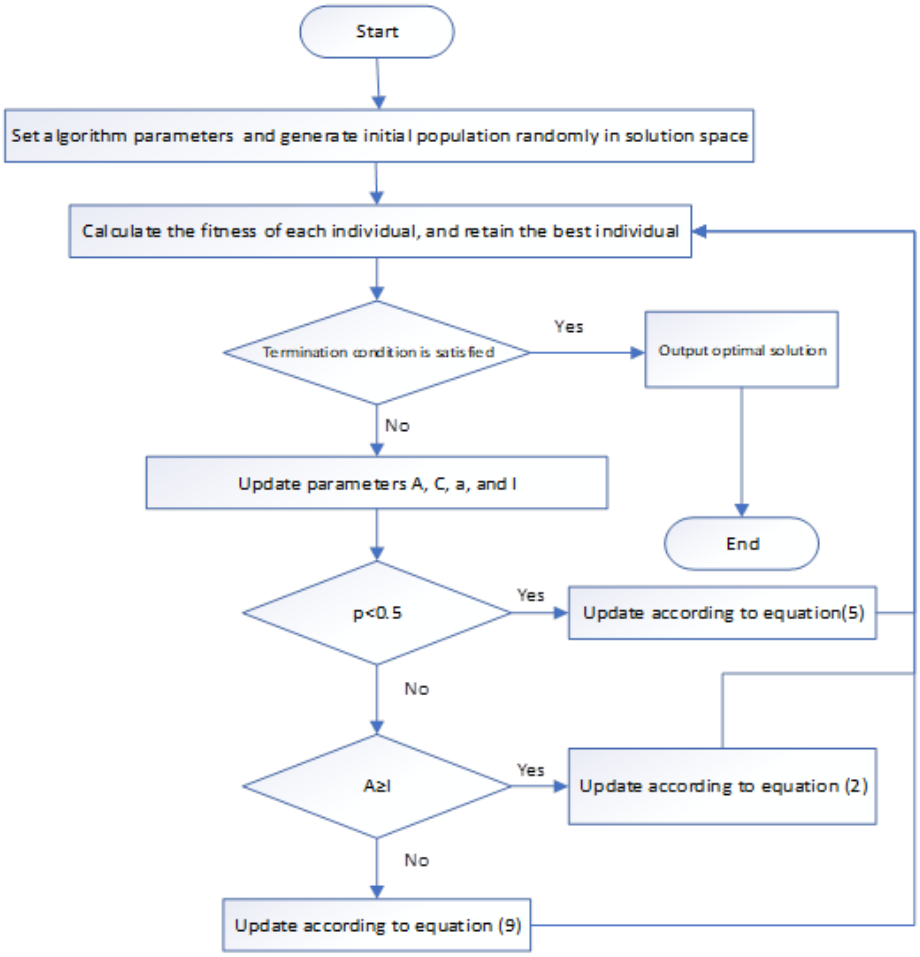

Figure 40: Flowchart of standard Whale Optimization Algorithm (WOA).

4.3 Model Approach

4.3.1 Maintenance Parameters

To determine the mathematical optimization models, several maintenance parameters responding to the problem in question are necessary such as:

- ❖ Availability A: The availability of an industrial system is given by the equation 10;

$$A = \frac{MTBF}{MTBF+MTTR} \quad (10)$$

With:

MTBF: Mean time between failures.

MTTR: Mean time to repair.

- ❖ Failure rate λ: The failure rate is inversely proportional to MTBF, it is given by:

$$\lambda = \frac{1}{MTBF} \quad (11)$$

- ❖ Repair rate: The repair rate is the inverse of the MTTR, it is expressed by:

$$\mu = \frac{1}{MTTR} \quad (12)$$

Applying equations (11) and (12) to equation (10), the expression of availability will be:

$$A = \frac{\mu}{\mu+\lambda} \quad (13)$$

Availability can be given by the following expression:

$$A = \frac{1}{1+\lambda.MTTR} \quad (14)$$

4.3.2 Total Cost Model

Total cost is the sum of costs spent on equipment maintenance plus production costs lost due to system downtime, it is expressed by:

$C_T = C_{PM} + C_{CM} + C_{pen} + C_{loss}$ ..... (15)

With:

- C_{PM}: Preventive maintenance costs.
- C_{CM}: Corrective maintenance costs.
- C_{Pen}: Cost of additional work carried out by the maintenance team.
- C_{loss}: Cost lost due to system downtime.

The total cost of i turbines can be expressed by equation (16):

$C_T = \sum_{j=1,i=1}^{J,I} \alpha_{ji} C_{CMh} + \sum_{i=1}^{I} \beta_i C_{PMa} + \sum_{i=1}^{I} n_i C_{pen} + \sum_{i=1}^{I} P_i \,.\, r_i . C_{el}$ ..... (16)

Where:

α_{ji}: is task j duration for corrective maintenance in wind turbine i [h].

If preventive maintenance is carried out without stopping the system, α_{ji} can be given by equation (9):

$\alpha_{ji} = \frac{1}{\lambda_{ji}} . \frac{[1-(1+n_{ji}\,\lambda_{ji})A_i]}{A_i}$ ..... (17)

With:

- λ_{ji}: is failure rate j in wind turbine i [1/h].
- n_{ji}: is supplementary hours for corrective maintenance task j in wind turbine i.
- A_i: Availability of wind turbine i.
- β_j: is the number of preventive maintenance tasks.
- C_{CMh} : is the hourly cost for performing corrective maintenance [€/h].
- C_{CMa} : is the average cost for performing preventive maintenance [€].
- C_{pen}: Penalty cost of additional maintenance work [€ / h].
- P_i: is the power of electricity generated by the wind turbine i [kW].
- r_{ji}: is the downtime j of wind turbine i [h].

The number of overtime hours in each repair j is given by the following equation (18):

$n_i \leq r_{ji} - \alpha_{ji}$ ..... (18)

C_{elec}: Electricity Cost [€ / kWh].

4.3.3 Objectives Functions of Optimization Model

The objective is to determine the optimal number of preventive maintenance tasks which corresponds to better availability (Amax) with minimal maintenance cost (Cmin).

Minimize equation

$$C_T = \sum_{j=1,i=1}^{J,I} \frac{1}{\lambda_{ji}} . \frac{[1-(1+n_{ji}\,\lambda_{ji})A_i]}{A_i} . C_{CMh} + \sum_{i=1}^{I} \beta_i\, C_{PMa} + \sum_{i=1}^{I} n_i\, C_{pen} + \sum_{i=1}^{I} P_i\,.\, r_i . C_{el}$$

Maximize equation

$$A_i = \frac{1}{1+\lambda_{ji}.(\alpha_{ji}.+n_{ji)}}$$

Subject to:

$[(1+\lambda_{ji}.(n_{ji}+1)].A_{ji} - 1 \le 0;\ 1 \le i \le 3;\ 1 \le j \le 3$ ..... (19)

$-r_{ji} + \alpha_{ji} + n_{ji} \le 0\ ;\qquad 1 \le i \le 3;\ 1 \le j \le 3$ ..... (20)

$n_{ji} = L_{ji} - 8;\ L_{ji} \ge 8;\qquad 1 \le i \le 3;\ 1 \le j \le 3$ ..... (21)

$2783.\lambda_{ji} - 1 = 0;\qquad 1 \le i \le 3; 1 \le j \le 3$ .....(22)

$4 \le \beta_i \le 12\ ;\qquad i \in I\ ;\ 1 \le i \le 3$ .....(23)

$n_{ji} \ge 0\ ;\qquad 1 \le i \le 3; 1 \le j \le 3$ .....(24)

$r_{min} \le r_{ji} \le r_{max}\ ;\qquad 1 \le i \le 3; 1 \le j \le 3$ .....(25)

$\lambda_{min} \le \lambda_{ji} \le \lambda_{max}\ ;\qquad 1 \le i \le 3; 1 \le j \le 3$ .....(26)

$0.9 \le A_i \le 0.98\qquad 1 \le i \le 3$ ..... (27)

4.4 Real case study and results

In this case study, it was considered the onshore wind farm Vestas V66 with three 1.65 MW wind turbines [109]. It is assumed that this wind turbine experiences up to three failures, i.e., 1 to three corrective maintenance tasks to be performed over a period of one year. The cost per hour is assumed to be the same for all corrective interventions. The maintenance team works within the limit of 8 hours per day. Exceeding this hourly limit,

we start counting overtime. Preventive maintenance tasks are supposed to be scheduled at least every three months and at most every month in the year with an average cost estimated at 65 euros for each task. All preventive maintenance tasks are supposed to be carried out without shutting down the wind system.

Table 12 shows the failure rate and downtime for each component of the wind turbine [109].

Table 12. Failure rate and downtime of each turbine component.

COMPONENT	FAILURE RATE (X10-3) (1/H)	DOWNTIME (H)
BLADES	0.617	36.9
TOWER	0.02	1
PITCH SYSTEM	0.375	11.175
MECHANICAL BRAKE	0.5	2.5
SHAFT/BEARING	0.1	2
GEARBOX	0.625	136.925
GENERATOR	0.4	101.625
HYDRAULIC SYSTEM	0.5	19.075
YAW SYSTEM	0.15	5.5
WIND MEASUREMENT	0.217	11.725
CONTROL SYSTEM	0.507	12.567
SENSORS	0.327	11
ELECTRICAL SYSTEM	0.7	33.907
OTHERS	0.433	7.2

The simulation parameters are assumed as follows: $C_{PMa} = 65$ € ; $C_{CMh} = 45$ €/h, ; $C_{el} = 0.83$ €/KWh, ; $P_i = 1.65\ MW$; $C_{pen} = 20$ €/h.

Failure rate and downtime of each turbine component are shown in Table 1, where: $\lambda_{min} = 0.02$; $\lambda_{max} = 0.625$; $r_{min} = 1\ h$; $r_{max} = 136.925\ h$.

The optimization results by the technique of Whale optimization algorithm are summarized in Table 13:

Table 13. results of problem optimization.

	A_i	β_i	n_i(H)	r_i(H)	λ_1(1/H)	λ_2(1/H)	λ_3(1/H)	C_T(€)	C_M (€)
WT 01	0.98	7	42	175.5	3.5025e-04	3.4993e-04	3.4958e-04	763031.56	8465.7
WT 02	0.98	7	42	175.5	3.4949e-04	3.4945e-04	3.4948e-04		8465.7
WT 03	0.98	7	42	175.5	3.4947e-04	3.4948e-04	3.4950e-04		8465.7

Table 13 shows that the minimum number of preventive maintenance tasks necessary to reduce failures is 7 tasks per turbine for a period of one year. The distribution of these tasks over equal 52-day intervals can help avoid unexpected failure of several wind turbine components with a failure rate greater than 0.00035, such as: Gearbox, Blades, Mechanical Brake, Electrical system, Control system and Others. The duration of unnecessary wind system shutdown can be reduced from 175.5 h to 66 h if the intervention of the maintenance team is immediate after each failure, hence a significant profitability of electricity production.

The simulation results by the whale algorithm also show an optimal availability of the wind farm of 98% and an optimal maintenance cost of 8465.70 € for each turbine without considering the production loss costs.

Figure 41, represents the evolution of the maintenance cost (Cmopt) and total cost (Ctopt) including the production losses costs according to the number of iterations which is limited by 1000 iterations in this simulation.

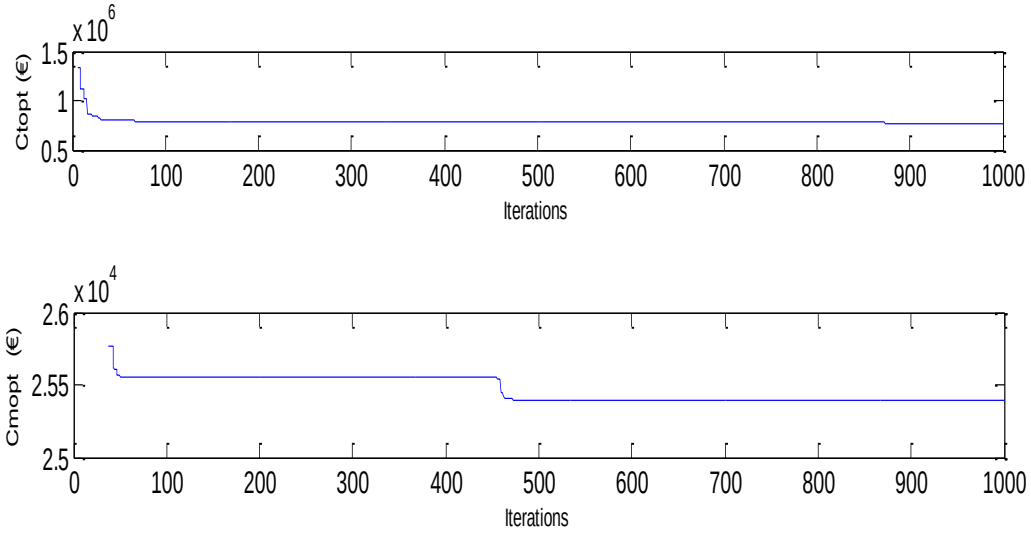

Figure 41: Wind farm total and maintenance costs optimized by Whale Optimisation Algorithm (WOA).

General Conclusion

This study addresses the dual challenge of optimizing the aero-structural performance of wind turbines and enhancing their operational availability. In The first part of the work, an analysis explores the intricate interplay between fluid dynamics and structural mechanics within Horizontal Axis Wind Turbines (HAWTs), providing insights into their behavior under a range of conditions, covering tip speeds ranging from 1 to 8.1 and examines blade structural responses at the maximum aerodynamic coefficient (tip speed ratio of 6.1) across a range of Young's modulus values from 5e8 to 1e10 Pa.

- The analysis of power coefficient (Cp) trends reveals distinct behaviors, with Cp initially increasing with tip-speed ratio (TSR), peaking at optimal TSR values, and subsequently declining.
- Visual representations of absolute pressure and velocity magnitude at several radial positions illustrate a high gradient in the case of the minimum tip speed ratio, contrasting with the maximum aerodynamic coefficient case.
- Moreover, examination of relative wind speed vectors unveils a significant finding of predicted flow separation near the blade's trailing edge at TSR = 2, with the flow separation region shortening towards the blade tip. However, for the highest tip-speed ratio, airflow remains attached to the blade across all radial positions.
- a radial deformation pattern emerges from the Blade Deformation Contours and the Blade Deformation curves, where blade deformation values appear to increase from the center of the blade (r=0) towards the blade's tip. Furthermore, the observed trend of decreasing blade deformation values with increasing YMs suggests an inverse relationship between this blade material parameter and aerodynamic forces. Additionally, von Mises stress serve as a material failure criterion, with maximum values detected at the blade-hub junction and midpoint of the blades. These stress values decrease with increasing Young's modulus values, with maximum values of 7.262e6, 6.909e6, and 6.570e6 Pa for YM values of 5e8, 9e8, and 1e10 Pa, respectively. The observed trend of blade tip deflection variation over time shows initial oscillations followed by stability at determined values. In the stability region, δ values decrease as Young's modulus (YM) values increase, with δ values of

0.1063, 0.0739, 0.0568, 0.0506, 0.0163, 0.0098, and 0.0049 meters for YM values of 5e8, 7e8, 9e8, 1e9, 3e9, 5e9, and 1e10 Pa, respectively.

- Furthermore, a comparison between One-way FSI and Two-way FSI simulation approaches reveals that the magnitude of the difference between the two approaches is dependent on the blade stiffness. At lower Young's modulus values, the discrepancy between the two methods is relatively significant, reaching a maximum of 8.21% for YM=5e8 Pa. This behavior can be attributed to the stronger fluid–structure coupling occurring in flexible blades, where aerodynamic loads continuously modify the blade geometry, which in turn alters the surrounding flow field. Consequently, the Two-way FSI approach captures these bidirectional interactions more accurately, resulting in larger predicted deflections. As the Young's modulus increases, the blade becomes progressively stiffer, reducing its sensitivity to aerodynamic loading. This leads to a gradual reduction in the difference between the two FSI approaches. For example, the discrepancy decreases from 5.67% at 7e8 Pa to 0.36% at 3e9 Pa, and eventually becomes nearly negligible for the highest stiffness cases. At YM=1e10 Pa, the difference slightly reverses (−0.176%), indicating that both approaches converge toward nearly identical predictions.

The second part delved into the aerodynamics of three airfoils—NACA-4412, NACA-23012, and NACA-63415—employing numerical simulations. The primary focus of the study was on evaluating performance and airflow patterns. Employing two-dimensional unsteady simulations, the computational approach thoroughly explored the effects of rotational speeds (ranging from 2 to 16 degrees per second) and a range of Reynolds numbers from 1.25e6 to 2e6. Key observations include:

- The analysis provides insights into the flow behavior around the airfoils by illustra ting the velocity magnitude and vectors and identifying flow separation regions, wi th a larger separation region observed in the case of NACA 63415.
- The analysis of lift coefficient values demonstrated a limited variance concerning changes in rotational speed, indicating that 8 degrees per second is an adequate rotational speed for the studied cases.
- An examination of airfoil aerodynamic coefficient trends revealed substantial

findings. Drag coefficient values increased over time, with greater values found for the NACA-63415 airfoil. Lift coefficient values, on the other hand, showed increasing variety, peaking at a value and then declining. Notably, the NACA 4412 airfoil has higher aerodynamic coefficients than the other airfoils tested.

The Third part presents a comprehensive numerical analysis of the aerodynamic performance of a Savonius wind turbine with three different diffuser configurations (SH1, SH2, and SH3), compared to a conventional Savonius design. The investigation focused on key performance metrics, such as power and torque coefficients, across a range of tip speed ratios (TSRs).

- The results showed that the addition of diffuser configurations significantly enhanced the turbine's aerodynamic efficiency, particularly in the SH1 and SH2 setups. The investigation found that the diffusers enhanced wind flow distribution by diverting the wind toward the blades' concave side, resulting in higher pressure in this region and less drag on the convex side. This enhanced airflow resulted in a significant improvement in power and torque coefficients, with the SH1 configuration having the highest power and torque coefficients of 0.433 and 1.08, respectively.

In the last part, the whale algorithm is proposed as a new approach for solving the wind farm maintenance optimization problem. The robustness, efficiency and rapid convergence of this approach compared to other methods reported in the literature has shown its superiority and ability to solve the problem in question.

- The results obtained from the simulation using the WOA algorithm showed that the appropriate number of preventive maintenance tasks corresponding to 3 failures in a reference period of one year is 7 tasks. Correct scheduling of these tasks versus corrective maintenance tasks can help prevent future unexpected shutdowns.
- The immediate intervention of the maintenance team after the occurrence of each failure can reduce the cost of lost production from 254,340 € to 90387 € for each wind turbine. The maintenance cost and the availability of each wind turbine are optimized at 8465.7 € and 98% respectively.

Together, the results of this research contribute new insights into how both design-level performance and maintenance scheduling can be optimized to improve wind turbine availability and efficiency. The dual perspective—technical (aerodynamic/structural performance) and operational (maintenance planning)— supports the development of more reliable, efficient, and cost-effective wind energy systems.

Bibliography

1. Beurskens, J., *The history of wind energy*. Understanding wind power technology: theory, deployment and optimisation, 2014: p. 1-44.
2. Hansen, M., *Aerodynamics of wind turbines*. 2015: Routledge.
3. Murty, P.S.R., *Chapter 24 - Renewable Energy Sources*, in *Electrical Power Systems*, P.S.R. Murty, Editor. 2017, Butterworth-Heinemann: Boston. p. 783-800.
4. Gasch, R. and J. Twele, *Wind power plants: fundamentals, design, construction and operation*. 2011: Springer Science & Business Media.
5. Whittlesey, R., *Chapter 10 - Vertical Axis Wind Turbines: Farm and Turbine Design*, in *Wind Energy Engineering*, T.M. Letcher, Editor. 2017, Academic Press. p. 185-202.
6. Breeze, P., *Chapter 3 - The Anatomy of a Wind Turbine*, in *Wind Power Generation*, P. Breeze, Editor. 2016, Academic Press. p. 19-27.
7. Zhao, D., et al., *Chapter 1 - General introduction to wind turbines*, in *Wind Turbines and Aerodynamics Energy Harvesters*, D. Zhao, et al., Editors. 2019, Academic Press. p. 1-20.
8. Bhattacharjee, S., *5 - Wind power technology*, in *Sustainable Fuel Technologies Handbook*, S. Dutta and C. Mustansar Hussain, Editors. 2021, Academic Press. p. 123-170.
9. Letcher, T.M., *Chapter 1 - Why Wind Energy?*, in *Wind Energy Engineering*, T.M. Letcher, Editor. 2017, Academic Press. p. 3-14.
10. Márquez, F.P.G., et al., *Condition monitoring of wind turbines: Techniques and methods.* Renewable energy, 2012. **46**: p. 169-178.
11. Naqash, T.M. and M.M. Alam, *A State-of-the-Art Review of Wind Turbine Blades: Principles, Flow-Induced Vibrations, Failure, Maintenance, and Vibration Suppression Techniques.* Energies, 2025. **18**(13): p. 3319.
12. Lydia, M. and G.E.P. Kumar, *Condition monitoring in wind turbines: a review.* Non-destructive testing and condition monitoring techniques in wind energy, 2023: p. 229-247.
13. Civera, M. and C. Surace, *Non-destructive techniques for the condition and structural health monitoring of wind turbines: A literature review of the last 20 years.* Sensors, 2022. **22**(4): p. 1627.
14. Peng, H., et al., *Analysis of wind turbine equipment failure and intelligent operation and maintenance research.* Sustainability, 2023. **15**(10): p. 8333.
15. Rajamohan, S., et al., *Approaches in performance and structural analysis of wind turbines–A review.* Sustainable energy technologies and assessments, 2022. **53**: p. 102570.
16. Molęda, M., et al., *From corrective to predictive maintenance—A review of maintenance approaches for the power industry.* Sensors, 2023. **23**(13): p. 5970.
17. Tchakoua, P., et al., *Wind turbine condition monitoring: State-of-the-art review, new trends, and future challenges.* Energies, 2014. **7**(4): p. 2595-2630.
18. Shafiee, M. and J.D. Sørensen, *Maintenance optimization and inspection planning of wind energy assets: Models, methods and strategies.* Reliability Engineering & System Safety, 2019. **192**: p. 105993.
19. Firoozi, A.A., A.A. Firoozi, and F. Hejazi, *Innovations in Wind Turbine Blade Engineering: Exploring Materials, Sustainability, and Market Dynamics.* Sustainability, 2024. **16**(19): p. 8564.
20. Li, W., et al., *Large-Scale Wind Turbine's Load Characteristics Excited by the Wind and Grid in Complex Terrain: A Review.* Sustainability, 2022. **14**(24): p. 17051.

21. Bai, C.-J. and W.-C. Wang, *Review of computational and experimental approaches to analysis of aerodynamic performance in horizontal-axis wind turbines (HAWTs).* Renewable and Sustainable Energy Reviews, 2016. **63**: p. 506-519.
22. Alrowwad, I., X. Wang, and N. Zhou, *Numerical modelling and simulation analysis of wind blades: a critical review.* Clean Energy, 2024. **8**(1): p. 261-279.
23. Cho, T. and C. Kim, *Wind tunnel test for the NREL phase VI rotor with 2 m diameter.* Renewable energy, 2014. **65**: p. 265-274.
24. Cho, T. and C. Kim, *Wind tunnel test results for a 2/4.5 scale MEXICO rotor.* Renewable energy, 2012. **42**: p. 152-156.
25. Ji, B., et al., *CFD simulations of aerodynamic characteristics for the three-blade NREL Phase VI wind turbine model.* Energy, 2022. **249**: p. 123670.
26. Muiruri, P.I., O.S. Motsamai, and R. Ndeda, *A comparative study of RANS-based turbulence models for an upscale wind turbine blade.* SN Applied Sciences, 2019. **1**(3): p. 237.
27. Moshfeghi, M., Y.J. Song, and Y.H. Xie, *Effects of near-wall grid spacing on SST-K-ω model using NREL Phase VI horizontal axis wind turbine.* Journal of Wind Engineering and Industrial Aerodynamics, 2012. **107**: p. 94-105.
28. Mo, J.-O. and Y.-H. Lee, *CFD Investigation on the aerodynamic characteristics of a small-sized wind turbine of NREL PHASE VI operating with a stall-regulated method.* Journal of mechanical science and technology, 2012. **26**: p. 81-92.
29. Tachos, N., A. Filios, and D. Margaris, *A comparative numerical study of four turbulence models for the prediction of horizontal axis wind turbine flow.* Proceedings of the Institution of Mechanical Engineers, Part C: Journal of Mechanical Engineering Science, 2010. **224**(9): p. 1973-1979.
30. Tachos, N., et al., *A computational aerodynamics simulation of the NREL phase II rotor.* Open Mechanical Engineering Journal, 2009. **3**: p. 9-16.
31. AbdelSalam, A.M. and V. Ramalingam, *Wake prediction of horizontal-axis wind turbine using full-rotor modeling.* Journal of Wind Engineering and Industrial Aerodynamics, 2014. **124**: p. 7-19.
32. Abdelsalam, A.M., et al., *Experimental and numerical studies on the wake behavior of a horizontal axis wind turbine.* Journal of Wind Engineering and Industrial Aerodynamics, 2014. **128**: p. 54-65.
33. Sudhamshu, A., et al., *Numerical study of effect of pitch angle on performance characteristics of a HAWT.* Engineering Science and Technology, an International Journal, 2016. **19**(1): p. 632-641.
34. Thumthae, C. and T. Chitsomboon, *Optimal angle of attack for untwisted blade wind turbine.* Renewable energy, 2009. **34**(5): p. 1279-1284.
35. Yossri, W., S.B. Ayed, and A. Abdelkefi, *Airfoil type and blade size effects on the aerodynamic performance of small-scale wind turbines: Computational fluid dynamics investigation.* Energy, 2021. **229**: p. 120739.
36. Khalafallah, M.G., A.M. Ahmed, and M.K. Emam, *The effect of using winglets to enhance the performance of swept blades of a horizontal axis wind turbine.* Advances in Mechanical Engineering, 2019. **11**(9): p. 1687814019878312.
37. Lipian, M., P. Czapski, and D. Obidowski, *Fluid–structure interaction numerical analysis of a small, urban wind turbine blade.* Energies, 2020. **13**(7): p. 1832.
38. Roul, R. and A. Kumar, *Fluid-structure interaction of wind turbine blade using four different materials: numerical investigation.* Symmetry, 2020. **12**(9): p. 1467.
39. Wang, L., R. Quant, and A. Kolios, *Fluid structure interaction modelling of horizontal-axis wind turbine blades based on CFD and FEA.* Journal of Wind Engineering and Industrial Aerodynamics, 2016. **158**: p. 11-25.

40. Huque, Z., et al., *Fluid–Structure Interaction Simulations of Wind Turbine Blades with Pointed Tips.* Energies, 2024. **17**(5): p. 1090.
41. Li, W., et al., *The aerodynamic performance of horizontal axis wind turbines under rotation condition.* Sustainability, 2023. **15**(16): p. 12553.
42. Shi, F., et al., *Influences of wind and rotating speed on the fluid-structure interaction vibration for the offshore wind turbine blade.* Journal of Vibroengineering, 2019. **21**(2): p. 483-497.
43. Thangavelu, S.K., et al., *Aeroelastic performance analysis of horizontal axis wind turbine (HAWT) swept blades.* Materials Today: Proceedings, 2021. **47**: p. 4965-4972.
44. Krogstad, P.Å. and J. Lund, *An experimental and numerical study of the performance of a model turbine.* Wind Energy, 2012. **15**(3): p. 443-457.
45. ANSYS, I., *Ansys fluent user's guide, 2022R1*. Ansys Fluent User's Guide. 2022.
46. Manwell, J.F., J.G. McGowan, and A.L. Rogers, *Wind energy explained: theory, design and application*. 2010: John Wiley & Sons.
47. Alfonsi, G., *Reynolds-averaged Navier–Stokes equations for turbulence modeling.* 2009.
48. Nichols, R., *Turbulence Models and Their Application to Complex Flows*. 2010.
49. Ferziger, J.H., M. Perić, and R.L. Street, *Computational Methods for Fluid Dynamics*. 2019: Springer.
50. Versteeg, H.K., *An introduction to computational fluid dynamics the finite volume method, 2/E*. 2007: Pearson Education India.
51. ANSYS, I., *Ansys fluent Theory Guide, 2022R1*. Ansys fluent Theory Guide. 2022.
52. Schaffarczyk, A.P., *Introduction to wind turbine aerodynamics*. 2020: Springer Nature.
53. Jones, D.R.H. and M.F. Ashby, *Chapter 3 - Elastic Moduli*, in *Engineering Materials 1 (Fifth Edition)*, D.R.H. Jones and M.F. Ashby, Editors. 2019, Butterworth-Heinemann. p. 31-47.
54. Leifsson, L. and S. Koziel, *Aerodynamic shape optimization by variable-fidelity computational fluid dynamics models: a review of recent progress.* Journal of Computational Science, 2015. **10**: p. 45-54.
55. Sharma, P., et al., *Recent advancements in optimization methods for wind turbine airfoil design: A review.* Materials Today: Proceedings, 2021. **47**: p. 6556-6563.
56. Tefera, G., G. Bright, and S. Adali, *Theoretical and computational studies on the optimal positions of NACA airfoils used in horizontal axis wind turbine blades.* Journal of Energy Systems, 2022. **6**(3): p. 369-386.
57. Bayram, H., *Numerical investigation of airfoils aerodynamic performances.* International Journal of Energy Applications and Technologies, 2022. **9**(1): p. 1-5.
58. Almohammadi, K., *Assessment of several modeling strategies on the prediction of lift-drag coefficients of a NACA0012 airfoil at a moderate Reynold number.* Alexandria Engineering Journal, 2022. **61**(3): p. 2242-2249.
59. Görgülü, Y.F., M.A. Özgür, and R. Köse, *CFD analysis of a NACA 0009 aerofoil at a low reynolds number.* Politeknik Dergisi, 2021. **24**(3): p. 1237-1242.
60. Göv, İ. and M.H. Doğru, *Aerodynamic optimization of NACA 0012 airfoil.* The International Journal of Energy and Engineering Sciences, 2020. **5**(2): p. 146-155.
61. Erkan, O., et al., *Investigation of aerodynamic performance characteristics of a wind-turbine-blade profile using the finite-volume method.* Renewable energy, 2020. **161**: p. 1359-1367.
62. Oukassou, K., et al., *Comparison of the power, lift and drag coefficients of wind turbine blade from aerodynamics characteristics of Naca0012 and Naca2412.* Procedia Manufacturing, 2019. **32**: p. 983-990.

63. Yılmaz, M., et al., *A comparative CFD analysis of NACA0012 and NACA4412 airfoils.* Journal of Energy Systems, 2018. **2**(4): p. 145-159.
64. Koca, K., et al., *Identification of flow phenomena over NACA 4412 wind turbine airfoil at low Reynolds numbers and role of laminar separation bubble on flow evolution.* Energy, 2018. **144**: p. 750-764.
65. Sutardi, S. and M.N. Fuad. *Flow characteristics around a NACA 4412 airfoil in the ground proximity*. in *AIP Conference Proceedings*. 2023. AIP Publishing.
66. Nirooei, M., *Aerodynamic and static stability characteristics of airfoils in extreme ground effect.* Proceedings of the Institution of Mechanical Engineers, Part G: Journal of Aerospace Engineering, 2018. **232**(6): p. 1134-1148.
67. Qu, Q., et al., *Airfoil aerodynamics in ground effect for wide range of angles of attack.* AIAA Journal, 2015. **53**(4): p. 1048-1061.
68. Qu, Q., et al., *Numerical study of the aerodynamics of a NACA 4412 airfoil in dynamic ground effect.* Aerospace Science and Technology, 2014. **38**: p. 56-63.
69. Qu, Q., et al. *Aerodynamics and Flow Physics of a NACA 4412 Airfoil in Dynamic Ground Effect*. in *52nd Aerospace Sciences Meeting*. 2014.
70. Ockfen, A.E. and K.I. Matveev, *Aerodynamic characteristics of NACA 4412 airfoil section with flap in extreme ground effect.* International Journal of Naval Architecture and Ocean Engineering, 2009. **1**(1): p. 1-12.
71. Qu, Q., et al. *Aerodynamics of an airfoil in dynamic ground effect during take-off*. in *55th AIAA aerospace sciences meeting*. 2017.
72. Liu, X.a., et al., *Numerical Study on Airfoil Aerodynamics in Proximity to Wavy Water Surface for Various Amplitudes.* Applied Sciences, 2021. **11**(9): p. 4215.
73. Hu, H. and D. Ma, *Airfoil aerodynamics in proximity to wavy ground for a wide range of angles of attack.* Applied Sciences, 2020. **10**(19): p. 6773.
74. Zhi, H., et al. *Numerical analysis of aerodynamics of a NACA4412 airfoil above wavy water surface*. in *AIAA aviation 2019 forum*. 2019.
75. Lee, T. and V. Tremblay-Dionne, *Experimental investigation of the aerodynamics and flowfield of a NACA 0015 airfoil over a wavy ground.* Journal of Fluids Engineering, 2018. **140**(7): p. 071202.
76. Coles, D. and A.J. Wadcock, *Flying-hot-wire study of flow past an NACA 4412 airfoil at maximum lift.* AIAA Journal, 1979. **17**(4): p. 321-329.
77. Tagawa, G.d., F. Morency, and H. Beaugendre. *CFD study of airfoil lift reduction caused by ice roughness*. in *2018 Applied Aerodynamics Conference*. 2018.
78. Cuevas-Carvajal, N., et al., *Effect of geometrical parameters on the performance of conventional Savonius VAWT: A review.* Renewable and Sustainable Energy Reviews, 2022. **161**: p. 112314.
79. Shende, V., et al., *A review on comparative study of Savonius wind turbine rotor performance parameters.* Environmental Science and Pollution Research, 2022. **29**(46): p. 69176-69196.
80. Patel, H. and A.S. Mohite, *CFD Analysis of Savonius Wind Turbine with Guide Vanes.*
81. Shahriare, S., M.R. Rony, and P. Das, *Enhanced Aerodynamic Performance of Savonius Wind Turbines Through Blade Design Modifications: A CFD Study.* Wind Energy, 2025. **28**(8): p. e70042.
82. Tanino, T., R. Yoshihara, and T. Miyaguni, *A Study on a Casing Consisting of Three Flow Deflectors for Performance Improvement of Cross-Flow Wind Turbine.* Energies, 2022. **15**(16): p. 6093.
83. Aboujaoude, H., et al., *Aerodynamic performance enhancement of an axisymmetric deflector applied to savonius wind turbine using novel transient 3D CFD simulation techniques.* Energies, 2023. **16**(2): p. 909.

84. Tata, M., et al., *Aerodynamic performance investigations of savonius twin-rotor wind turbines.* Journal of Applied Fluid Mechanics, 2023. **17**(2): p. 442-460.
85. Kariuki, S., et al., *CFD Investigation of the Effect of Multiple Phase Shift Angles on the Performance of a Two-Stage Savonius Wind Turbine.* AMERICAN JOURNAL OF ENERGY RESEARCH Учредители: Science and Education Publishing Co., Ltd., 2024. **12**(3): p. 63-69.
86. Ferrari, G., et al., *CFD study of Savonius wind turbine: 3D model validation and parametric analysis.* Renewable energy, 2017. **105**: p. 722-734.
87. Sumiati, R., U.G.S. Dinata, and D.A. Saputra, *Enhancing the performance of Savonius rotor using tiered-height zigzag patterns in concave surface.* Journal of Applied Engineering Science, 2024. **22**(1): p. 113-122.
88. Mohamed, M.H., et al., *Enhancement attempts for a three-bladed Savonius turbine performance.* Frontiers in Energy Research, 2022. **10**: p. 797868.
89. Mahizam, M.H.F., et al., *Improving Savonius turbine efficiency with splitter and barrier cylinder deflector design: A Taguchi method study.* Physics of Fluids, 2023. **35**(11).
90. Layeghmand, K., N. Ghiasi Tabari, and M. Zarkesh, *Improving efficiency of Savonius wind turbine by means of an airfoil-shaped deflector.* Journal of the Brazilian Society of Mechanical Sciences and Engineering, 2020. **42**(10): p. 528.
91. Afify, R., E. Saber, and H. Awad, *Investigation of an innovative Savonius turbine in practice.* Scientific Reports, 2025. **15**(1): p. 6937.
92. Ramarajan, J. and S. Jayavel, *Performance improvement in Savonius wind turbine by modification of blade shape.* Journal of Applied Fluid Mechanics, 2021. **15**(1): p. 99-107.
93. Ghafoorian, F., et al., *Performance Optimization of Savonius VAWTs Using Wind Accelerator and Guiding Rotor House for Enhanced Rooftop Urban Energy Harvesting.* Machines, 2025. **13**(9): p. 838.
94. Zereg, A., et al., *Performance enhancement of Savonius wind turbine through partially deformable blades.* International Journal for Simulation and Multidisciplinary Design Optimization, 2024. **15**: p. 8.
95. Sugiharto, B., et al., *Performances of Savonius rotor with addition guide vanes.* International Journal of Renewable Energy Research (IJRER), 2016. **6**(4): p. 1336-1341.
96. Singh, S.V. and P. Kumar, *Study of flow characteristics of a savonius turbine inside nozzle diffuser duct.* Journal of Engineering Research, 2022.
97. Ang, E.B. and J.P. Honra, *Theoretical aerodynamic performance and FEA analysis of a novel three-blade Savonius wind turbine blade with pointed deflectors.* Dynamics, 2025. **5**(1): p. 8.
98. Mirashi, D.N. and S. Kumarappa, *CFD Analysis on Two Bladed Savonius Wind Turbine With and Without Splitter.* International Research Journal of Engineering and Technology (IRJET) e-ISSN, 2016: p. 2395-0056.
99. Debnath, P. and R. Debbarma. *Numerical study for the improvement of performance of Savonius wind turbine having elliptical blades*. in *E3S Web of Conferences*. 2024. EDP Sciences.
100. Mohammadi, M., et al., *Numerical investigation of performance refinement of a drag wind rotor using flow augmentation and momentum exchange optimization.* Energy, 2018. **158**: p. 592-606.
101. Khalil, A., et al., *Numerical Study of the Effect of Long Shroud Diffuser with and without Plate Obstacle on the Performance of Savonius Wind Turbine.*

102. Antar, E. and M. Elkhoury, *Parametric sizing optimization process of a casing for a Savonius Vertical Axis Wind Turbine.* Renewable Energy, 2019. **136**: p. 127-138.
103. Hesami, A., A.H. Nikseresht, and M.H. Mohamed, *Feasibility study of twin-rotor Savonius wind turbine incorporated with a wind-lens.* Ocean Engineering, 2022. **247**: p. 110654.
104. Guo, F., et al., *Experimental and numerical validation of the influence on Savonius turbine caused by rear deflector.* Energy, 2020. **196**: p. 117132.
105. Hayashi, T., Y. Li, and Y. Hara, *Wind tunnel tests on a different phase three-stage Savonius rotor.* JSME International Journal Series B Fluids and Thermal Engineering, 2005. **48**(1): p. 9-16.
106. Benmessaoud, T., K. Mohammedi, and Y. Smaili, *Influence of maintenance on the performance of a wind farm.* Przegląd Elektrotechniczny, 2013. **89**(03a): p. 174-178.
107. Benmessaoud, T., et al., *Wind Farms Predictive Maintenance Based on Condition Monitoring System.* International Journal of Advanced Studies in Computers, Science and Engineering, 2021. **10**(5): p. 1-6.
108. Mirjalili, S. and A. Lewis, *The whale optimization algorithm.* Advances in engineering software, 2016. **95**: p. 51-67.
109. Gonzalo, A.P., et al., *Optimal maintenance management of offshore wind turbines by minimizing the costs.* Sustainable Energy Technologies and Assessments, 2022. **52**: p. 102230.